HIGH-PERFORMANCE MICROMACHINED VIBRATORY RATE- AND RATE- INTEGRATING GYROSCOPES

by

Jae Yoong Cho

A dissertation submitted in partial fulfillment
of the requirements for the degree of
Doctor of Philosophy
(Electrical Engineering)
in The University of Michigan
2012

Doctoral Committee:

Professor Khalil Najafi, Chair
Professor Yogesh Gianchandani
Professor Noel C. Perkins
Sang Woo Lee, Epack Inc.

This thesis is dedicated to my wife Fusaka, my parents Hyunkyu and Kwisook, my brother Jae Hong, my parents-in-law Toshio and Shigeko, and my sister-in-law Miho for their love and support. I also thank my dog Jane for staying healthy during my PhD years.

ACKNOWLEGEMENTS

I would like to thank everyone who helped me throughout my PhD years. First, I thank my advisor, Professor Najafi, for giving me the opportunity to pursue my PhD degree and supporting me throughout the years. Although I have been struggling with my research for the first few years, he was very patient and generously allowed me to try all the experiments that I wanted to try. Many of these experiments failed, but I learned a lot from these failures. He also outworked all of us and encouraged us to do our best. At the same time, he also cared a lot about our feelings and our families.

I also thank my thesis committee members, Professor Yogesh Gianchandani, Professor Noel Perkins, and Dr. Sangwoo Lee. I also thank Professor Ken Wise for being in my prelim committee and continuously encouraging my research.

I thank Professor Osamu Tabata at Kyoto University, Japan, for his great kindness. He allowed me to work in his research group in the summer of 2004, right after I received my undergraduate degree. Since then, he treated me as his own student, and whenever I visit Osaka, he invited me to his group's research seminars and parties. He also came to our wedding in 2009 and gave a speech for us in three different languages. Because of Professor Tabata, I became interested in the MEMS area and pursued my Ph.D. in this area.

I thank my mentors in the Najafi research group, Drs. Junseok Chae, Sangwoo Lee, Sanghyun Lee, and Sangwon Yoon, for their kindness. I especially thank my research

project mate Jeffrey Gregory for the friendship and scientific discussions. Without his knowledge and insights, our research would have never been to the current level. Besides being a good researcher, he is a good cook, and he kindly invited our family to his house for several occasions. I also specially thank my group mate Dr. Tzeno Galchev for the friendship, joyfulness, and smartness. We started in the same year and spent many years together.

I also thank my current and previous group mates Zongliang, Guohong, Jialiang, Ali, Amir, Daniel, Erkan, Niloufar, James, Kevin, Mahdi, Seowyuen, Andy Gross, Andy Kuo, Jay, Neil, Hanseup, Burcu, TJ, Stefan, Pedram. I thank Seowyuen for helping me during the preparation of my thesis. I thank Dr. Becky Peterson and Mr. Robert Gordenker for their support.

Lastly, I thank all my friends for the their friendship and support.

TABLE OF CONTENTS

LIST OF FIGURES

LIST OF TABLES

LIST OF APPENDICES

ABSTRACT

HIGH-PERFORMANCE MICROMACHINED VIBRATORY RATE- AND RATE-INTEGRATING GYROSCOPES

by

Jae Yoong Cho

Chair: Khalil Najafi

The performance of vibratory micromachined gyroscopes has been continuously improving for the past two decades. However, to further improve performance of the MEMS gyroscope in harsh environment, it is necessary for gyros to reduce the sensitivity to environmental parameters, including vibration and temperature change. In addition, conventional rate-mode MEMS gyroscopes have limitation in performance due to tradeoff between resolution, bandwidth, and full-scale range.

In this research, we aim to reduce vibration sensitivity by developing gyros that operate in the balanced mode. The balanced mode creates zero net momentum and reduces energy loss through an anchor. The gyro can differentially cancel measurement errors from external vibration along both sensor axes. The vibration sensitivity of the balanced-mode gyroscope including structural imbalance from microfabrication reduces as the absolute difference between in-phase parasitic mode and operating mode frequencies increases. The parasitic sensing mode frequency is designed larger than the

operating mode frequency to achieve both improved vibration insensitivity and shock resistivity. A single anchor is used in order to minimize thermoresidual stress change.

We developed two gyroscope based on these design principles. The Balanced Oscillating Gyro (BOG) is a quad-mass tuning-fork rate gyroscope. The relationship between gyro design and modal characteristics is studied extensively using finite element method (FEM). The gyro is fabricated using the planar Si-on-glass (SOG) process with a device thickness of 100μm. The BOG is evaluated using the first-generation analog interface circuitry. Under a frequency mismatch of 5Hz between driving and sense modes, the angle random walk (ARW) is measured to be 0.44°/sec/√Hz. The performance is limited by quadrature error and low-frequency noise in the circuit.

The Cylindrical Rate-Integrating Gyroscope (CING) operates in whole-angle mode. The gyro is completely axisymmetric and self-aligned to maximize mechanical isotropy. The gyro offers a large frequency ratio of ~1.7 between parasitic and the wineglass modes. The CING is fabricated using the 3D Si-on-glass (SOG) process with a device thickness of 300μm. The 1st and 2nd generation CINGs operate at 18kHz and 3kHz, respectively and demonstrate a frequency mismatch of <1% and a large Q (~20,000 at 18kHz and ~100,000 at 3kHz under exact mode matching). In the rate-sensing mode, the first-generation CING (18kHz) demonstrates an A_g of 0.05, an angle random walk (ARW) of 7°/√hr, and a bias stability of 72°/hr without temperature compensation. The performance is limited by the A_g, white noise in the phase-lock loop (PLL) in the interface circuitry, and temperature control. In the rate-sensing mode, the second-generation CING measures an A_g of 0.0065, an ARW of 0.09°/√hr, and a bias stability of 129°/hr without temperature compensation. The performance is limited by A_g and temperature compensation. In the rate-integration mode, the gyro demonstrates precession with an A_g of 0.011±0.001 under a frequency mismatch of 20~80mHz during several hours of operation.

CHAPTER 1.

INTRODUCTION TO MEMS GYROSCOPES

Gyroscopes are sensors for measuring rotation [1]. There exist several types of gyroscopes based on various physical principles. Typical applications include military, automotive, guidance, and consumer electronics. Based on physical principles, gyroscopes can be categorized as: 1) mechanical gyroscopes [2-31], 2) optical gyroscopes [32, 33], 3) nuclear magnetic resonance (NMR) gyroscopes [34, 35], and 4) cold atom gyroscopes [36, 37], as summarized in Figure 1.1.

Mechanical gyroscopes measure the Coriolis force. This force is named after the French scientist Gaspard-Gustave Coriolis who discovered it in 1835. The Coriolis force acts on a moving body under rotation and is perpendicular to both the velocity and the rotation directions. Depending on designs, mechanical gyroscopes can detect either precession angles [29] or rotation rates [2-27]. They have a wide range of performance in terms of angle random walk (ARW, short-term rate noise density) and bias stability (long-term rate noise). Among these, the Hemispherical Resonator Gyroscope (HRG) provides one of the best ARW and bias stability [29, 40]. The operation of optical gyroscopes is based on the Sagnac effect [32]. This effect refers to rotation-induced path-length differences for oppositely-traveling lights through an optical loop. Ring laser gyroscopes (RLG) and fiber optic gyroscopes (FOG) belong to this category, and are widely used in high-performance applications [33, 41]. Other gyroscopes are still under development, including nuclear magnetic resonance (NMR) gyroscopes and cold atom gyroscopes. The former is based on the change in the precession frequency of noble-gas molecules' magnetic moment (the Larmor frequency) due to rotation [34, 35], and the latter is based on rotation-induced path-length change for two oppositely-traveling atomic waves (the Broglie wave) at extremely low temperature [36, 37].

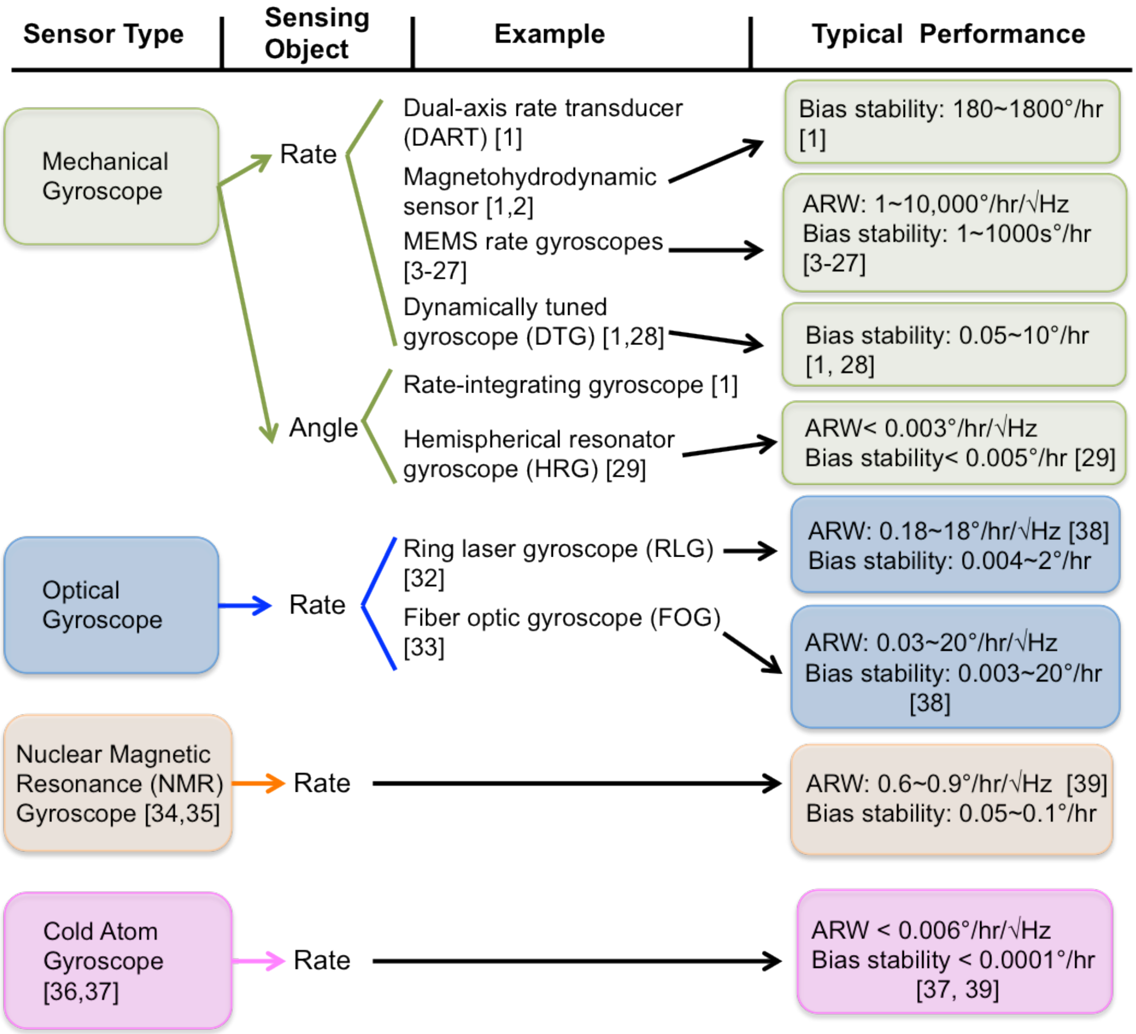

Figure 1.1. Classification of gyroscopes.

Gyroscopes have to satisfy certain requirements dictated by the particular application. These specifications include ARW, bias stability, scale factor accuracy, full-scale range, maximum endurable shock, and detection bandwidth. The typical requirements for rate-grade, tactical-grade, and inertial-grade gyroscopes are summarized in Table 1.1 [3]. Rate-grade applications include automotive rollover protection and image stabilization for camcorders. Tactical-grade applications include missile guidance, radar stabilization, and autonomous vehicle guidance. Inertial-grade applications include inertial references for aircrafts or spacecrafts. ARW and bias stability are often considered as the two most important performance indicators because they directly represent the minimum detectable rotation rate of a given gyroscope. The HRG, RLG, and FOG satisfy tactical and inertial requirements, but they are too large and expensive for portable applications [40]. Micromachined gyroscopes, on the other hand, were originally developed and used for rate-grade applications such as automotive stabilization or jitter compensation because of their compactness, affordability, and acceptable performance [30, 31, 42-44]. Their performance has continuously improved during the past two decades and has reached near-inertial grade, as shown in Figures 1.2 and 1.3, due to advances in design, electronics, fabrication technology, and packaging. Figure 1.4 shows the comparison of the size and the bias stability for different types of gyroscopes [1, 3-29, 37-39]. As this figure indicates, micro-gyroscopes have considerably smaller size compared to the others, and their performance is still being improved.

Table 1.1. Performance requirements for different classes of gyroscopes [3]

Parameter	Rate Grade	Tactical Grade	Inertial Grade
Angle Random Walk* (°/√hr)	>0.5	0.05-0.5	<0.001
Bias Drift (°/hr)	10-1000	0.1-10	<0.01
Scale Factor Accuracy (%)	0.1-1	0.01-0.1	<0.001
Full Scale Range (°/sec)	50-1000	>500	>400
Max. Shock in 1msec, g’s	10^3	10^3-10^4	10^3
Bandwidth (Hz)	>70	~100	~100

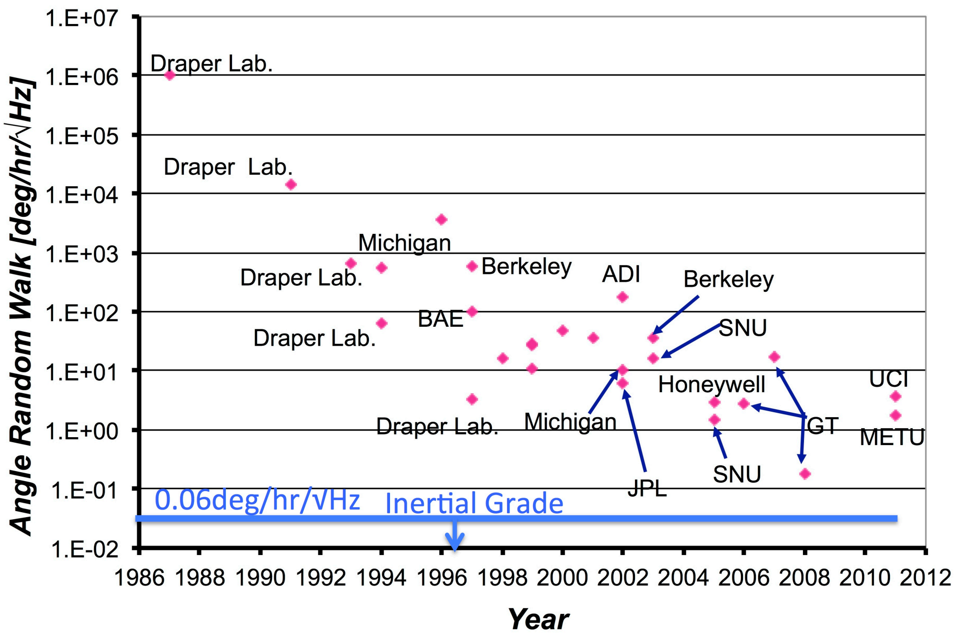

Figure 1.2. Trend of angle random walk (ARW) improvement [4-27, 45, 46].

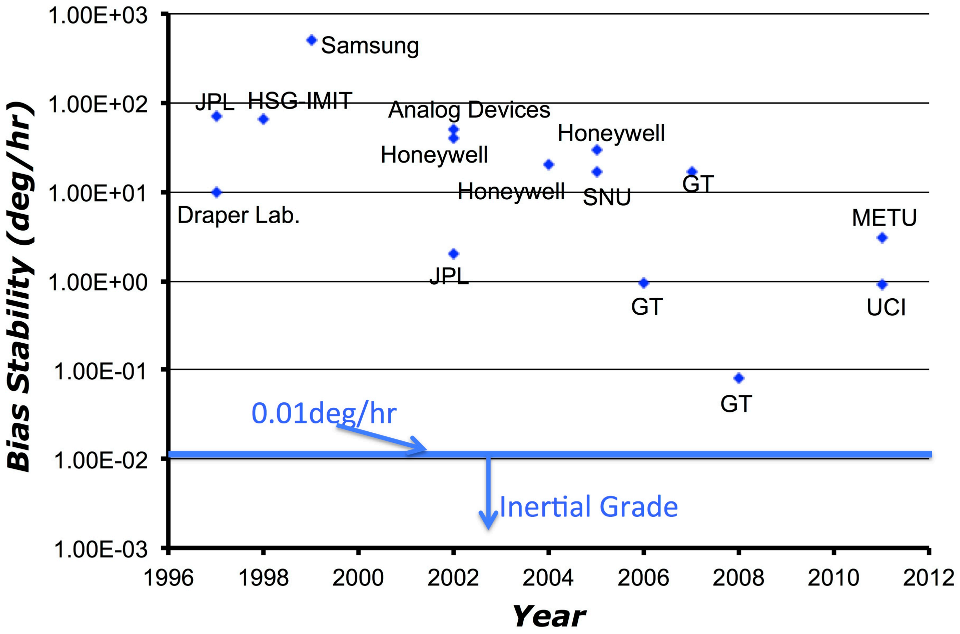

Figure 1.3. Trend of bias stability improvement [11, 12, 15, 18, 20, 23-27, 45-49].

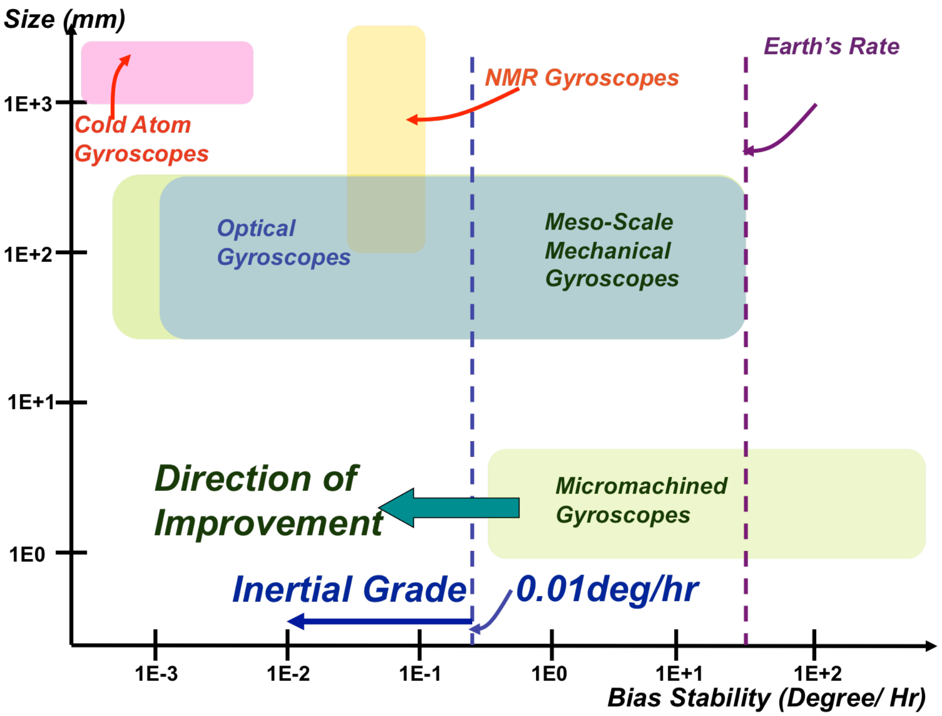

Figure 1.4 Comparison of the dimensions and the bias stability of different types of gyroscopes (optical gyroscopes: after [41]; meso-scale mechanical gyroscopes: after [1], [28, 29]; NMR gyroscopes: after [39]; cold atom gyroscopes: after [37], MEMS gyroscopes: after [3-27].

1.1. Mechanical Gyroscopes

Vibratory micro-gyroscopes utilize the Coriolis force to sense the rate of rotation [7]. The relationship between the Coriolis force ($\overrightarrow{F_{Coriolis}}$), effective mass ($M$), velocity ($\vec{v}$), rotation rate ($\vec{\Omega}$), and angular gain factor (k) is given by:

$$\overrightarrow{F_{Coriolis}} = 2kM\vec{v}\times\vec{\Omega} \qquad \text{(Equation 1.1)}$$

The angular gain factor k depends on whether the gyro is a lumped mass gyro or a solid wave gyro. The k of a lumped mass gyro, like the tuning fork gyro, is 1. For a continuous mass gyro, like ring gyro or the cylindrical gyro operating in the nth flexural mode (wineglass mode), k is equal to nA_g, where A_g is named the angular gain. They will be explained in Chapter 2.

The Coriolis force is utilized by micro-gyroscopes, because it can be easily detected using masses of several micro-grams and the displacements induced by the Coriolis force can be easily detected using standard electronics. Optical gyroscopes are more difficult to be scaled down, because they typically require long optical paths and lasers [32], NMR gyroscopes use special gas molecules and strong magnetic shields [34, 35], and cold atom gyroscopes need cryogenic coolers [36], making them large and difficult to minimize.

Mechanical micro-gyroscopes are generally divided in two different types. The first type is vibratory micro-gyroscopes, such as a tuning-fork micro-gyroscope shown in Figure 1.5 [4]. This type of device consists of masses, flexures, and supporting anchors. The operation of the device relies on oscillating the masses along their drive axes to generate momentum, and measuring the Coriolis-induced oscillations along their sense axes to measure rotation. Detection schemes include capacitive [4-9], electromagnetic [10], piezoelectric [42, 43], piezoresistive [50], and tunneling [14]. The second type is electrically-suspended spinning-mass micro-gyroscopes. This type of device consists of rotors, frames, and stators [51, 52] (Figure 1.6). The device generates momentum by spinning the rotor that is placed inside the cavity created between the top stator, the frame, and the bottom stator. Under rotation, the Coriolis force tilts the rotor along the direction normal to the spin and the rotation axes, and the angle is electronically detected. When the two types are compared, the former is advantageous by being mechanical stability, better vibration and shock resistivity, batch producibility, and simpler control. The proposed research focuses on vibratory micro-gyroscopes with electrostatic actuation and capacitive detection. Capacitive gyroscopes are easy to fabricate using conventional micro-fabrication technologies, easy to scale down, provide good sensitivity, and require low power.

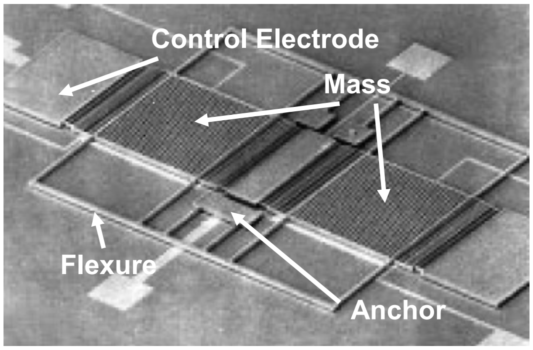

Figure 1.5. SEM picture of the vibratory tuning fork micro-gyroscope (TFG) [4].

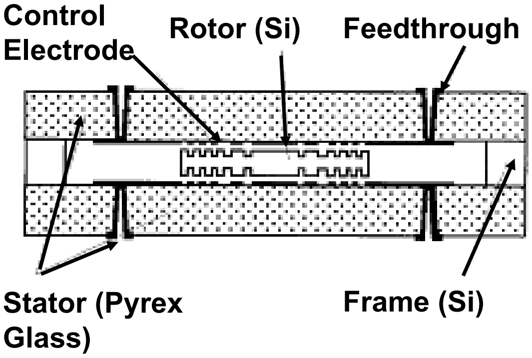

Figure 1.6. Schematic of electrically-suspended micro-gyroscope [51].

Figure 1.7 shows a simplified diagram of a single-mass vibratory rate-sensing gyroscope, interface circuit, and the Fourier representations of the processed signals. The gyroscope's mass is driven along its drive axis, and the amplitude of the drive oscillation is sustained using a positive feedback loop. Under rotation, the mass will also oscillate along its sense axis, and the amplitude of the sense oscillation is detected. The output signal contains the rotation rate which modulate the mass along its sense axis. The rotation rate is extracted by demodulating this signal using a reference signal derived from the driving motion of the gyro.

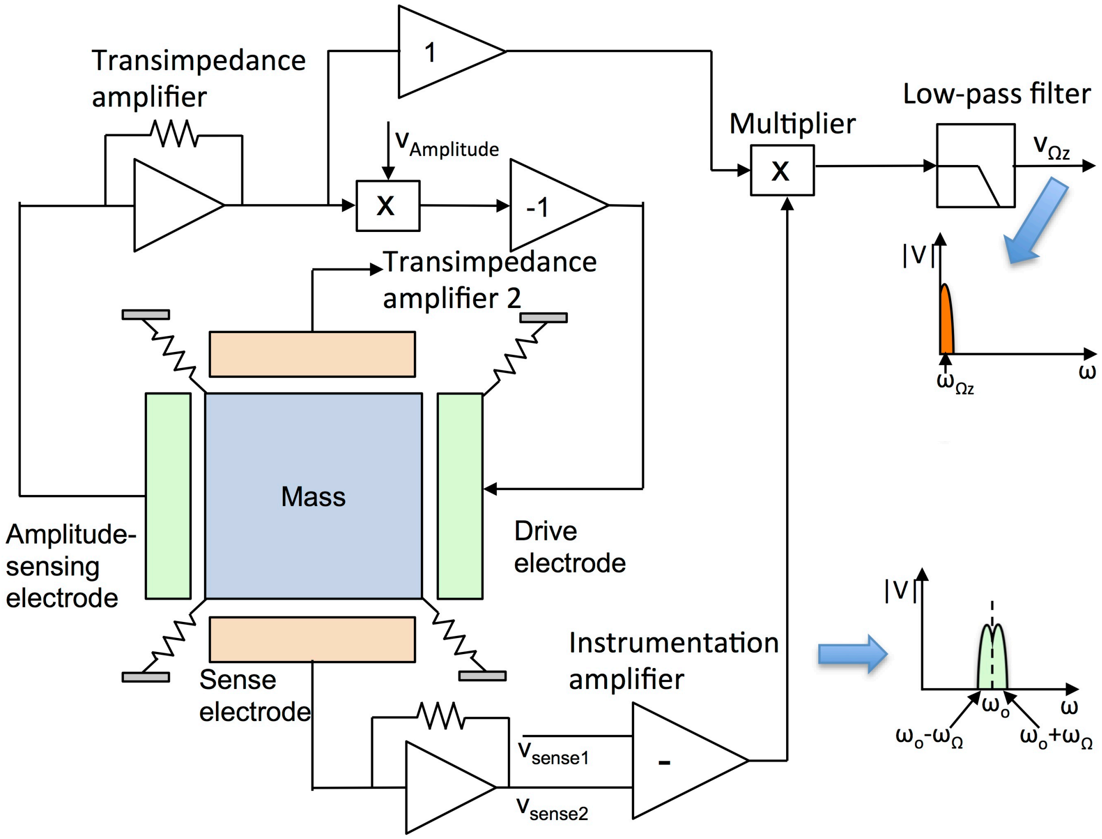

Figure 1.7. Simplified diagram of a vibratory capacitive gyroscope, showing device, interface circuitry, and Fourier representation of the processed signals.

1.2. Sensitivity of Micromachined Gyroscopes to Vibration and Temperature

When a vibratory gyroscope is subjected to forces due to shock or vibration, the deflection creates drift. This creates an error signal indistinguishable from the deflection due to the Coriolis force. The frequency of the shock and vibration that affect the gyroscope's operation need to be close to the resonance frequency of the gyroscope, otherwise the signal is filtered out at the sensor's demodulation unit. Since most of the vibration from environment exists up to a few hundred Hertz, a MEMS gyroscope is designed to have an operating frequency of at least a few thousand Hertz.

Another source of error due to the environment is frequency shift and the resultant scale factor change due to temperature change. The resonance frequency of a mechanical resonator changes with change in thermoresidual stress. For example, the thermal coefficient of frequency (TC_F) of a clamped-clamped beam undergoing the fundamental bending motion is expressed as [53]:

$$TC_F(C-C\ \ Beam) \approx 0.151\left(\frac{L}{w}\right)^2(\alpha_{sensor}-\alpha_{substrate})+\frac{TC_E}{2}+\frac{\alpha}{2} \qquad \text{(Equation 1.2)}$$

[TC_E (Si): -37.48 ppm/K (thermal coefficient of elasticity),
α (Si): 2.6 ppm/K (thermal coefficient of expansion)]

In this equation, the first term accounts for thermoresidual stress change, which is strongly related to the geometry of the resonator. The second and third terms account for material properties. In a mechanical gyro, the difference between drive and sense mode frequencies needs to be kept constant to achieve a constant scale factor. In order to keep the frequency difference constant, it is necessary to minimize thermoresidual stress change. The amount of thermoresidal stress can be minimized if a gyro has a single anchor at the center of the device and the size of the anchor is minimized to the level allowed by microfabrication process.

A gyro's vibration sensitivity can be reduced with a mechanical isolation stage. The isolation stage is basically a flexible spring-mass system with its resonance frequency located at a fraction of the resonance frequency of the gyroscope mounted on it. The stage transmits low-frequency vibration, containing rotational data, and filters high-frequency vibration (above its resonance frequency). The isolation platform also plays a role in reducing temperature sensitivity. A gyro's temperature sensitivity can be reduced by oven-controlling the temperature of the sensor, similar to an Oven-Controlled Crystal Oscillator (OCXO). In order to reduce the input power to sustain with tens of milliwatts for industrial temperature range (-40~85°C), it is necessary to include a thermal-isolation stage with a thermal resistivity of 1000s of K/W. Such a vibration and thermal isolation stage can be realized using conventional MEMS materials like glass, as in [54] (Figure 1.8); however, the dimensions of the isolation stage do not tend to be comparable to the sensor dimension, so the system size with the isolation stage becomes uneconomical for many commercial applications.

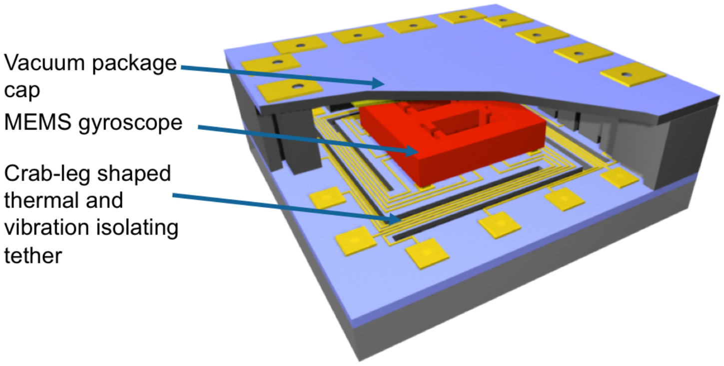

Figure 1.8. HERMIT package containing crab-leg shaped thermal and vibration isolating tethers [107].

The vibration sensitivity can be reduced by differentially canceling the vibration due to environmental effects. In order to distinguish the vibration from the environment from the Coriolis force, a gyro needs to have balanced operating mode shapes, where all linear and rotational momentum of the gyro with respect to the center of the mass sums to be zero. The sensitivity to vibration from environment can be further reduced by increasing the ratio between the parasitic and operating modes. In order to increase this frequency ratio, it is crucial to design a coupling beam that is flexible to a desired movement pattern and is stiff to parasitic mode pattern. More detailed analysis of the vibration and shock sensitivity of the developed gyroscope will be provided in Chapter 7.

1.3. Review of Gyroscope Designs

In order to suppress vibration-induced bias drifts, micro-gyroscopes need to be able to differentially cancel the vibration-induced displacements using balanced drive and sense modes. In the balanced mode, the center of the mass is constant and there is zero net momentum. When the gyro has ideal uniformity (mass, stiffness and damping), the balanced mode cannot be actuated by linear or rotational acceleration from the environment. This section discusses the relationship between the mode shapes and vibration immunity. Analyses will be made using the two most widely adopted designs, the single-mass [8, 13-16, 21, 24, 47, 55-71] and the double-mass designs [4, 6, 25, 72-79]. Structures and characteristics of existing vibration-immune micro-gyroscopes will be analyzed.

1.3.1. Vibration Sensitivity of the Single-Mass Micro-Gyroscope

The single-mass micro-gyroscope typically has a mass at the center of the device and multiple springs that support the mass. The mass is made to oscillate either linearly or angularly along the drive and the sense axes. Figure 1.9 shows the structure of a yaw-rate sensing single-mass micro-gyroscope [80], and Figure 1.10 shows the lumped-mass representation of its drive and sense resonance modes. The net momentum in the resonance modes is determined by the mass and the oscillation velocity, and neither of these resonance modes has zero momentum. Single-mass micro-gyroscopes based on decoupled drive and sense resonance modes are available [21, 55, 57-60, 65, 66, 69, 80], but they also have non-zero momentum for both of their resonance modes.

Suppose the device in Figure 1.9 is subjected to vibrations along the drive (x) axis. The vibration will alter the amplitude of the drive oscillation, change the velocity, and change the magnitude of the Coriolis force leading to an error in the sensed rate of rotation. This situation is shown in Figures 1.11 (a) and (b). The magnitude of the interference reaches the maximum when the vibration frequency is identical to the resonance frequency. When vibration is applied along the driving axis (x), the amplitude change caused by the vibration in the same phase to driving oscillation is restored by amplitude controlling circuitry. When the phase of the applied vibration has a quadrature relationship with the driving motion, the driving control loop automatically adjusts the phase of driving motion to keep the zero phase shift around the loop. As a result, the effect of vibration in the driving loop can be reduced by the interface circuitry. However, when this sensor is subjected to vibration along the sense (y) axis in the same phase with the Coriolis force, the sense (y) axis displacement from vibration becomes indistinguishable from the displacement caused by the Coriolis force. Vibration along the sense axis therefore introduces larger error than the vibration along the drive axis (Figure 1.12). In the next case, effects of vibrations for double-mass micro-gyroscopes will be discussed. That case will show a different trend because double-mass micro-gyroscopes have zero momentum in their drive axes.

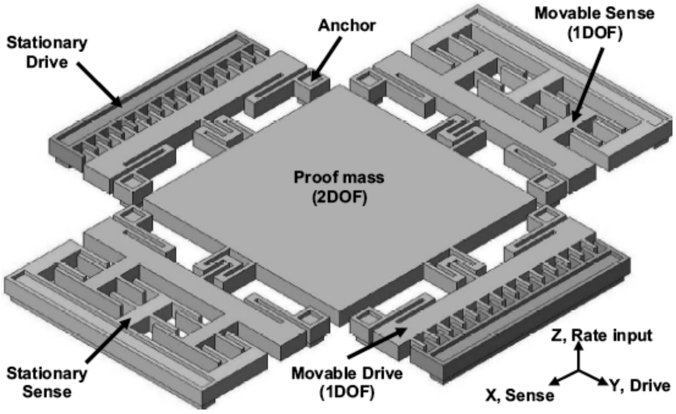

Figure 1.9. Structure of single-mass yaw-sensing micro-gyroscope [80].

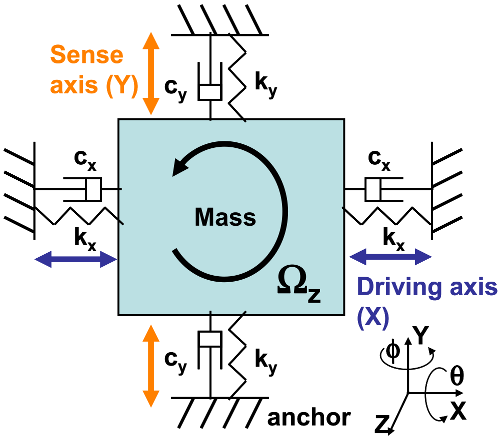

Figure 1.10. Lumped-mass representation of a single-mass yaw- sensing micro-gyroscope.

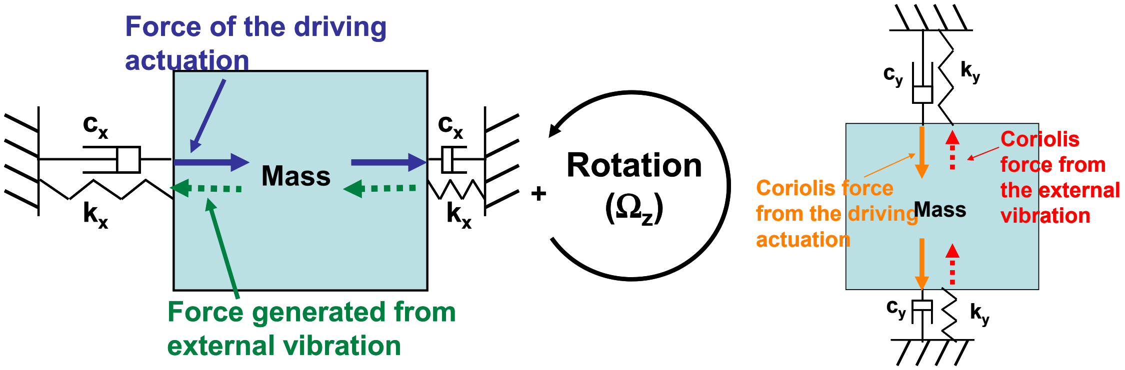

(a) (b)

Figure 1.11. Lumped-mass representations of (a) external vibrations added along the drive (x) axis under a yaw-rotation rate (Ω_z) and (b) change in the Coriolis force.

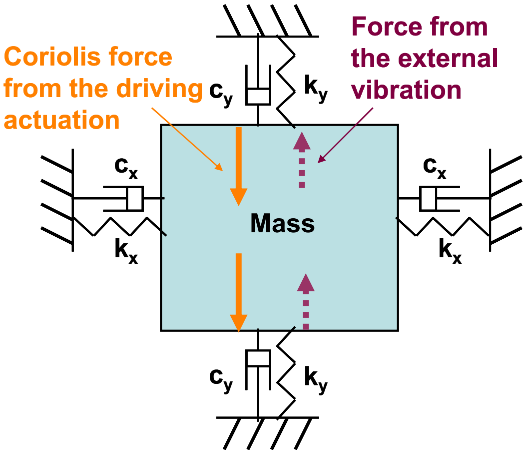

Figure 1.12. Lumped-mass representation of the vibration-induced displacement along the sense (y) axis.

1.3.2. Vibration Sensitivity of the Double-Mass Micro-Gyroscope

The operation principle of the double-mass micro-gyroscope is typically based on that of tuning forks [4, 6, 27, 72-79]. The device consists of two identical masses at equal distances from the center and springs that allow them to move either linearly or angularly along drive and the sense axes. Figure 1.13 shows a yaw-rate-sensing tuning-fork micro-gyroscope which drives the masses along the x-axis and senses the Coriolis force along the y-axis [27]. Figures 1.14 (a) and (b) show the lumped-mass representations of the drive and the sense resonance modes. In the drive mode, the masses oscillate in opposite phase along the centerline of the device with complementary momentums and therefore achieve zero net momentum. In the sense mode, the masses oscillate in opposite phase along the sense (y) axis. However, in this case, the masses oscillate along two different lines that are apart by a certain distance from the center of the device. Therefore, the momentum of masses are not complementary to each other, and there is a net angular momentum along the yaw axis. Double-mass micro-gyroscopes with decoupled drive and sense resonance modes are also available [72, 74], but they also have zero net momentum for their drive resonance modes and non-zero net momentum for their sense resonance modes.

Suppose this device is subjected to vibration along the drive (x) axis. Similarly to the single-mass device, the masses will have extra displacements along the drive (x) axis. However, the displacements are in the same direction, as opposed to complementary directions. In other words, the drive oscillation and the displacement from the external vibration are out-of-phase. Thus, the Coriolis force from the drive oscillation and the Coriolis force from the vibration are also out-of-phase. As a result, the displacement from the vibration is canceled using the sense electrode configuration for measuring the original Coriolis oscillation (Figures 1.15 (a) and (b)). Suppose this device is subjected to angular vibrations along the yaw axis. The masses will then move in the opposite directions along the sense (y) axis. In this case, the displacement is in the same direction as the existing angular momentum, and the displacement by the vibration and displacement by the Coriolis force are not distinguishable (Figure 1.16). Note that the frequency of the yaw-axis angular vibration that introduces noise to the gyro is near the sense mode frequency (>5kHz), which is much higher than the signal that the frequency of rotation that the sensor measures (<100Hz).

Based on the cases above, existing vibratory micro-gyroscopes are categorized according to:

- Whether the device is vulnerable to vibration along both the drive and the sense axes (Type-I), immune to vibration along only the drive axis (Type-II), immune to vibration along only the sense axis (Type-III), or both (Type-IV).
- Whether the device is vulnerable to linear vibration (Type-A) or angular vibration (Type-B).

Tables 1.2 and 1.3 show the result of this categorization.

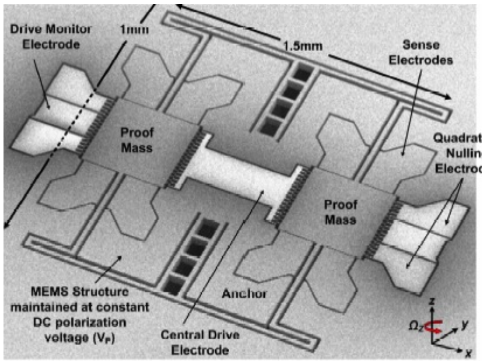

Figure 1.13. Yaw-sensing tuning fork micro-gyroscope [27].

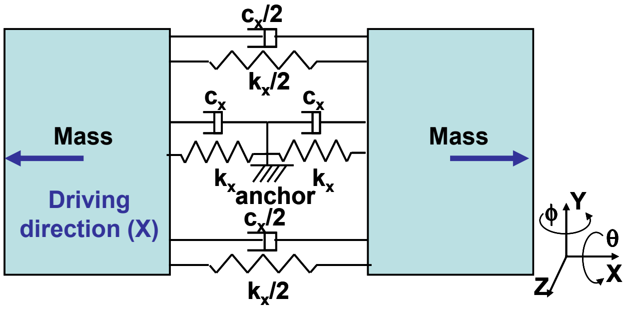

(a) Drive mode

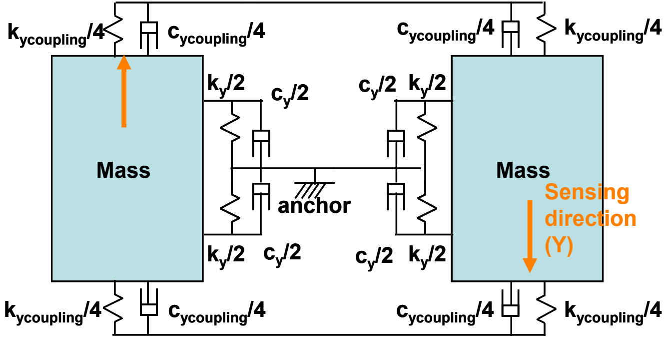

(b) Sense mode

Figure 1.14. Lumped mass representations of the (a) drive and (b) sense modes of double-mass yaw-sensing micro-gyroscope.

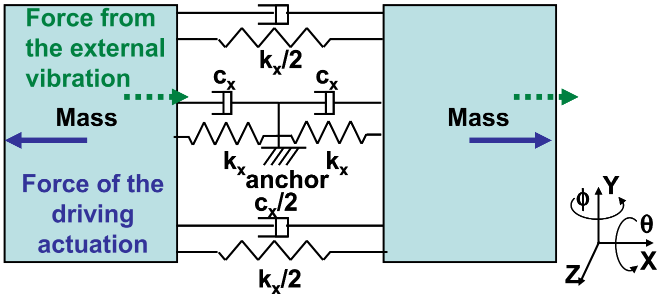

(a) Drive mode

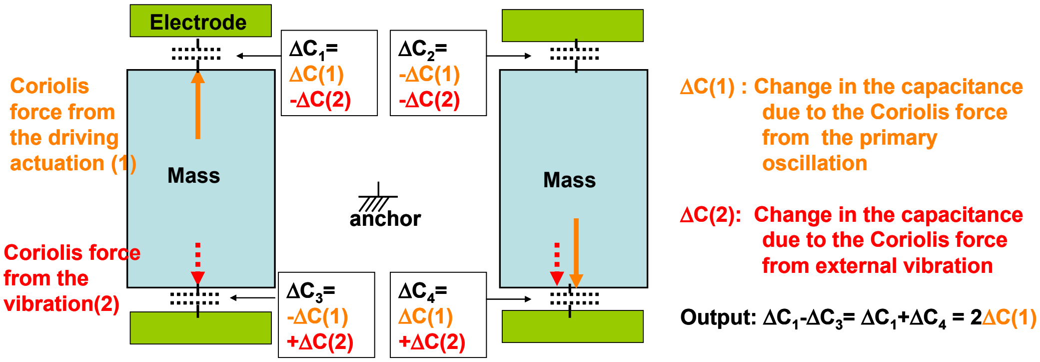

(b) Sense mode

Figure 1.15. Lumped-mass representations of (a) displacement due to vibration along the drive (x) axis and (b) differential cancellation of Coriolis force from external vibration along drive axis (springs and dampers are omitted).

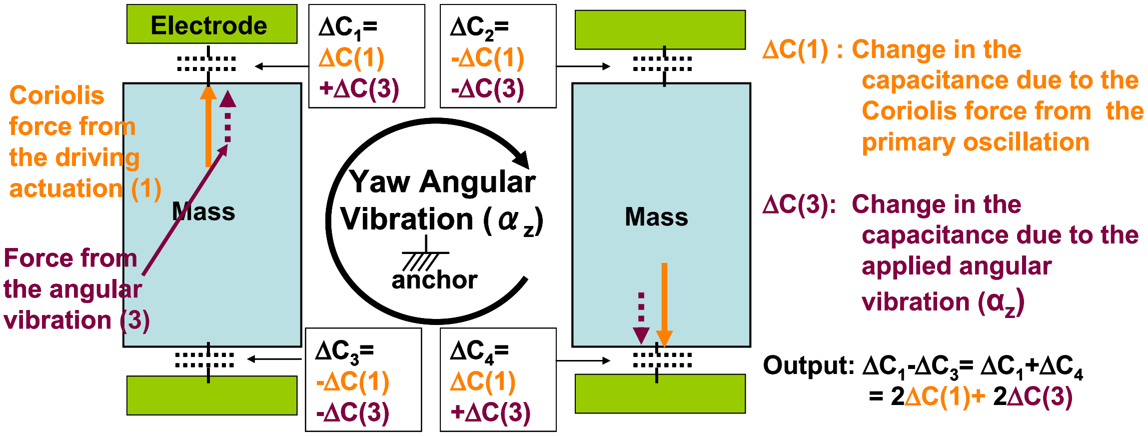

Figure 1.16. Lumped-mass representation of non-cancellable displacement due to yaw angular vibration (springs and dampers are omitted).

Table 1.2. Classification of vibration immunity of a micro-gyroscope

Immunity to vibration according to the drive and the sense axes		Type of vibration which a device is vulnerable to	
Type I	Vulnerable along both the drive and the sensing axes	Type A	Vulnerable to linear vibration
Type II	Cancellable along the drive axis but not on the sense axis		
Type III	Cancellable along the sense axis but not on the drive axis	Type B	Vulnerable to angular vibration
Type IV	Cancellable along both the drive and the sense axes		

Table 1.3. Categorization of the vibratory micro-gyroscopes with respect to the immunity to vibration

Class	References
I-A	[8], [13], [15], [17], [21], [24], [55](MARS-LL), [56]-[70]
I-B	[47], [55](MARS-RR), [71]
I-AB	[16]
II-A	Not found
II-B	[6], [27], [72], [73]-[79]
II-AB	Not found
III-A	Not found
III-B	Not found
III-AB	Not found
IV (Balanced mode devices)	[7], [10], [19], [26], [81]-[87]

1.3.3. Balanced-Mode Gyroscope Designs

There are a few devices that have balanced mode shapes. They are categorized into 1) degenerate-mode balanced gyroscope, 2) non-degenerate-mode balanced gyroscope, and 3) balanced bulk-acoustic-wave (BAW) gyroscope. The designs of these sensors are discussed here.

Degenerate micro-gyroscopes utilize drive and sense resonance modes which ideally occur at the same frequency and have indistinguishable mode shapes. Degenerate mode gyros include those with symmetric shells or volumes, such as hemispheres [29], rings [7, 19], or disks [26]. The ring (Figure 1.17) and the disk (Figure 1.18) micro-gyroscopes measure yaw rates by utilizing the fundamental (*n*=2) or higher (*n*=3) flexural modes, also known as the wineglass mode. In the flexural mode, the position of the center of the mass is conserved, so these are not actuatable with external vibrational input. The displacement pattern of the *n*=2 wineglass mode is shown in Figure 1.19. There are two *n*=2 modes occurring at 45 degrees apart with identical expansion and contraction profiles. The ring and the disk micro-gyroscopes use these modes as their drive and sense resonance modes.

The advantages of this type of device include symmetry of the physical parameters (effective mass, damping, stiffness, actuation and sensing area), simple design, and fewer parasitic modes near the wineglass mode. The degenerate-type gyros are ideal geometry

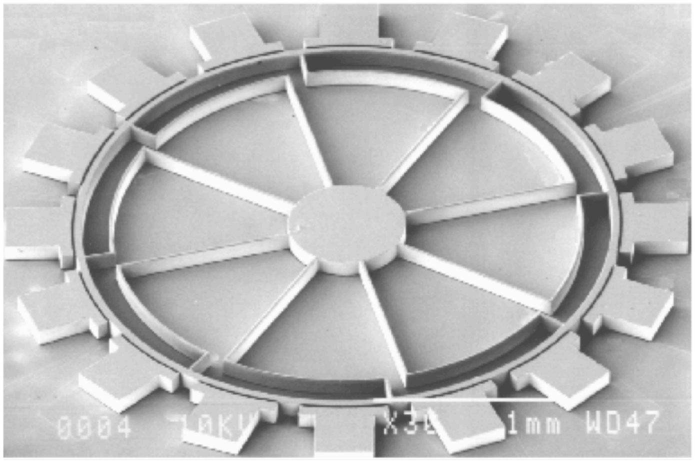

Figure 1.17. SEM picture of vibratory ring gyroscope [19].

for a rate-integrating gyroscope (RIG) due to the innate physical isotropy. The drawbacks of these gyroscopes include lower effective mass compared to its sensor footprint and smaller driving range due to the use of parallel plates.

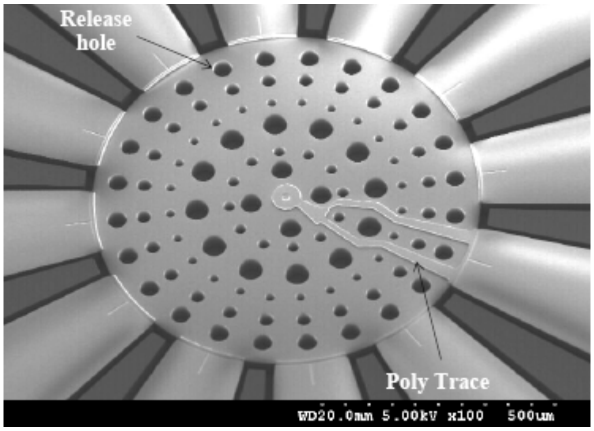

Figure 1.18. SEM picture of bulk acoustic wave disk gyroscope [26].

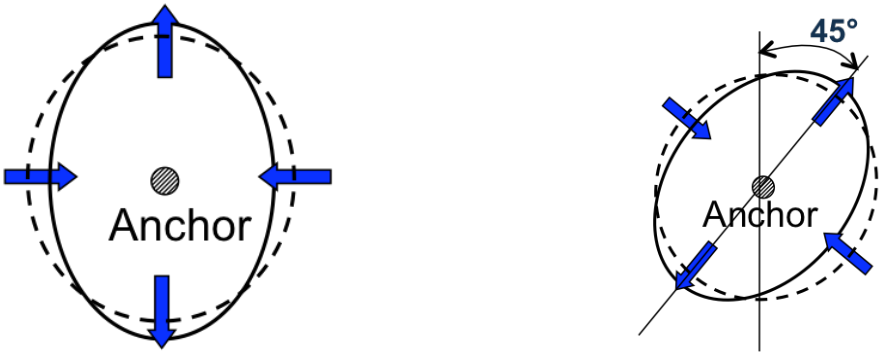

(a) First mode

(b) Second mode
(Separated from first mode by 45 degrees)

Figure 1.19. Displacement pattern of two *n*=2 flexural modes (wineglass modes).

1.4. Non-Degenerate-Type Balanced-Mode Gyroscopes

Non-degenerate micro-gyroscopes use two distinguishable resonance modes that occur at different frequencies. They consist of separate masses and springs, and they have less symmetric shapes compared to degenerate micro-gyroscopes. Previously published examples include the butterfly micro-gyroscope [83, 84], the trident-tuning-fork micro-gyroscope [85], the quad-tuning-fork micro-gyroscope [45, 86], and the balanced bulk-acoustic-wave (BAW) gyroscope [87].

1.4.1. Butterfly Micro-Gyroscope

The butterfly micro-gyroscope measures planar rotation rates. The original butterfly gyroscope was developed by Imego Institute in 1999 (Figure 1.20) [83]. An improved design was developed by researchers at SensNor and SINTEF in 2001 (Figure 1.21) [84].

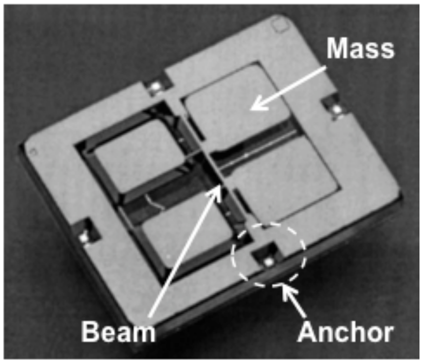

Figure 1.20. Photograph of the Butterfly micro-gyroscope from Imego [83].

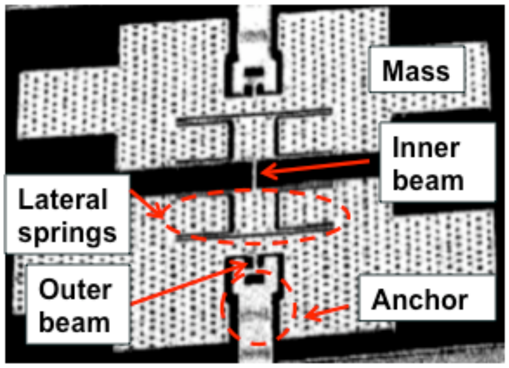

Figure 1.21. SEM picture of the Butterfly micro-gyroscope from SensNor and SINTEF [84].

The device shown in Figure 1.20 consists of two masses, a beam that connects the masses, and anchors that hold both ends of the beam. The device shown in Figure 1.21 improved the former design by adding lateral springs. The drive and sense resonance modes of the two gyros are shown in Figures 1.22 and 1.23, respectively. In the drive mode (Figures 1.22-(a) and Figure 1.23-(a)), the masses angularly oscillate along the z-axis in opposite phase. In the sense mode (Figures 1.22-(b) and 1.23-(b)) (under x-axis rotation rate), the masses angularly oscillate along the y-axis, again in opposite phase.

In the butterfly gyroscope, a straight beam along the y-axis serves as both the drive and sensing springs. The spring is made to be tilted intentionally from the sensor plane (using anisotropic etching and two-step DRIE) so that the masses can be dithered along planar directions using the bottom electrode (Figure 1.24).

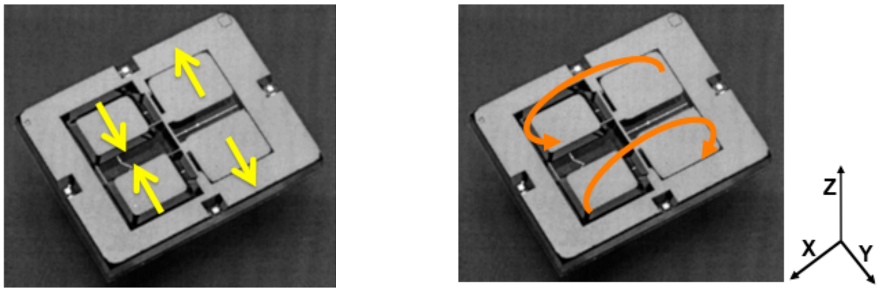

(a) Drive mode (b) Sense mode

Figure 1.22. Resonance mode patterns of the butterfly micro-gyroscope from Imego [83].

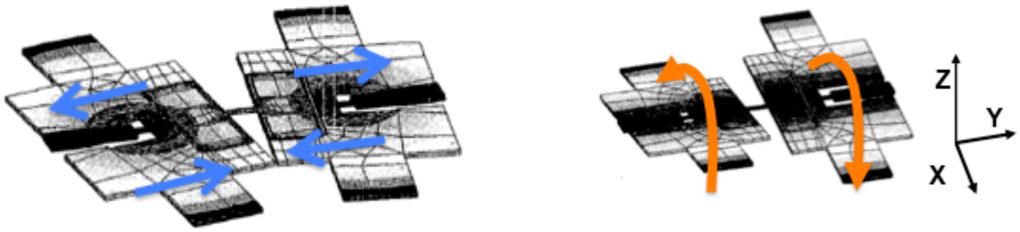

(a) Drive mode (at 9.0 kHz) (b) Sense mode (at 9.3 kHz)

Figure 1.23. Resonance modes of the butterfly micro-gyroscope from SensNor and SINTEF [84].

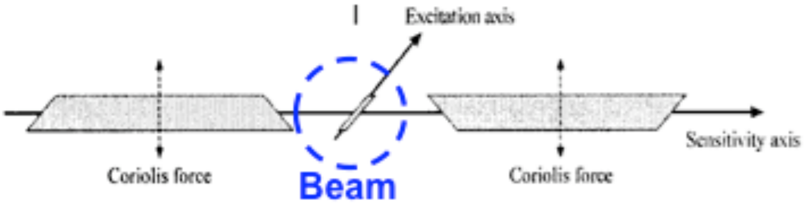

(a) Cross-sectional figure of Imego's butterfly micro-gyroscope (patterned using anisotropic wet etch)

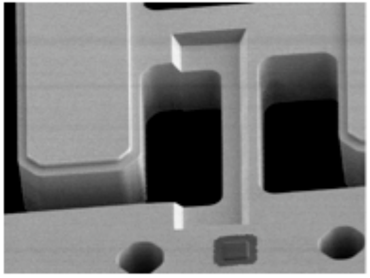

(b) SEM picture near the beam of SensNor and SINTEF's butterfly micro-gyroscope (patterned using DRIE)

Figure 1.24. Illustration and SEM picture of the intentionally-tilted beams.

One of the advantages of the butterfly gyro architecture is that due to the simplicity of the spring design fewer parasitic modes exist. The drawbacks of this design may include geometrical variation due to misalignment of multiple masks used for defining the gyro and possibly larger temperature sensitivity due to clamped-clamped-beam shape of the sensor spring.

1.4.2. Trident-Tuning-Fork Micro-Gyroscope

The trident-tuning-fork gyroscope is a planar micro-gyroscope consisting of three silicon tines of an identical size. It was developed by researchers at Tohoku University in 2000 [85] (Figure 1.25). In the drive resonance mode, the outer tines oscillate in-phase along the z-axis at identical velocities, but the center tine oscillates in opposite-phase at twice their velocities (Figure 1.26-(a)). Under a y-axis rotation rate, the outer tines oscillate in-phase along the x-axis at identical velocities, but the center tine moves in opposite-phase at twice their velocities (Figure 1.26-(b)). It uses both bottom electrodes for driving the tines and sensing the Coriolis oscillation. The advantage of this design is extreme design simplicity. Challenges in this design may include small driving range, mode tuning, and separation of the parasitic modes from drive and sense modes.

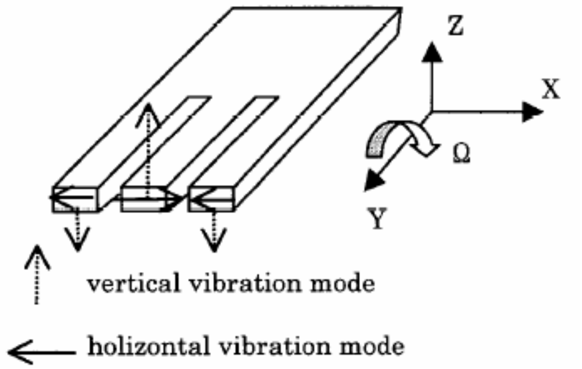

Figure 1.25. Trident tuning-fork micro-gyroscope [85].

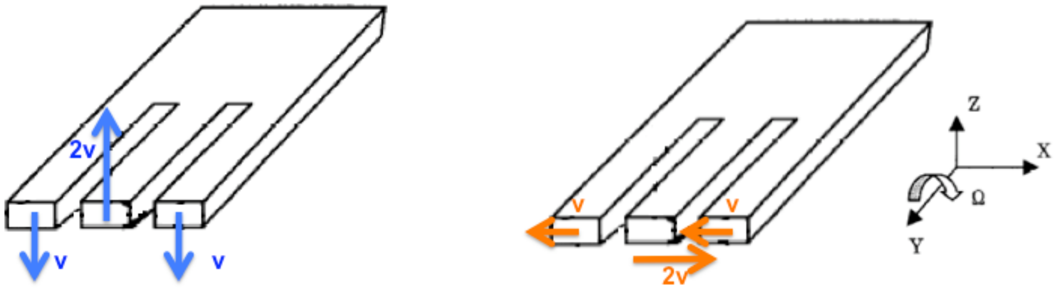

(a) Drive mode (b) Sense mode under y-axis rotation

Figure 1.26. Resonance modes of the trident tuning-fork gyroscope.

1.4.3. Quad-Tuning-Fork Micro-Gyroscope

The quad tuning-fork micro-gyroscope is a yaw gyroscope developed by Analog Devices [86] (Figure 1.27). The gyro is constructed with four framed-masses, coupling springs, and supporting springs. The structure of the framed-mass is identical to the one used for their earlier tuning-fork micro-gyroscope [31]. The framed-mass consists of mass, drive spring, and frame. The mass is allowed to move along the drive (x) axis and kept from moving along the sense (y) axis. The frames are coupled to each other using supporting springs and coupling springs. Figures 1.28-(a) and 1.28-(b) show its drive and sense resonance modes, respectively. In the drive resonance mode, the masses oscillate along the x-axis in the opposite phases to the adjacent ones. Under a yaw rotation rate, the masses oscillate along the y-axis in opposite phases to the adjacent ones. A similar quad-mass gyroscope architecture is used by researchers at UC Irvine as a rate-integrating gyroscope (Figure 1.29) [45]. The Irvine gyro was designed to be exactly symmetric along the x- and y- axes, so that the resonance frequencies for the two operating modes are ideally the same. The Irvine gyro operates at 2kHz, where Si has a high quality factor (*Q*) due to lower thermoelastic damping (TED). They have demonstrated a Q of 1.6 million (decay time comstant of 150 seconds), which remains the highest reported damping time among the presented Si resonators.

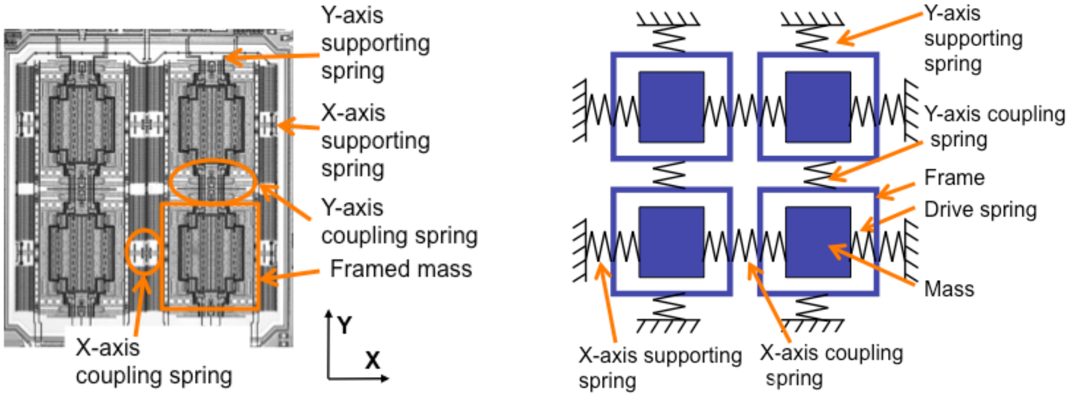

(a) Die photo

(b) Simplified mechanical model (Some anchors are omitted)

Figure 1.27. Die photograph and simplified mechanical model of Analog Device's quad tuning-fork micro-gyroscope [86].

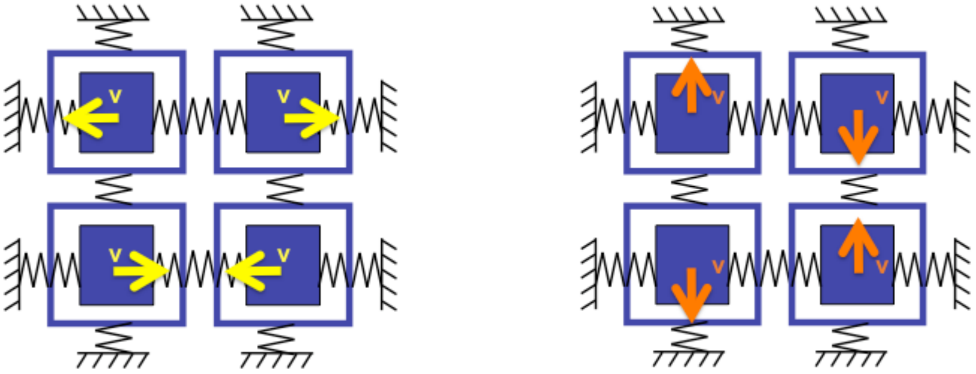

(a) Drive mode

(b) Sense mode under yaw rotation

Figure 1.28. Resonance modes of the quad tuning-fork micro-gyroscope (some of the anchors are omitted).

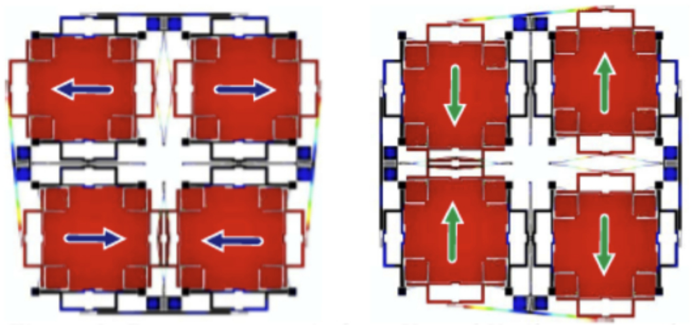

Figure 1.29. Drive and sense modes of UC Irvine's quad mass tuning-fork gyroscope [45].

The attractive features of this design include mode-decoupling and large sensing and actuation area. Drawbacks of this design include design complexity and number of coupling springs that increase the number of parasitic modes.

1.5. Balanced Bulk-Acoustic-Wave (BAW) Gyroscope

Similar to the balanced electrostatic gyroscopes mentioned above, balanced modes can be found from a solid piece of a piezoelectric material. One example is the PZT bulk-acoustic-wave (BAW) gyroscope, developed by researchers at Hyogo University [87] (Figure 1.30). This gyroscope uses the 29th mode of a PZT block ($3\times4\times5\text{mm}^3$), located at 415kHz (Figure 1.30). In this mode, mass components of the PZT block displace symmetrically along x-axis, with respect to the center plane of the block. Under y-axis rotation, due to the Coriolis force, compressive and extensive stresses develop at different parts of the mass. The direction of the stress aligns with the polarization of the PZT block and output voltage is developed. The driving, driving readout, and sensing electrodes are patterned on the top and bottom surface of the block. Since the drive mode is a balanced mode, the developed z-axis stress is also balanced with respect to the center of the mass. In addition, the gyro operates at a high frequency range, where the environmental noise density is low. The gyroscope is attractive in terms of design and packaging. The drawbacks of this design include low Q, small driving distance and effective mass. Unlike the other vibratory gyroscopes, this gyroscope does not have a resonance to amplify the Coriolis force along the sense axis. Therefore, this gyro may not be suitable for high-accuracy applications.

Figure 1.30. Photograph of the PZT bulk-acoustic wave (BAW) gyroscope [87].

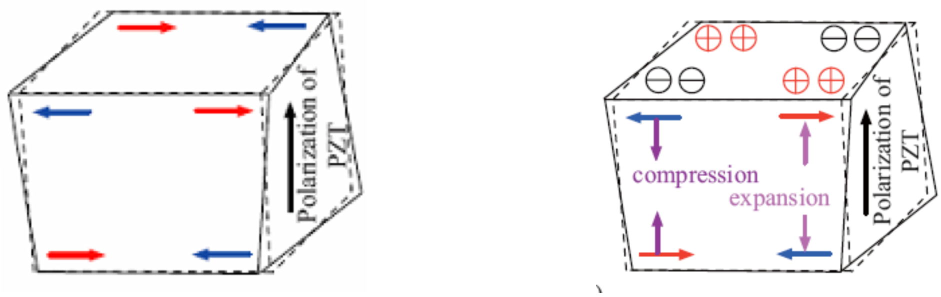

(a) Drive mode (b) Direction of Coriolis force (in purple)

Figure 1.31. Resonance modes of the BAW PZT micro-gyroscope [87].

1.6. Research Objective

The goal of the presented work is to understand the performance-limiting factors of conventional MEMS gyroscopes and to develop, fabricate, and demonstrate new gyro designs that will lead to better performance in real applications. Another goal of this research is to develop a rate-integrating gyroscope (RIG) to overcome the issue of the tradeoff between resolution to bandwidth and full-scale factor for conventional rate-sensing gyroscopes (RG).

The devices are designed to operate in balanced modes. In the balanced modes, the momentum of the sum of the mass always exists at the center of the device. The gyro can fully differentially cancel in-phase acceleration from environment. The gyros are designed to achieve large ratios between parasitic mode and the operating mode to reduce the sensitivity to environmental vibration under mismatch in mass and stiffness from manufacturing imperfection and to increase shock resistivity. The devices have a single anchor at the center of the device, minimizing the development of thermoresidual stress from temperature fluctuation.

We develop two types of gyroscopes: the Balanced Oscillating Gyroscope (BOG) and the Cylindrical Rate-Integrating Gyroscope (BOG). The BOG is a planar-rate-sensing quad-mass tuning-fork gyroscope. The CING is a whole-angle-mode gyroscope. We analyze the design of the gyros using finite element method (FEM) extensively to improve their frequency characteristics. We study the dominant energy loss mechanism of the gyro. The gyroscopes are made using Si-on-glass (SOG) process to achieve large *Q*, large transduction area, and small parasitic capacitance. We demonstrate the feasibility of these gyroscopes by controlling them using off-chip interface circuitry.

1.7. Contribution

The presented research provides the following contributions:

- Analysis of gyro parameters for low vibration sensitivity and large quality factor (*Q*).
- Development of new gyroscope architectures, namely the Balanced Oscillating Gyroscope (BOG) and the Cylindrical Rate-Integrating Gyroscope (CING), aimed for low environmental sensitivity.
- Understanding the performance limits of the BOG and CING and extending performance through appropriate selection of device structure and fabrication technology.

- Improvement of the Si-on-glass (SOG) process for creating high-aspect ratio single crystal-Si sensors for the BOG and CING, with low parasitic capacitance, high-*Q*, self-alignment, and in the future, easier vacuum packagibility.
- Demonstration of sensor operation, including:
    - CING: demonstration of perfectly axisymmetric and self-aligned MEMS sensor aimed at rate-integrating applications, with small original mode mismatch (<10Hz), long decay time (~10 seconds), and large transduction area. Operation in both rate-sensing mode (closed-loop) and rate-integration mode.
    - BOG: demonstration of preliminary sensor characteristics.

1.8. Organization of Thesis

Chapter 1 presents the objectives and contributions of the proposed research. Chapter 2 explains the physics of the rate gyroscope (RG) and rate-integrating gyroscope (RIG) and compares them from the standpoint of critical error sources and design. Chapter 3 discusses the steps to calculate the physical parameters (effective mass, angular gain, centrifugal mass) of a 3-dimensional wineglass mode gyroscope using FEM. Chapter 4 discusses the design, fabrication, and evaluation of the Balanced Oscillating Gyroscope (BOG). Chapter 5 discusses the design, fabrication and evaluation of the first-generation (high-frequency) Cylindrical Rate-Integrating Gyroscope (CING). Chapter 6 discusses the design, fabrication, and evaluation of the second-generation (low-frequency) CING. In Chapter 7, the relationship between the vibration sensitivity of BOG and CING under mechanical anisotropy and their mode characteristics is studied. Chapter 8 summarizes the presented research and discusses future work. Appendix A derives the stiffness and damping coefficients of a gyro along an arbitrary sensor axis that is separated from fundamental stiffness and damping axes. Appendix B shows the ANSYS simulation codes used for analyzing physical parameters of 3D wineglass mode gyroscopes. Appendix C discusses the design of the vertical comb-drive (VC) electrode developed using the Si-on-Glass (SOG) process.

CHAPTER 2.

THEORY OF VIBRATORY RATE- AND RATE-INTEGRATING GYROSCOPES

A mechanical can gyroscope can be controlled to measure rotation rate or rotation angle. Depending on whether a gyro measures rates or angles, the gyro can be categorized as the rate gyro (RG) or the rate-integrating gyro (RIG). The operating principles of the RG and RIG are similar in many aspects. In this chapter, the motion equations for the two types of gyroscopes will be described, control methods for RG and RIG will be compared, and typical sources of error of the RG and RIG will be described.

2.1. Basics of Rate and Rate-Integrating Mode Operation

A rate-integrating gyroscope (RIG) measures rotation angle from the precession angle between the direction of the moving vibration pattern and a reference point on the rotated coordinate. The phenomenon that the gyro's linear or rotational movement lags the input rotation is called precession. Precession can be understood by viewing from both the inertial frame and the rotating frame. First, from the inertial frame, from Newton's First Law, an ideal gyro with isotropic stiffness (k) and damping (c) along the two principal axes oscillates along a fixed direction. The oscillation is unaffected by rotation of the rotating frame. Thus, one can simply measure rotated angle from the angle between the oscillation direction and a reference point on the rotating frame.

When viewing from the rotating frame, we can understand precession as continuous energy transfer between motions along the two principal axes through the Coriolis force. The momentum of the gyro mass can be projected onto the two principal axes. The momentum along one axis is deviated by the Coriolis force that is proportional to the velocity along the other axis. Unless the change in the momentum on one axis is canceled by a reaction force from a control system, the momentum will continue to deviate under continued rotation due to the Coriolis force. One can read the rotated angle from ratio of the momentum in the two principal axes.

An example of the angular measurement using an ideal Foucault pendulum is described in Figure 2.1. The pendulum is located on a rotation table. At the initial time point (t_o), the swinging pattern aligns with the axis 0°-180°. The stage rotates by 30 degrees between t_o and t_1. The swinging pattern is viewed both from Camera 1, located on the ceiling (inertial coordinate), and Camera 2, located right above the center point of the rotating stage. Figure 2.2 illustrates the swinging pattern at t_o and t_1. The direction of the swinging pattern does not change, and one can calculate the precessed angle by reading the change in the tick on the rotating stage that aligns with the reference point on the inertial coordinate. The precessed angle can be read from Camera 2 (Figure 2.3). Figure 2.3-(a) illustrates the original swinging pattern at t_o; Figure 2.3-(b) illustrates the path of the swinging motion at a time between t_o and t_1; and Figure 2.3-(c) illustrates the swinging pattern at t_1. The precessed angle can be calculated from the change of the angle read by the ruler on the stage. In the actual RIG, control circuitry is required to cancel the effect of non-ideal properties of the gyroscope.

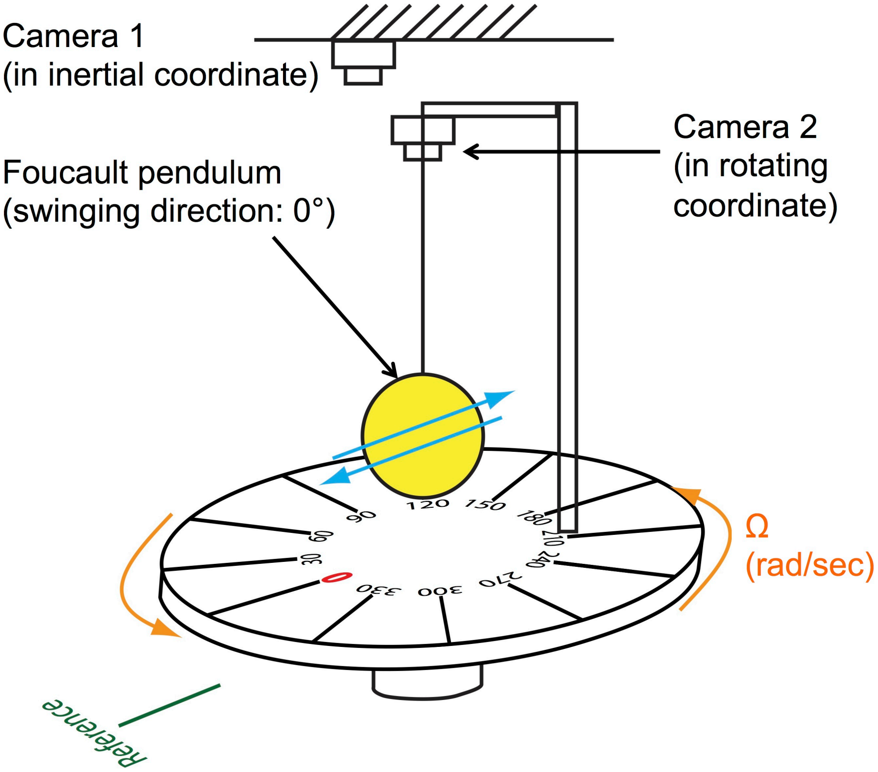

Figure 2.1. Illustration of ideal Foucault pendulum located on rotation table, spinning at a constant rate *Ω*. The swinging pattern is viewed from Camera 1 (in inertial coordinate) and Camera 2 (in rotating coordinate).

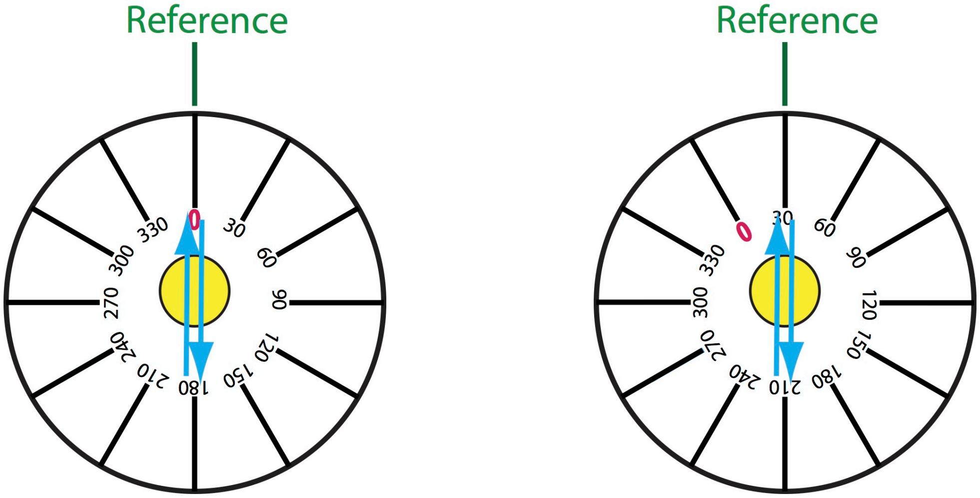

(a) Swing direction at t_o (b) Swinging direction at t_1

Figure 2.2. Precession of swinging pattern of a Foucault pendulum seen by Camera1 (from inertial space): (a) at initial time point (t_o) and (b) time point (t_1) when the stage has rotated by 30 degrees.

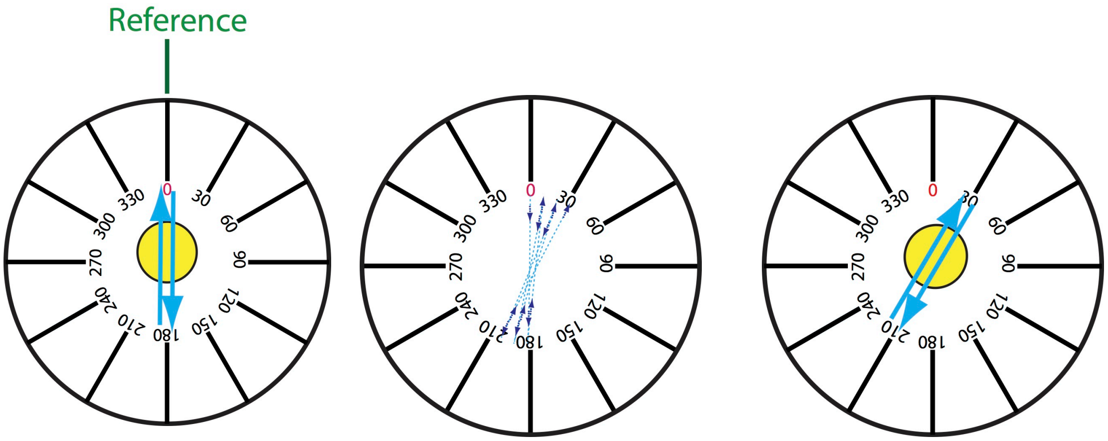

(a) Swinging direction at t_o (b) Swinging path between t_o and t_1 (c) Swinging path at t_1

Figure 2.3. Precession of swinging pattern of a Foucault pendulum, seen from Camera 2 (in rotating coordinate): (a) at initial time point (t_o), (b) between t_o and t_1, and (c) time point (t_1) when the stage has rotated by 30 degrees.

The RG measures the rotation rate, which is proportional to the Coriolis force. Any RIG can operate as a RG, when the vibrating pattern is held along a fixed direction using feedback control. The feedback force to prevent precession is directly proportional to the Coriolis force. This kind of operation mode is called closed-loop rate-sensing mode. The RG can also operate in the open-loop mode without force balancing if damping is allowed to cancel the momentum on only one axis.

The choice of RIG or RG mode operation affects a number of different sensor characteristics. The RIG achieves wider bandwidth and full-scale range than the RG, and these parameters are not related to Q as they are in RG. However, the angular accuracy of the RIG is limited by mechanical anisotropy which is difficult to control. In both open-loop and closed-loop RG, the bandwidth and the full-scale range are degraded as Q increases. The bandwidth and the full-scale range for the closed-loop RG are larger than those of the open-loop RG, because the effective sense-mode Q of the sensor under force-feedback is smaller than the open-loop Q.

In the next section, the physics of the general vibratory gyro will be described, and the dynamic characteristics of the RIG and RG will be compared.

2.2. Dynamics of Vibratory Rate- and Rate-Integrating Gyroscopes

2.2.1. General Two-Dimensional Motion Equation

The physics for both the rate-integrating gyroscope (RIG) and rate gyroscope (RG) are described using two-dimensional Lagrange equations, which are coupled by the Coriolis force. The vibrating motion in the Cartesian coordinate is expressed as the sum of the product of the normalized mode shape parameters (ϕ_{x1}, ϕ_{y1}, ϕ_{z1}, ϕ_{x2}, ϕ_{y2}, ϕ_{z2}) and the generalized displacement of the two modes (q_1, q_2).

$$u_x = \phi_{x1} q_1 + \phi_{x2} q_2 \qquad \text{(Equation 2.1)}$$

$$u_y = \phi_{y1} q_1 + \phi_{y2} q_2 \qquad \text{(Equation 2.2)}$$

$$u_z = \phi_{z1} q_1 + \phi_{z2} q_2 \qquad \text{(Equation 2.3)}$$

The axes where the generalized displacements are calculated are named the q_1- and q_2- axes, and since the vibrating pattern of the whole location of the device can be calculated by knowing the displacements along these axes, they are named the principal axes of motion. For a Foucault pendulum gyroscope, since the motion is described as the sum of linear vibrating mode of a solid mass along x- and y- axes, the generalized displacements (q_1, q_2) are simply u_x and u_y. In the case of a fundamental (n=2) flexural mode (wineglass mode) gyro, the shell serves both as a mass and the spring, so the shape factors (ϕ_{x1}, ϕ_{x2}, ϕ_{y1}, ϕ_{y2}) are not equal to 1. In this mode, q_1 and q_2 are the displacement along the two n=2 flexural modes, which are separated by 45 degrees in the Cartesian coordinate.

The stiffness along any direction in the 2-DOF system is determined by two stiffness parameters [7]. Since the stiffness of the entire system is determined by these two parameters, the axes where the maximum and minimum stiffness are aligned are called the principal elasticity axes. The relationship between the principal elasticity axes and the principal motion axes are shown in Figure 2.4. In this figure, the motion axes are rotated from the sensor axes by an angle θ_ω. Similarly to the elasticity axes, the axes where the largest and smallest damping factors are located are called the principal damping axes. Figure 2.5 illustrates the principal damping axis of a Foucault pendulum, which are separated from the sensor axes by an angle θ_τ.

The stiffness parameters along the principal motion axes can be calculated with a coordinate transform as a two-by-two matrix, containing on-axis and off-axis stiffness terms. These equations are found from applying an arbitrary displacement along the principal stiffness to generate a certain mechanical energy ($E_{stiffness}$) and performing coordinate transfer between the sensor coordinate and the principal stiffness coordinate.

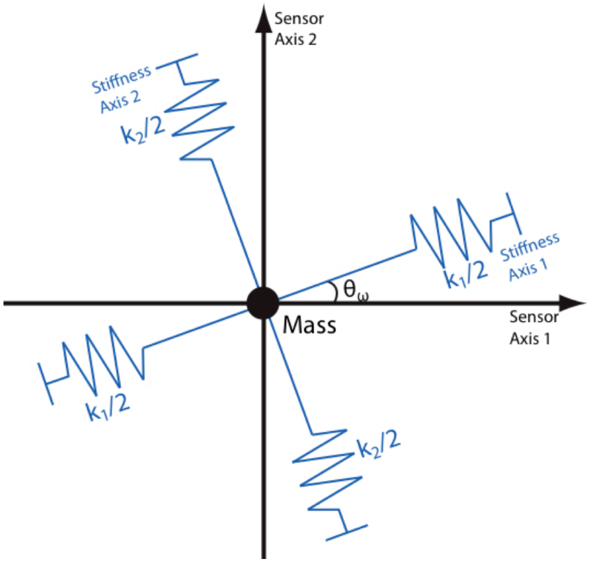

Figure 2.4. Principal elasticity axes, separated from motion axes sensor axes by θ_ω.

The in-axis stiffness terms along the two axes in the sensor coordinate are named k_{11}, k_{12}, respectively. The cross-axial stiffness terms between the two axes are named k_{12} and k_{21}. The stiffness matrix for the Foucault pendulum gyro is found as:

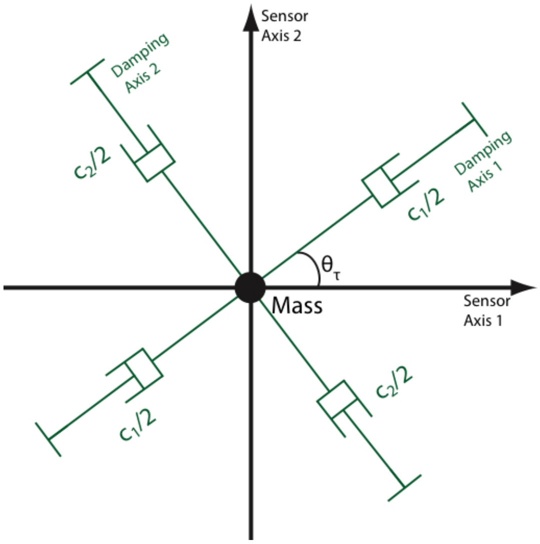

Figure 2.5. Principal damping axes, separated from the sensor axes by θ_τ.

The stiffness parameters along the principal motion axes can be calculated with a coordinate transform as a two-by-two matrix, containing on-axis and off-axis stiffness terms. These equations are found from applying an arbitrary displacement along the principal stiffness to generate a certain mechanical energy ($E_{stiffness}$) and performing coordinate transfer between the sensor coordinate and the principal stiffness coordinate.

The in-axis stiffness terms along the two axes in the sensor coordinate are named k_{11}, k_{12}, respectively. The cross-axial stiffness terms between the two axes are named k_{12} and k_{21}. The stiffness matrix for the Foucault pendulum gyro is found as:

$$\begin{bmatrix} k_{11} & k_{12} \\ k_{21} & k_{22} \end{bmatrix} = \begin{bmatrix} \cos^2\theta_\omega k_1 + \sin^2\theta_\omega k_2 & \cos\theta_\omega \sin\theta_\omega (k_1 - k_2) \\ \cos\theta_\omega \sin\theta_\omega (k_1 - k_2) & \sin^2\theta_\omega k_1 + \cos^2\theta_\omega k_2 \end{bmatrix} \qquad \text{(Equation 2.4)}$$

$$k_{11} = \frac{\partial}{\partial q_1}\left(\frac{\partial E_{stiffness}}{\partial q_1}\right) \qquad \text{(Equation 2.5)}$$

$$k_{12} = k_{21} = \frac{\partial}{\partial q_1}\left(\frac{\partial E_{stiffness}}{\partial q_2}\right) \qquad \text{(Equation 2.6)}$$

$$k_{22} = \frac{\partial}{\partial q_2}\left(\frac{\partial E_{stiffness}}{\partial q_2}\right) \qquad \text{(Equation 2.7)}$$

The damping parameter matrix along the principal motion axes can be found by applying a damping energy (*E_{damping}*) with respect to the principal damping coordinate and performing a coordinate transformation between the sensor coordinate to the principal damping coordinate. The in-axis damping terms along the two axes in the sensor coordinate are named c_{11} and c_{12}, respectively. The cross-axial damping terms between the two axes are named c_{12} and c_{21}. The damping matrix for the Foucault pendulum gyro is found as:

$$\begin{bmatrix} c_{11} & c_{12} \\ c_{21} & c_{22} \end{bmatrix} = \begin{bmatrix} \cos^2\theta_\tau c_1 + \sin^2\theta_\tau c_2 & \cos\theta_\tau \sin\theta_\tau (c_1 - c_2) \\ \cos\theta_\tau \sin\theta_\tau (c_1 - c_2) & \sin^2\theta_\tau c_1 + \cos^2\theta_\tau c_2 \end{bmatrix} \qquad \text{(Equation 2.8)}$$

$$c_{11} = \frac{\partial}{\partial \dot{q}_1}\left(\frac{\partial E_{damping}}{\partial q_1}\right) \qquad \text{(Equation 2.9)}$$

$$c_{12} = \frac{\partial}{\partial \dot{q}_1}\left(\frac{\partial E_{damping}}{\partial q_2}\right) \qquad \text{(Equation 2.10)}$$

$$c_{21} = \frac{\partial}{\partial \dot{q}_2}\left(\frac{\partial E_{damping}}{\partial q_1}\right) \qquad \text{(Equation 2.11)}$$

$$c_{22} = \frac{\partial}{\partial \dot{q}_2}\left(\frac{\partial E_{damping}}{\partial q_2}\right) \qquad \text{(Equation 2.12)}$$

The derivation of stiffness and damping matrices that are separated from the principal stiffness and damping coordinates by θ_ω and θ_τ, respectively, is shown in Appendix A. In the calculation of the 2D motion equation, the inertial force, elastic force, damping, Coriolis force, centrifugal force, and angular acceleration are considered [7]. The 2D Lagrangian equation is summarized in Equation 2.13. Detail derivation of effective mass (M), Corioliolis mass (γ), and centrifugal mass (α, β, μ) to the two-dimensional gyroscope is found in [7]. The expanded derivation of these parameters accounting for 3D motional patterns instead of 2D patterns is shown in Chapter 3.

$$\overset{\text{Mass}}{\begin{bmatrix} M_1 & 0 \\ 0 & M_2 \end{bmatrix}}\begin{Bmatrix} \ddot{q}_1 \\ \ddot{q}_2 \end{Bmatrix} + \overset{\text{Damping}}{\begin{bmatrix} c_{11} & c_{12} \\ c_{21} & c_{22} \end{bmatrix}}\begin{Bmatrix} \dot{q}_1 \\ \dot{q}_2 \end{Bmatrix} + \overset{\text{Coriolis coupling}}{\begin{bmatrix} 0 & -2\gamma\Omega_z \\ 2\gamma\Omega_z & 0 \end{bmatrix}}\begin{Bmatrix} \dot{q}_1 \\ \dot{q}_2 \end{Bmatrix}$$

$$+ \overset{\text{Angular acceleration}}{\begin{bmatrix} 0 & -\gamma\dot{\Omega}_z \\ \gamma\dot{\Omega}_z & 0 \end{bmatrix}}\begin{Bmatrix} \dot{q}_1 \\ \dot{q}_2 \end{Bmatrix} + \overset{\text{Centrifugal stiffness}}{\begin{bmatrix} K_{c1} & 0 \\ 0 & K_{c2} \end{bmatrix}}\begin{Bmatrix} q_1 \\ q_2 \end{Bmatrix} + \overset{\text{Stiffness}}{\begin{bmatrix} k_{11} & k_{12} \\ k_{21} & k_{22} \end{bmatrix}}\begin{Bmatrix} q_1 \\ q_2 \end{Bmatrix} = \overset{\text{Input force}}{\begin{Bmatrix} f_1 \\ f_2 \end{Bmatrix}}$$

(Equation 2.13)

- q_1, q_2: Generalized displacement.

$$u_x = \phi_{x1}q_1 + \phi_{x2}q_2 \qquad \text{(Equation 2.14)}$$

$$u_y = \phi_{y1}q_1 + \phi_{y2}q_2 \qquad \text{(Equation 2.15)}$$

$$u_z = \phi_{z1}q_1 + \phi_{z2}q_2 \qquad \text{(Equation 2.16)}$$

- M_1, M_2: Effective mass of two modes.

$$M_1 = \int \rho\left(\phi_{x1}^2 + \phi_{y1}^2 + \phi_{z1}^2\right)dV \qquad \text{(Equation 2.17)}$$

$$M_2 = \int \rho\left(\phi_{x2}^2 + \phi_{y2}^2 + \phi_{z2}^2\right)dV \qquad \text{(Equation 2.18)}$$

- k_{ij} matrix: Effective stiffness with respect to the sensor axis.

$$\begin{bmatrix} k_{11} & k_{12} \\ k_{21} & k_{22} \end{bmatrix} = \begin{bmatrix} \cos^2\theta_\omega k_1 + \sin^2\theta_\omega k_2 & \cos\theta_\omega \sin\theta_\omega (k_1 - k_2) \\ \cos\theta_\omega \sin\theta_\omega (k_1 - k_2) & \sin^2\theta_\omega k_1 + \cos^2\theta_\omega k_2 \end{bmatrix} \qquad \text{(Equation 2.19)}$$

- c_{ij} matrix: Effective damping coefficients with respect to the sensor axis.

$$\begin{bmatrix} c_{11} & c_{12} \\ c_{21} & c_{22} \end{bmatrix} = \begin{bmatrix} \cos^2\theta_\tau c_1 + \sin^2\theta_\tau c_2 & \cos\theta_\tau \sin\theta_\tau (c_1 - c_2) \\ \cos\theta_\tau \sin\theta_\tau (c_1 - c_2) & \sin^2\theta_\tau c_1 + \cos^2\theta_\tau c_2 \end{bmatrix} \quad \text{(Equation 2.20)}$$

- γ: Coriolis mass

$$\gamma = \int \rho\left(\phi_{x1}\phi_{y2} - \phi_{y1}\phi_{x2}\right)dV \quad \text{(Equation 2.21)}$$

- K_{ij}: Centrifugal stiffness of two modes.

$$K_{c1} = -\alpha_1\Omega_x^2 - \beta_1\Omega_y^2 - \mu_1\Omega_z^2 \quad \text{(Equation 2.22)}$$

$$K_{c2} = -\alpha_2\Omega_x^2 - \beta_2\Omega_y^2 - \mu_2\Omega_z^2 \quad \text{(Equation 2.23)}$$

- α, β, μ: Centrifugal mass of two modes.

$$\alpha_1 = \int_V \rho(\phi_{y1}^2 + \phi_{z1}^2)dV \quad \text{(Equation 2.24)}$$

$$\alpha_2 = \int_V \rho(\phi_{y2}^2 + \phi_{z2}^2)dV \quad \text{(Equation 2.25)}$$

$$\beta_1 = \int_V \rho(\phi_{x1}^2 + \phi_{z1}^2)dV \quad \text{(Equation 2.26)}$$

$$\beta_2 = \int_V \rho(\phi_{x2}^2 + \phi_{z2}^2)dV \quad \text{(Equation 2.27)}$$

$$\mu_1 = \int_V \rho(\phi_{x1}^2 + \phi_{y1}^2)dV \quad \text{(Equation 2.28)}$$

$$\mu_2 = \int_V \rho(\phi_{x2}^2 + \phi_{y2}^2)dV \quad \text{(Equation 2.29)}$$

In Equation 2.13, the parameters M, α, β, and γ are related to the mass distribution of the resonator and are dependent on the mode shapes. Especially, M is named as the effective mass, and it relates to the amount of inertia it creates; whereas γ is named the Coriolis mass, which is the amount of effective mass that creates the Coriolis force under rotation.

2.2.2. Specific Case for Gyros with Identical Effective Mass

Equation 2.13 can be further simplified in the case of the RIG whereas due to the mechanical isotropy, the effective masses along the two axes are typically identical. In addition, some of the parameters in the general motion equation can be related to more physically meaningful terms of resonance frequencies (ω) and decay time constants (τ) as:

$$k_1 = \omega_1^2 M \qquad \text{(Equation 2.30)}$$

$$k_2 = \omega_2^2 M \qquad \text{(Equation 2.31)}$$

$$\tau_1 = \frac{2M}{c_1} \qquad \text{(Equation 2.32)}$$

$$\tau_2 = \frac{2M}{c_2} \qquad \text{(Equation 2.33)}$$

Using these parameters, the motion equation for the RIG can be further developed as shown in Equation 2.34 [88]:

Mass Damping

$$\begin{bmatrix} 1 & 0 \\ 0 & 1 \end{bmatrix} \begin{Bmatrix} \ddot{q}_1 \\ \ddot{q}_2 \end{Bmatrix} + \begin{bmatrix} \left(\frac{2}{\tau}\right) + \cos 2\theta_\tau \left(\Delta \frac{1}{\tau}\right) & \sin 2\theta_\tau \left(\Delta \frac{1}{\tau}\right) \\ \sin 2\theta_\tau \left(\Delta \frac{1}{\tau}\right) & \left(\frac{2}{\tau}\right) - \cos 2\theta_\tau \left(\Delta \frac{1}{\tau}\right) \end{bmatrix} \begin{Bmatrix} \dot{q}_1 \\ \dot{q}_2 \end{Bmatrix}$$

Coriolis coupling Angular acceleration

$$+ \frac{1}{M} \begin{bmatrix} 0 & -2\gamma\Omega_z \\ 2\gamma\Omega_z & 0 \end{bmatrix} \begin{Bmatrix} \dot{q}_1 \\ \dot{q}_2 \end{Bmatrix} + \frac{1}{M} \begin{bmatrix} 0 & -\gamma\dot{\Omega}_z \\ \gamma\dot{\Omega}_z & 0 \end{bmatrix} \begin{Bmatrix} \dot{q}_1 \\ \dot{q}_2 \end{Bmatrix}$$

Centrifugal stiffness Stiffness

$$+ \begin{bmatrix} -\Omega_z^2 & 0 \\ 0 & -\Omega_z^2 \end{bmatrix} \begin{Bmatrix} q_1 \\ q_2 \end{Bmatrix} + \begin{bmatrix} \omega^2 + \omega\Delta\omega \cos 2\theta_\omega & \omega\Delta\omega \cos 2\theta_\omega \\ \omega\Delta\omega \cos 2\theta_\omega & \omega^2 + \omega\Delta\omega \cos 2\theta_\omega \end{bmatrix} \begin{Bmatrix} q_1 \\ q_2 \end{Bmatrix}$$

Input force

$$= \frac{1}{M} \begin{Bmatrix} f_1 \\ f_2 \end{Bmatrix}$$

(Equation 2.34)

$$\frac{1}{\tau} \equiv \frac{1}{2}\left(\frac{1}{\tau_1} + \frac{1}{\tau_2}\right) \quad \text{(Equation 2.35)}$$

$$\Delta \frac{1}{\tau} = \frac{1}{\tau_1} - \frac{1}{\tau_2} \quad \text{(Equation 2.36)}$$

$$\omega^2 = \frac{\omega_1^2 + \omega_2^2}{2} \quad \text{(Equation 2.37)}$$

$$\omega\Delta\omega = \frac{\omega_1^2 - \omega_2^2}{2} \quad \text{(Equation 2.38)}$$

2.3. Oscillation Pattern of Gyroscopes

2.3.1. Response of Gyroscope with Stiffness and Damping Isotropy

When gyros have the same effective mass along the two axes, and when the rotation rate is sufficiently lower than the resonance frequency, the effect of centrifugal force and angular acceleration become negligible. In addition, we assume that the control circuitry cancels damping. The approximated motion equation is shown in Equation 2.39. This coupled equations is difficult to be solved analytically. However, a specific set of solutions for this equation is known to be Equations 2.40-2.43, and one can confirm it by substituting them into Equation 2.39 [89].

$$\begin{bmatrix} M & 0 \\ 0 & M \end{bmatrix}\begin{Bmatrix} \ddot{q}_1 \\ \ddot{q}_2 \end{Bmatrix}+\begin{bmatrix} 0 & -2\gamma\Omega_z \\ 2\gamma\Omega_z & 0 \end{bmatrix}\begin{Bmatrix} \dot{q}_1 \\ \dot{q}_2 \end{Bmatrix}+\begin{bmatrix} \omega^2 & 0 \\ 0 & \omega^2 \end{bmatrix}\begin{Bmatrix} q_1 \\ q_2 \end{Bmatrix}=0$$

(Equation 2.39)

$$q_1 = a(t)\cos(\theta(t))\cos(\omega t+\phi(t)) - q(t)\sin(\theta(t))\sin(\omega t+\phi(t))$$ (Equation 2.40)

$$q_2 = a(t)\sin(\theta(t))\cos(\omega t+\phi(t)) + q(t)\cos(\theta(t))\sin(\omega t+\phi(t))$$ (Equation 2.41)

$$\dot{q}_1 = -\omega a(t)\cos(\theta(t))\sin(\omega t+\phi(t)) - \omega q(t)\sin(\theta(t))\cos(\omega t+\phi(t))$$ (Equation 2.42)

$$\dot{q}_2 = -\omega a(t)\sin(\theta(t))\sin(\omega t+\phi(t)) + \omega q(t)\cos(\theta(t))\cos(\omega t+\phi(t))$$ (Equation 2.43)

Equations 2.40-2.43 are called the canonical pendulum equation. In these equations, a denotes the amplitude of the in-phase motion, q denotes the amplitude of the out-of-phase motion, θ denotes the angle between the main axis of the vibrating motion to the q_1 axis, and ϕ denotes the phase of the motion. The trajectory of the vibrating motion on the principal motion axis, under zero input rotation, is illustrated in Figure 2.6. The motion described by Equations 2.40-2.43 can be more easily understood by numerically plotting using a PDE program like MATLAB.

The motion illustrated in Figure 2.6 is represented with two different amplitudes at the orthogonal axes. To reduce drift and stabilize the scale factor of the vibratory gyroscope, a is set to be constant and q set to be zero. For further analysis, the interrelationships between the changes of the parameters in Equations 2.44-2.47 over time can be described in terms of slowly-varying motional parameters. The details of the mathematical derivation are shown in [89].

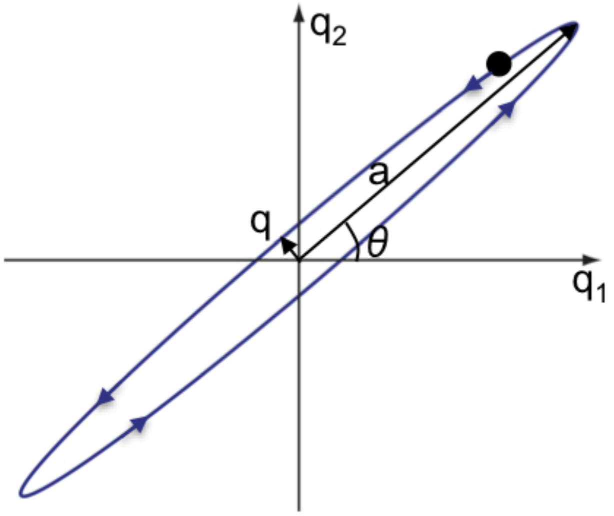

Figure 2.6. Trajectory of free canonical motion, described by Equations 2.37-2.40. Mass is shown in black. *a* is called the in-phase amplitude and *q* is called the quadrature amplitude.

$$\dot{a} = -\left(\frac{2\gamma}{M}\right)\Omega_z q \sin(2\phi)/2 \qquad \text{(Equation 2.44)}$$

$$\dot{q} = -\left(\frac{2\gamma}{M}\right)\Omega_z a \sin(2\phi)/2 \qquad \text{(Equation 2.45)}$$

$$\dot{\theta} = \left(\frac{2\gamma}{M}\right)\Omega_z (q^2 \sin^2\phi - a^2 \sin^2\phi)\big/(a^2 - q^2) \qquad \text{(Equation 2.46)}$$

$$\dot{\phi} = -\left(\frac{2\gamma}{M}\right)\Omega_z aq \cos(2\phi)/(a^2 - q^2) + \omega \qquad \text{(Equation 2.47)}$$

When the rotation rate is much slower than the vibration frequency ($\Omega_z << \omega$), the canonical parameters can be approximated by averaging the change of these parameters over a period. When the quadrature amplitude *q* of these parameters is kept to be zero with the control circuitry, the parameters in Equations 2.48-2.51 become the expressions that are basically the behavior of an ideal rate-integrating gyroscope, where the a precessing rate of a gyro $\dot{\theta}$ is proportional to an applied rotation rate (Ω_z).

$$\dot{a} \approx 0 \quad \text{(Equation 2.48)}$$

$$q = 0 \quad \text{(Equation 2.49)}$$

$$\dot{\theta} \approx -\sin^2 \phi \left(\frac{2\gamma}{M} \right) \Omega_z \quad \text{(Equation 2.50)}$$

$$\approx -\left(\frac{\gamma}{M} \right) \Omega_z \quad \text{(from time averating)}$$

$$\dot{\phi} \approx \omega \quad \text{(Equation 2.51)}$$

2.3.1.1. Response of Ideal Gyro Under Large Input Rate

Under large input rotation, the centrifugal force term cannot be neglected, and reduces the frequency of the oscillation. At the ultimate input rate ($\Omega_{ultimate}$), the centrifugal force becomes equal to the elastic force, and the vibration stops. By relating the motion equation with the centrifugal force, such condition can be found (Equation 2.52). In Equation 2.52, the amplitude of the gyro is sustained and the quadrature amplitude is canceled to zero. Equations 2.53 and 2.54 show the solution to the equation, showing the reduction in the resonance frequency is found by equating ω' to zero in Equation 2.55. Practically, the maximum input rate is typically limited by the dynamic range of the control circuitry.

$$\begin{bmatrix} M & 0 \\ 0 & M \end{bmatrix} \begin{Bmatrix} \ddot{q}_1 \\ \ddot{q}_2 \end{Bmatrix} + \begin{bmatrix} 0 & -2\gamma\Omega_z \\ 2\gamma\Omega_z & 0 \end{bmatrix} \begin{Bmatrix} \dot{q}_1 \\ \dot{q}_2 \end{Bmatrix} + \begin{bmatrix} -\Omega_z^2 & 0 \\ 0 & -M\Omega_z^2 \end{bmatrix} \begin{Bmatrix} q_1 \\ q_2 \end{Bmatrix} + \begin{bmatrix} M\omega^2 & 0 \\ 0 & M\omega^2 \end{bmatrix} \begin{Bmatrix} q_1 \\ q_2 \end{Bmatrix} = \begin{Bmatrix} 0 \\ 0 \end{Bmatrix} \quad \text{(Equation 2.52)}$$

$$q_1 = a\cos\left(\theta_o - \frac{\gamma}{M} \Omega_z t \right) \cos(\omega' t + \phi_o) \quad \text{(Equation 2.53)}$$

$$q_2 = a\sin\left(\theta_o - \frac{\gamma}{M} \Omega_z t \right) \cos(\omega' t + \phi_o) \quad \text{(Equation 2.54)}$$

$$\omega' = \sqrt{\omega^2 - \Omega_z^2\left(1 - \left(\frac{\gamma}{M}\right)^2\right)} \qquad \text{(Equation 2.55)}$$

$$\Omega_{ultimate} = \frac{\omega}{1 - \left(\frac{\gamma}{M}\right)^2} \qquad \text{(Equation 2.56)}$$

The Coriolis mass γ is a function of modal shape. For the lumped mass gyroscope, like the tuning fork gyroscope, γ is 1; for flexural mode gyro (n=2), it ranges from roughly $0.02M$ to $0.6M$. Chapter 3 will describes the procedure for numerically calculating the γ of arbitrary-shaped wineglass-mode gyroscope.

2.3.2. Angular Gain (A_g)

The parameters in Equation 2.13 depend on the resonance mode in which the gyro operates. The two most widely used modes are the translational mode, in the case of the Foucault pendulum, and the wineglass mode, in the case of the Hemispherical Resonator Gyro (HRG) or the cylinder gyro. In the case of the translational mode, the entire mass moves in a single direction. The relationship between the motion along principal mode axes (q_1, q_2) and the Cartesian axis (u_x, u_y), shape functions ϕ, and Coriolis mass γ is shown in Equations 2.57-2.63.

$$u_x = q_1 \qquad \text{(Equation 2.57)}$$

$$u_y = q_2 \qquad \text{(Equation 2.58)}$$

$$u_x = \phi_{x1}q_1 + \phi_{x2}q_2 \qquad \text{(Equation 2.59)}$$

$$u_y = \phi_{y1}q_1 + \phi_{y2}q_2 \qquad \text{(Equation 2.60)}$$

$$\phi_{x1} = 1,\ \phi_{x2} = 0 \qquad \text{(Equation 2.61)}$$

$$\phi_{y1} = 0,\ \phi_{y2} = 1 \qquad \text{(Equation 2.62)}$$

$$\gamma = M \qquad \text{(Equation 2.63)}$$

So far, we have derived the motion of a gyro along the sensor coordinate, so the precession angle θ, found from integrating Equation 2.50 with time, is measured in the sensor coordinate. The angle measured in the sensor coordinate is related to the angle measured in Cartesian coordinate ($\theta_{Cartesian}$) by Equation 2.64:

$$\theta_{Cartesian} = \frac{1}{n}\theta \qquad \text{(Equation 2.64)}$$

In Equation 2.64, n is related with the number of nodes in the oscillation pattern. In the translational mode, like the Foucault pendulum, n is 1. Therefore, the angle $\theta_{Cartesian}$ is equal to θ. In the n=2 flexural mode, the motional axes are separated by 45 degrees in the Cartesian coordinate, so $\theta_{Cartesian}$ becomes a half of θ. Similarly, for n=3 flexural mode, $\theta_{Cartesian}$ becomes a third of θ. The rotation rate (Ω_z), in Equation 2.64, is measured in the Cartesian coordinate. By naming the angle calculated from the integration of Ω_z with time as $\theta_{input\_Cartesian}$, from Equations 2.50 and 2.64, $\theta_{Cartesian}$ and $\theta_{input\_Cartesian}$ are related by:

$$\theta_{Cartesian} = -\frac{\gamma}{nM}\theta_{input\_Cartesian} \qquad \text{(Equation 2.65)}$$

The angular gain (A_g) is defined as the ratio between $\theta_{Cartesian}$ and $\theta_{input\_Cartesian}$ [7], [118]. The A_g is expressed as:

$$A_g = \frac{\gamma}{nM} \qquad \text{(Equation 2.66)}$$

In the translational mode gyro, γ/M is 1, so the A_g of the Foucault pendulum gyro becomes 1. Axisymmetric gyros like the Cylindrical Rate-Integrating Gyroscope

(CING), γ/M ratio is calculated using ANSYS as 0.14~0.7 for an aspect ratio (= height/radius) of 0.05~1. The A_g for the calculated aspect ratio range is therefore 0.007~0.35. For a given geometry, A_g means what portion of the effective mass (M) actually contributes to generate the Coriolis force, so it directly affects the resolution of the gyro. The A_g becomes the scale factor in the rate-integrating gyro (RIG). In Chapter 5, the a number of axisymmetric sensor geometries are compared in terms of mechanical characteristics, including A_g, and microfabricational accuracy and simplicity to find an optimal geometry for the MEMS RIG.

2.3.3. Response of Gyroscope with Mechanical Anisotropy

In an actual vibratory gyroscope, there are several nonideality components that affect stable precession of the pattern. These include anisotropy in the stiffness, anisotropy in damping, and nonlinear stiffness. The effects of stiffness and damping anisotropy are studied.

2.3.3.1. Effect from Anisotropy in Stiffness

Using Equation 2.13, the motion equation with elasticity anisotropy, under zero rotation, can be constructed as [89]:

$$\begin{bmatrix} M & 0 \\ 0 & M \end{bmatrix} \begin{Bmatrix} \ddot{q}_1 \\ \ddot{q}_2 \end{Bmatrix} + M \begin{bmatrix} \omega^2 + \omega\Delta\omega\cos 2\theta_\omega & \omega\Delta\omega\sin 2\theta_\omega \\ \omega\Delta\omega\sin 2\theta_\omega & \omega^2 + \omega\Delta\omega\cos 2\theta_\omega \end{bmatrix} \begin{Bmatrix} q_1 \\ q_2 \end{Bmatrix} = 0 \quad \text{(Equation 2.67)}$$

$$\omega^2 = \frac{\omega_1^2 + \omega_2^2}{2} \quad \text{(Equation 2.68)}$$

$$\omega\Delta\omega = \frac{\omega_1^2 - \omega_2^2}{2} \quad \text{(Equation 2.69)}$$

A set of solution to Equation 2.69 are found to be Equations 2.70-2.75:

$$\dot{a} = \frac{-q}{4\omega}(\omega_1^2 - \omega_2^2)\sin\big(2(\theta - \theta_\omega)\big) \quad \text{(Equation 2.70)}$$

$$\dot{q} = \frac{a}{4\omega}(\omega_1^2 - \omega_2^2)\sin\big(2(\theta - \theta_\omega)\big) \quad \text{(Equation 2.71)}$$

$$\dot{\theta} = -\frac{1}{2\omega}\eta(\omega_1^2 - \omega_2^2)\cos\big(2(\theta - \theta_\omega)\big) \quad \text{(Equation 2.72)}$$

$$\dot{\phi} = \frac{1}{4\omega}\xi(\omega_1^2 - \omega_2^2)\cos\big(2(\theta - \theta_\omega)\big) + \omega \quad \text{(Equation 2.73)}$$

where,

$$\eta = \frac{2aq}{a^2 - q^2} \quad \text{(Equation 2.74)}$$

$$\xi = \frac{a^2 + q^2}{a^2 - q^2} \quad \text{(Equation 2.75)}$$

Equations 2.70-2.75 indicate that all the canonical variables are affected by the elasticity anisotropy. The canonical parameters ($\dot{a}$, $\dot{q}$, $\dot{\theta}$, $\dot{\phi}$) are functions of in-phase amplitude (*a*), quadrature amplitude (*q*), angular position of the oscillation θ, angular separation between the sensor axis and principal stiffness axis θ_ω, and the difference in the square of the resonance frequencies $\omega_1^2 - \omega_2^2$. Among the parameters, we focus on the drift in the output angular position $\dot{\theta}$, because this parameter is the output signal of the sensor. The amount of drift is proportional to $\cos(2(\theta - \theta_\omega))$, so it becomes zero when the oscillation wave pattern is aligned to the principal stiffness axes and becomes the largest when the wave pattern is separated from the stiffness axes by π/4 radians. The $\dot{\theta}$ is proportional to $\omega_1^2 - \omega_2^2$ and *q*. Therefore, to reduce the drift due to stiffness mismatch, the gyro needs to have electrostatic tuning method to match the two frequencies to match them to closest possible distance and cancel the *q* using force feedback control. The tuning and feedback control circuitry can be easily realized in the capacitive gyroscope, so the drift due to stiffness mismatch can be compensated relatively easily. Equation 2.72 also indicates that the drift rate is proportional to nominal frequency change $\Delta\omega$.

$$\frac{\omega_1^2 - \omega_2^2}{\omega} \propto \Delta\omega \qquad \text{(Equation 2.76)}$$

For a constant thermal coefficient of frequency (TC_F), a gyro with a smaller nominal frequency (ω) has smaller frequency drift ($\Delta\omega$) over the same amount of temperature change, so it is advantageous to design a RIG with a small ω.

2.3.3.2. Effect from Anisotropy in Damping

Using Equation 2.13, the motion equation with anisotropy in damping can be expressed as Equation 2.77. In this expression, the rotation rate is also considered to be much slower than the resonance frequency ($\Omega_z << \omega$).

$$\begin{bmatrix} M & 0 \\ 0 & M \end{bmatrix}\begin{Bmatrix} \ddot{q}_1 \\ \ddot{q}_2 \end{Bmatrix} + M\begin{bmatrix} \left(\frac{2}{\tau}\right) + \cos 2\theta_\tau \left(\Delta\frac{1}{\tau}\right) & \sin 2\theta_\tau \left(\Delta\frac{1}{\tau}\right) \\ \sin 2\theta_\tau \left(\Delta\frac{1}{\tau}\right) & \left(\frac{2}{\tau}\right) - \cos 2\theta_\tau \left(\Delta\frac{1}{\tau}\right) \end{bmatrix}\begin{Bmatrix} \dot{q}_1 \\ \dot{q}_2 \end{Bmatrix}$$
$$+ \begin{bmatrix} 0 & -2\gamma\Omega_z \\ 2\gamma\Omega_z & 0 \end{bmatrix}\begin{Bmatrix} \dot{q}_1 \\ \dot{q}_2 \end{Bmatrix} + \begin{bmatrix} \omega^2 & 0 \\ 0 & \omega^2 \end{bmatrix}\begin{Bmatrix} q_1 \\ q_2 \end{Bmatrix} = 0 \qquad \text{(Equation 2.77)}$$

The canonical parameters of the gyroscope considering only the damping anisotropy can be solved as [89]:

$$\dot{a} = \frac{a}{2}\left(\frac{-2}{\tau} - \Delta\frac{1}{\tau}\cos 2(\theta - \theta_\tau)\right) \qquad \text{(Equation 2.78)}$$

$$\dot{q} = \frac{q}{2}\left(\frac{-2}{\tau} - \Delta\frac{1}{\tau}\cos 2(\theta - \theta_\tau)\right) \qquad \text{(Equation 2.79)}$$

$$\dot{\theta} = \frac{1}{2}\xi\Delta\frac{1}{\tau}\sin 2(\theta - \theta_\tau) \qquad \text{(Equation 2.80)}$$

$$\dot{\phi} = -\frac{1}{2}\eta\Delta\frac{1}{\tau}\sin 2(\theta - \theta_\tau) + \omega \qquad \text{(Equation 2.81)}$$

$$\eta = \frac{2aq}{a^2 - q^2}, \qquad \text{(Equation 2.82)}$$

$$\xi = \frac{a^2 + q^2}{a^2 - q^2} \qquad \text{(Equation 2.83)}$$

The parameters ($\dot{a}$, $\dot{q}$, $\dot{\theta}$, $\dot{\phi}$) are functions of in-phase and quadrature amplitudes (*a*, *q*), average of inverse decay time ($1/\tau$) and difference between the inverse of decay time ($\Delta 1/\tau$). The $\dot{\theta}$ decreases with the decrease in *q* and $\Delta 1/\tau$. The *q* can be reduced using quadrature feedback control. However, the parameter $\Delta 1/\tau$ is dependent on the quality factor (*Q*) of the system, and it cannot be reduce easily with tuning or feedback control. Since $\Delta 1/\tau$ parameter is inversely proportional to the inverse of the nominal damping time (τ_o), it is necessary to increase τ_o. The τ_o is proportional to the *Q* and inversely proportional to the resonance frequency ω:

$$\tau_o = \frac{2Q}{\omega} \qquad \text{(Equation 2.84)}$$

The low-frequency gyro is advantageous due to the inverse relationship between the τ_o and ω. Si gyroscopes with a small ω (<5kHz) is advantageous from *Q*, too, because the gyros have a higher *Q* (close to 1 million) due to reduction in thermoelastic damping (TED). The relationship between the ω_o and TED will be discussed further in Chapter 5. To achieve a small $\Delta 1/\tau$, it is ideal to use a degenerate mode in order to have the same damping parameters for both modes. Combining the effect of anisotropy in elasticity and damping, the drift of the vibrating motion is described with the motion parameters as shown in Equations 2.85-2.90 [89].

$$\dot{a} = \frac{-q}{4\omega}(\omega_1^2 - \omega_2^2)\sin 2(\theta - \theta_\omega) + \frac{a}{2}\left(\frac{-2}{\tau} - \Delta\frac{1}{\tau}\cos 2(\theta - \theta_\tau)\right) \qquad \text{(Equation 2.85)}$$

$$\dot{q} = \frac{a}{4\omega}(\omega_1^2 - \omega_2^2)\sin 2(\theta - \theta_\omega) + \frac{b}{2}\left(\frac{-2}{\tau} - \Delta\frac{1}{\tau}\cos 2(\theta - \theta_\tau)\right) \qquad \text{(Equation 2.86)}$$

$$\dot{\theta} = -\frac{\gamma}{M}\Omega - \frac{1}{2\omega}\eta(\omega_1^2 - \omega_2^2)\cos 2(\theta - \theta_\omega) + \frac{1}{2}\xi\Delta\frac{1}{\tau}\sin 2(\theta - \theta_\tau) \qquad \text{(Equation 2.87)}$$

$$\dot{\phi} = \frac{1}{4\omega}\xi(\omega_1^2 - \omega_2^2)\cos 2(\theta - \theta_\omega) - \frac{1}{2}\eta\Delta\frac{1}{\tau}\sin 2(\theta - \theta_\tau) + \omega \qquad \text{(Equation 2.88)}$$

$$\eta = \frac{2aq}{a^2 - q^2} \qquad \text{(Equation 2.89)}$$

$$\xi = \frac{a^2 + q^2}{a^2 - q^2} \qquad \text{(Equation 2.90)}$$

To summarize our findings, to improve the RIG performance, it is necessary to reduce the operating frequency ω_o (to reduce $\omega_1^2 - \omega_2^2$ and $\Delta 1/\tau$), match the frequencies of the two modes ($\omega_1 = \omega_2$), increase Q, and have very close Q for the two modes.

2.3.4. Rate-Gyroscope (RG) Under Stiffness and Damping Anisotropy

In the rate-sensing mode, the motion along the drive axis is kept constant, and the motion along the sense axis is close to zero. The motion of an open-loop mode rate-sensing gyroscope can be derived from the general motion equation (Equation 2.34). In this discussion, we assume that the rotation rate (Ω_z) is small, so we neglect the effects of angular acceleration and centrifugal force. In the open-loop operation, the input force along sense axis (f_2) is zero, the amplitude and velocity along the sense axis (q_2, $\dot{q}_2$) are much smaller than those along the driving axis (q_1, $\dot{q}_1$). For this reason, the cross-coupling forces along the drive axis can be neglected. The motional equations for a general open-loop rate gyroscope are expressed using Equations 2.91-2.92.

$$\ddot{q}_1 + \left[\frac{2}{\tau} + \cos 2\theta_\tau \left(\Delta \frac{2}{\tau}\right)\right]\dot{q}_1 + \left(\omega^2 + \omega\Delta\omega\cos 2\theta_\omega\right)q_1 = \frac{f_1}{M} \qquad \text{(Equation 2.91)}$$

(Drive axis)

$$\ddot{q}_2 + \left[\frac{2}{\tau} - \cos 2\theta_\tau \left(\Delta \frac{1}{\tau}\right)\right]\dot{q}_2 + \frac{2\gamma}{M}\Omega_z\dot{q}_1 + \left(\omega^2 + \omega\Delta\omega\cos 2\theta_\omega\right)q_2$$

$$= -\left(\omega\Delta\omega\sin 2\theta_\omega\right)q_1 - \left(\sin 2\theta_\tau \left(\Delta \frac{1}{\tau}\right)\right)\dot{q}_1 \qquad \text{(Equation 2.92)}$$

(Sense axis)

We find that unlike the rate-integrating mode operation, the motion along the drive axis (Equation 2.91) has effectively zero Coriolis force, so the motion along the drive axis becomes independent from the sense axis motion (Equation 2.92). The motion along the sense axis is affected by the Coriolis force that is generated from motion along drive axis, because q_1 and $\dot{q}_1$ are much larger than q_2 and $\dot{q}_2$. The force that has the same phase with q_1 is called the quadrature force due to 90° phase shift from the Coriolis force. The quadrature force can be reduced by aligning the principal stiffness axes to the sensor axes. This can be relatively easily done using electronic tuning method [7]. The remaining quadrature error can be canceled out using feedback force. The forces that has the same phase with $\dot{q}_1$ include forces from damping anisotropy and the Coriolis force.

When we compare the behavior of the rate-integrating gyro (RIG) and the rate gyro (RG), the influence of stiffness anisotropy can be minimized in both cases easily using electrostatic tuning and quadrature feedback. In the case of the RIG, the anisotropy in damping results in bias drift ($\dot{\theta}$) that depends on the position between the vibrating pattern to the principal damping axis (θ_τ). In the case of the RG, the anisotropy in damping results in a constant rate bias. Both of these bias needs to be canceled using calibration method.

2.4. Performance Parameters of the Vibratory Rate and Rate-Integrating Gyro

The performance of gyros is characterized by many parameters. Among them are short-term accuracy, long-term accuracy, dynamic range, and bandwidth. Short-term accuracy is named the angle random walk (ARW) ($^\circ/\sqrt{hr}$ or $^\circ/hr/\sqrt{Hz}$)[90]. The ARW is caused from Brownian motion of a gyro and white noise from interface circuitry. The spectral density of the Brownian force is [91]:

$$F_{Brownian} = \sqrt{4k_B TR}\ \ (N/\sqrt{Hz}) \qquad \text{(Equation 2.93)}$$

$$k_B = 1.38 \times 10^{-23} m^2 kg s^{-2} K^{-1} \qquad \text{(Boltzmann Constant)} \qquad \text{(Equation 2.94)}$$

$$R \approx \frac{M\omega}{Q} \qquad \text{(Damping constant)} \qquad \text{(Equation 2.95)}$$

The effect of the Brownian noise is calculated by entering the noise term in the right hand side of the 2-DOF motion equation (Equation 2.13). Especially, for a RG where the motions along the two axes are weakly coupled and in the case when the two mode frequencies are matched, the noise-equivalent rotation rate ($\Omega_{Brownian}$) is expressed as:

$$\begin{aligned}\frac{\Omega_{Brownian}}{\sqrt{BW}} &= \frac{\sqrt{4k_B TR}}{2\gamma A_{drive}\omega} \\ &= \frac{1}{nA_g A_{drive}}\sqrt{\frac{k_B T}{M\omega Q_{sense}}}(\text{rad/sec/}\sqrt{\text{Hz}})\end{aligned} \qquad \text{(Equation 2.96)}$$

[A_{drive}: driving amplitude, n: mode number, A_g: angular gain, M: effective mass, ω: resonance frequency, Q_{sense}: effective sense mode quality factor]

Equation 2.96 indicates that $\Omega_{Brownian}$ reduces as Coriolis mass (γ), driving amplitude (A_{drive}), and resonance frequency ω_o increase. The white noise from interface circuitry also contributes to the short-term noise. The noise equivalent rotation rate from the circuitry ($\Omega_{Circuitry}$) can be calculated by dividing its output-referred circuit noise by the scale factor (*SF*) (Equation 2.97):

$$\frac{\Omega_{circuitry}}{\sqrt{BW}} = \frac{\sqrt{v_n^2(output)}}{SF}(\mathrm{rad/sec/\sqrt{Hz}}) \qquad \text{(Equation 2.97)}$$

Typically, a capacitive gyro uses parallel plates along the sense axis to maximize *SF*. For transimpedance amplifier with a feedback resistance of R_{fb}, a DC polarization voltage of V_p across the parallel plates, nominal sense capacitance of C_{sense}, and a parallel plate gap of g_{sense}, *SF* is calculated as:

$$SF = \frac{2V_p R_{fb} n A_g A_{drive} Q_{sense} C_{sense}}{g_{sense}} \qquad \text{(Equation 2.98)}$$

The overall noise-equivalent rotation rate is calculated as:

$$\frac{\Omega_{noise}}{\sqrt{BW}} = \frac{\sqrt{\Omega_{Brownian}^2 + \Omega_{Circuitry}^2}}{\sqrt{BW}}(\mathrm{rad/sec/\sqrt{Hz}}) \qquad \text{(Equation 2.99)}$$

In the RIG, the bias drift is caused by physical parameters such as anisotropy in elasticity and damping and nonlinear stiffness. The 1/f noise from the readout and control circuitry also causes drift. The anisotropy can be calibrated out, but it changes with temperature and pressure. The drift is also caused by environmental vibration, which couples into the 2-DOF dynamics. In the rate-gyroscope (RG), the drift is caused by quadrature error and scale factor change. This can occur from the change in operating pressure or temperature, since they affect the frequency difference between driving and sense mode and *Q*. The maximum scale factor sensitivity occurs when the modes are exactly matched. Therefore, depending on the application, the RG is operated with slight mode mismatch or under feedback.

The full-scale range is the maximum input range where the scale factor is kept within a linearity range. For the rate-integrating gyro (RIG), the scale factor is the angular gain (A_g). For the rate gyro (RG), the scale factor is the rate sensitivity. The factors affecting A_g is the deviation of the motion parameters as the rotation rate (Ω) gets closer to the resonance frequency (ω_o). The bandwidth of the demodulation block from the control circuitry also affects the A_g. For the RG, the scale factor is affected by the nonlinearity in the amplitude or amplitude sensing of the motion along the sense axis. The dynamic range of the rate gyroscope, defined as the ratio between the full-scale range and the noise-equivalent rotation rate, is related with the geometry and the physical parameter of the gyros as [92]:

$$Dynamic\ Range \cong \frac{g_{sense}\omega}{10}\sqrt{\frac{\pi M}{k_B T}} \qquad \text{(Equation 2.100)}$$

[g_{sense}: electrode gap (parallel plate), ω: operating frequency, M: effective mass, k_B: Boltzmann constant, T: temperature]

Equation 2.100 indicates that the dynamic range increases as the capacitance gap and the stiffness of the gyro increase and as the temperature decreases. The bandwidth of the gyroscope is the maximum bandwidth of the input rotation where the output is kept under a certain linearity range. In the RIG, the bandwidth is limited by the bandwidth of the demodulation block of the control circuitry. The gyro dynamics itself is unrelated with the frequency of input rotation. In the RG, the bandwidth is the effective bandwidth of the sense mode dynamics.

2.5. Control of Vibratory Gyroscope

2.5.1. Control Parameters of the Vibratory Gyroscope

From the previous section, it is shown that in order to accurately measure the precessed angle (θ) it is important to cancel the quadrature (q) of the trajectory, sustain the main amplitude (a), and have the right phase relation between the input forces to the dynamics of the gyro. A feedback system can be used to maintain these conditions. Additionally, using pre-calibrated system properties measured at different locations of the samples, a control system can compensate the effects of the stiffness and damping mismatch.

Control variables of RIG are derived in [93] and [94]. In this section, we introduce the control variables in [117]. A positive feedback loop creates the vibration pattern. In the loop at steady state, the overall phase difference is zero and the overall loop gain is 1. Motion parameters such as in-phase mechanical energy (E), quadrature mechanical energy (K), and angle (θ) can be introduced from the motion amplitude, velocity, and phase. They can be individually controlled using separate control loops. The parameters can be expressed in terms of the position (q_1, q_2) and velocity terms ($\dot{q}_1$, $\dot{q}_2$) as [93]:

$$\begin{aligned} E &= a^2 + q^2 \\ &\propto q_1^2 + q_2^2 + \dot{q}_1^2 + \dot{q}_2^2 \text{ (low-pass filtered)} \end{aligned} \quad \text{(Equation 2.101)}$$

$$\begin{aligned} K &= \omega a q \\ &\propto q_1\dot{q}_2 - q_2\dot{q}_1 \text{ (low-pass filtered)} \end{aligned} \quad \text{(Equation 2.102)}$$

$$
\begin{aligned}
\theta &= \frac{1}{2}\tan^{-1}\left(\frac{q_1 q_2 + \dot{q}_1 \dot{q}_2}{q_1^2 + \dot{q}_1^2 - q_2^2 - \dot{q}_2^2}\right) \\
&\approx \tan^{-1}\left(\frac{q_2}{q_1}\right) \text{(when } Q \approx 0\text{)}
\end{aligned}
\qquad \text{(Equation 2.103)}
$$

The feedback forces are applied from both sensor axes and are proportional to the position or velocity of oscillation. The perturbation forces to individually control *E*, *K*, and *θ* can be constructed using feedback loops. These perturbation forces are expressed as [93]:

$$
\begin{bmatrix} M & 0 \\ 0 & M \end{bmatrix}\begin{Bmatrix} \ddot{q}_1 \\ \ddot{q}_2 \end{Bmatrix} + \begin{bmatrix} 0 & -2\gamma\Omega_z \\ -2\gamma\Omega_z & 0 \end{bmatrix}\begin{Bmatrix} \dot{q}_1 \\ \dot{q}_2 \end{Bmatrix} + \begin{bmatrix} -M\Omega_z^2 & 0 \\ 0 & -M\Omega_z^2 \end{bmatrix}\begin{Bmatrix} \dot{q}_1 \\ \dot{q}_2 \end{Bmatrix}
$$

$$
+M\begin{bmatrix} \omega^2 & 0 \\ 0 & \omega^2 \end{bmatrix}\begin{Bmatrix} q_1 \\ q_2 \end{Bmatrix} = \left(C + H + N\right)\begin{Bmatrix} q_1 \\ q_2 \end{Bmatrix} + \left(D + G + \Gamma\right)\begin{Bmatrix} \dot{q}_1 \\ \dot{q}_2 \end{Bmatrix}
$$

(Equation 2.104)

$$
C = \begin{pmatrix} c & 0 \\ 0 & c \end{pmatrix} \qquad \text{(Equation 2.105)}
$$

$$
D = \begin{pmatrix} d & 0 \\ 0 & d \end{pmatrix} \qquad \text{(Equation 2.106)}
$$

$$
\Gamma = \begin{pmatrix} 0 & \psi \\ -\psi & 0 \end{pmatrix} \qquad \text{(Equation 2.107)}
$$

$$
N = \begin{pmatrix} 0 & n \\ -n & 0 \end{pmatrix} \qquad \text{(Equation 2.108)}
$$

In Equations 2.104-2.108, the parameters *c*, *d*, *ψ*, and *n* indicates control parameters, calculated from PI controllers. In Equation 2.104, *C* controls the phase between the input signal to the response; *N* controls *K*; *D* controls *E*; and Γ controls *θ*. In other words, 1) the amplitude of the vibration (*E*) can be controlled by applying signals proportional to the velocity of the respective axis; 2) the quadrature signal of the vibration (K) can be controlled by applying feedback signal that is proportional to the displacement along the opposite axes; 3) the angle of the precession (θ) can be controlled by applying the forces that are proportional to the velocity from the opposite axes; and 4) the phase difference between the reference signal and motion signal can be adjusted by applying forces that are proportional to the displacement of the same axis, which is basically the idea for the electrical tuning.

2.6. Difference Between Control and Design of Rate-Integrating Gyroscope (RIG) and Rate Gyroscope (RG)

2.6.1. Difference in the Control of RIG and RG

In the rate-integrating gyro (RIG), the controller consists of the main phase-control loop to have self-oscillation, amplitude control circuitry to sustain the E, and quadrature control to null the K. The output signal of the RIG is θ. When the frequency difference between the two modes is small, electrical tuning methods can be used. The stiffness anisotropy is compensated mechanically and electrically to nearly zero. Anisotropic damping and stiffness create drift rate that is a sinusoidal function of θ. Thus, by finding out the positions of the principal damping axes and the maximum drift rate at the maximum damping axis, one can compensate the drift due to anisotropic damping, given that the gyro is operated under controlled temperature and pressure level. This compensation method was adopted in the HRG to improve its bias stability sufficient for the inertial grade applications [95].

In the closed-loop mode of RG, there is an additional control for θ. The output signal of this mode is the amplitude of ψ in Equation 2.104, which is an output voltage of a PI controller for θ. In the open-loop mode of the RG, the control circuitry controls the E of one axis (q_1) and mechanical damping limits the amplitude on the second axis (q_2). The mode frequencies are either exactly tuned or matched to a close value. In case the two frequencies are exactly matched, the sense mode displacement (q_2) becomes in-phase with the displacement of mass in the driving axis (q_1). When the two frequencies are intentionally mismatched to achieve wide bandwidth and smaller bias drift, q_2 becomes in-phase with the velocity along the drive axis $\dot{q}_1$. The difference is made from the fact that when the two modes are mismatched, the Coriolis motion does not cause resonance in the motion along the sense axis.

2.6.2. Difference in the Structural Design of RIG and RG

The rate-integrating gyroscope (RIG) and the rate gyroscope (RG) have different physical parameters that affect their performances. The accuracy of the RIG is limited by the drift from stiffness and damping mismatch, so it is critical to closely the stiffness and damping. However, when the principal stiffness axes are aligned closely to the sensor axes, the RG offers good performance in the existence of stiffness and damping anisotropy. The performance of the RG is typically limited by the noise from circuitry (white and 1/f noise), from the body (Brownian motion), quadrature error, and scale-factor change from temperature change.

The difference in the error sources for the RG and RIG leads to different design strategy. First, in the RIG, a symmetrical shape is required. Degenerate-type resonator shapes are generally preferred due to the innate symmetry. The resonators are built with either a polycrystalline material or a material with isotropy along the directions where the shell deforms. In the RIG, the Brownian noise from the mass has less influence than the structural anisotropy. The amplitude of the RIG does not influence the scale factor of the sensor, so the amplitude of the sensor can be kept at a relatively small level.

On the other hand, for the RG, a symmetrical structure shape is not needed. There is no restriction in the crystallography of materials to create a RG. Many designs adopt lumped-mass structures, like a tuning-fork gyroscope, because these structures have much larger effective mass and larger gain factor and it is much easier to control their gyro frequencies to a desired value than in a degenerate-mode gyroscope. Folded springs are used to reduce nonlinear stiffening in order to have large oscillation amplitudes. Comb-drive electrodes are used to induce large actuation amplitude with low nonlinearity. Comb-drive electrodes are not suitable for the RIG, because they create off-axis attracting forces when the oscillation motion deviates from the direction of the electrodes (Figure 2.7). Parallel electrodes do not produce such off-axis force, so they are adopted in the RIG (Figure 2.8).

A number of advanced design techniques are available for the RG. Mode-decoupling designs are proposed for reducing quadrature error caused by the microfabrication process [21, 55, 57-60, 65, 66, 69, 80]. The decoupled gyro typically has two sets of springs with strong directional compliancy, i.e. the drive-mode spring is compliant along only the driving axis and the sense-mode spring is compliant along only the sensing axis. A decoupled gyro is typically constructed by having a gyro mass connected a single set of directional springs. The springs are connected to a frame with strong rigidity in all directions. The frame is connected to another set of directional springs. Finally, the directional springs are connected to an anchor. With multiple masses (main mass, frame) and multiple springs, the structure of the decoupled gyroscope is asymmetric with respect to the principal motion axes. In addition, the vibration sensitivity of a tuning-fork gyroscope is reduced by using balanced modes for driving and sensing modes, where the components of motion from environmental vibration can be differentially canceled. In order to create a balanced-mode gyroscope, multiple sets of masses and springs are used, and the shapes of these springs are often not the same for the two axes. Because of this, although many balanced mode gyros can become a good RG, they may not be suitable as RIG.

2.7. Summary

In this chapter, the principle of vibratory rate gyro (RG) and rate-integrating gyroscopes (RIG) are explained. The rate-integrating gyro measures angular position (θ), and the advantage of the RIG include large full-scale range and wide bandwidth, both of which are fraction of its operating frequency (ω). The RIG also has a stable scale factor, angular gain (A_g), which is determined sorely from the geometry of the gyro. The RIG has these characteristics because of equal coupling of Coriolis force to both motional axes. When a gyro has identical stiffness and damping along both motional axes, the motional responses of the two motional axes under the Coriolis force become identical, resulting in zero drift. However, there is always a certain amount of mismatch in stiffness and damping, and the mismatch in these parameters cause drift in vibrational pattern ($\dot{\theta}$). The mismatch in the stiffness factors can be suppressed relatively easily using electrical tuning and quadrature-control algorithm. The drift due to the mismatch in damping coefficient is difficult to suppress, and it needs to be compensated using calibrated drift data over two-dimensional space. The bias drift rate is also inversely proportional to the nominal decay time (τ_o), so it is also important to design a device with a large Q and a small operating frequency (<5kHz). Due to the requirement of isotropy in stiffness and damping, the geometries for the RIG are typically limited to those with degenerate modes. Axisymmetric geometries are preferred due to innate matching in stiffness and damping.

The RG is a subset of RIG. The output signal of the RG is rotational rate ($\dot{\theta}$). The advantage of the RG is simpler control and high accuracy in rate measurement. The principle of the RG is unequal coupling of Coriolis force in the two motional axes. In this mode, the vibrational amplitude along only the driving axis is kept large, and the sense mode motion is influenced by the Coriolis force. However, since the vibrational amplitude along the sense axis is much smaller than the amplitude in the driving axis, so

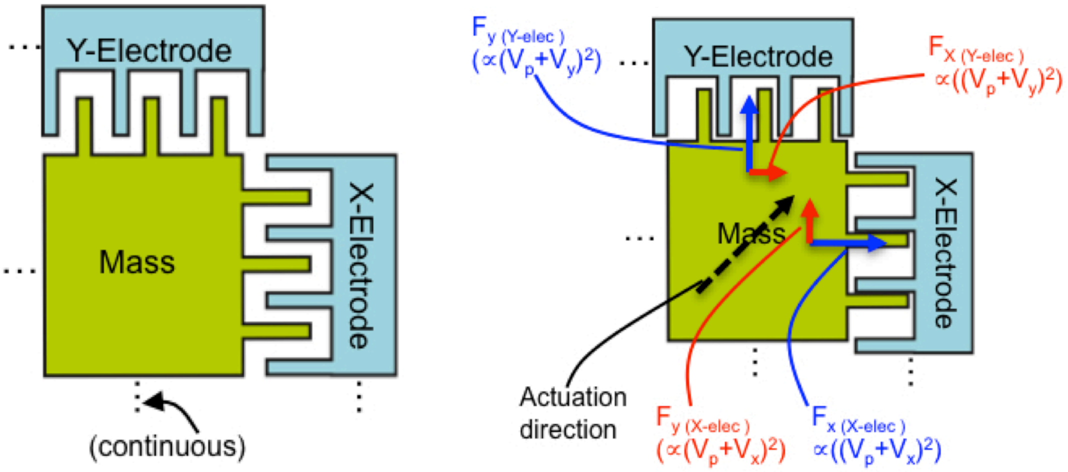

(a) Initial position of the mass with respect to the x and y comb drive electrodes.

(b) Parallel (blue) and perpendicular (red) force components from x- and y-axis comb-drive electrodes and resultant actuation direction (black)

Figure 2.7. Comb drive actuation of mass: (a) Initial state of a rectangular mass with x- and y- comb-drive electrodes and (b) force diagram when the mass (at GND) is actuated from x-axis electrode (at $V_x + V_p$) and y-axis electrode (at $V_y + V_p$). The actuation direction of the mass deviates from the intended direction due to the off-axis force components (in red) from both electrodes.

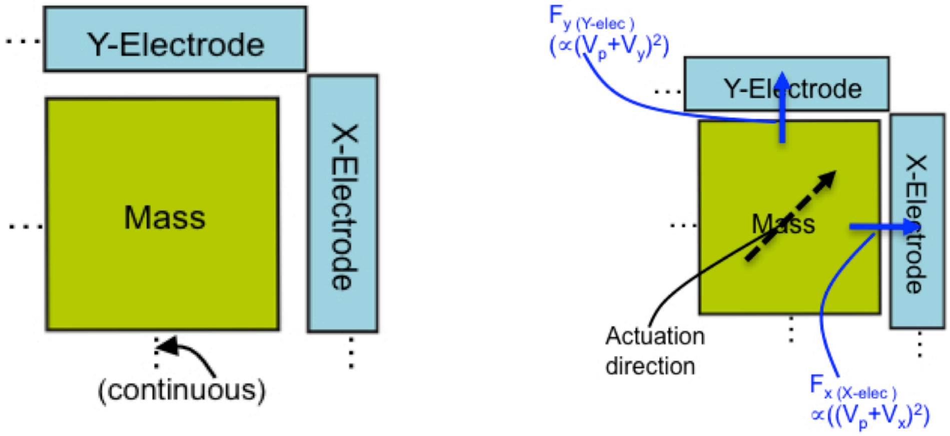

(a) Initial position of the mass with respect to the x- and y- parallel drive electrodes

(b) Parallel (blue) force components from x- and y- parallel electrode and resultant actuation direction

Figure 2.8. Parallel-plate actuation of mass: (a) Initial state of a rectangular mass with x- and y- parallel plate electrodes and (b) force diagram when the mass (at GND) is actuated from x- electrode (at $V_x + V_p$) and y- electrode (at $V_y + V_p$). The direction of vibration is controlled more precisely because there are no off-axis forces.

negligible amount of Coriolis force is generated along the driving axis. The RG does not require isotropic stiffness or damping coefficients along the driving and sense mode axes. In fact, the resonance frequencies of the two modes are typically slightly mismatched to achieve wider bandwidth and prevent large change in its scale factor over temperature or pressure change. In addition, the Q of the sense mode is typically kept lower than the Q of the drive mode to increase the bandwidth. The geometry of the sensor and the vibrational mode shapes of the RG are much less restricted than the RIG, since the accuracy of RG is not limited by the anisotropy in stiffness or damping. The rest of the comparison between the RG and the RIG are included in Tables 2.1-2.3.

In later chapters, the design, fabrication, and testing of a RG, Balanced Oscillating Gyroscope (BOG) and a RIG, Cylindrical Rate-Integrating Gyroscope (CING), will be described. Especially, for the CING, due to the strict requirement for stiffness and damping isotropy, we focused on developing a gyro with an entirely axisymmetric geometry, self-alignment of the anchor and the resonator body, low operating frequency (~3kHz), and large Q (~100,000).

Table 2.1. Comparison of mechanical properties and designs of the vibratory rate gyroscope (RG) and rate-integrating gyroscope (RIG) from viewpoint of sensor property and sources of error

A. Sensor Property and Sources of Error		
Category	**Rate Gyroscope (RG)**	**Rate-Integrating Gyroscope (RIG)**
1. Sensor output	Amplitude along sense axis (q_2) (open loop), counterbalancing force amplitude (ψ) (closed loop).	Rotation angle (θ).
2. Scale factor	$\propto \frac{V_p R_{fb} n A_g A_{drive} Q_{sense} C_{sense}}{g_{sense}}$ (from Equation 2.97).	Angular gain (A_g).
3. Bandwidth	$\propto \frac{\omega}{Q_{sense}}$.	Bandwidth of low-pass filter of demodulator (fraction of ω).
4. Dynamic range	$\approx \frac{g_{sense}\omega}{10}\sqrt{\frac{\pi M_{eff}}{k_B T}}$ (from Equation 2.99).	Bandwidth of low pass filter of demodulator (fraction of ω) divided by minimum angular resolution.
5. Physical sources limiting the accuracy	a. Short term: Brownian noise. b. Long term accuracy (>1sec) - Quadrature error. - Electrical feedthrough. - 1/f noise. - Scale factor change due to pressure or temperature change. - Shock and vibration.	Stiffness and damping mismatch, Brownian motion, circuit noise, and control error.

Table 2.2. Comparison between mechanical properties and designs of the vibratory rate gyroscope (RG) and rate-integrating gyroscope (RIG) from viewpoint of structural requirements

B. Structural Requirements		
Category	**Rate Gyroscope (RG)**	**Rate-integrating gyroscope (RIG)**
1. Effective mass (*M*)	a. Large *M* needed for better resolution. b. *M* for two modes do not need to be the same.	a. *M* for two modes need to be identical. b. Large *M* reduces Brownian noise, but it is not the performance-limiting factor.
2. Frequency (ω)	a. Larger ω helps increasing bandwidth and shock resistivity, but typically leads to lower SNR (due to limitation in the transduction area). b. Lower ω simplifies fabrication process and leads to larger SNR, and increases electrical tuning range, but more fragile and more sensitive to environmental vibration. c. Frequency mismatch ($\Delta\omega$) decreases SNR but increases BW.	a. Lower ω improves τ and leads to lower drift due to anisotropic damping, but more fragile and sensitive to vibration. b. Larger ω improves sensor bandwidth and full-scale range. c. Exact mode matching is needed.
3. Quality factor (*Q*)	a. Large *Q* improves SNR but lowers the BW and increases drift under pressure or temperature change. b. Sense-mode *Q* determines sensor's BW.	a. Large *Q* improves bias stability. b. *Q* does not affect bandwidth or full-scale range.

Table 2.3. Comparison between mechanical properties and designs of the vibratory rate gyroscope (RG) and rate-integrating gyroscope (RIG) from viewpoint of sensor design and control

C. Sensor Design and Control		
Category	**Rate Gyroscope (RG)**	**Rate-integrating gyroscope (RIG)**
1. Operating mode shapes	a. Modes with low vibration sensitivity (balanced mode), low quadrature error (decoupled design), and large Q (low anchor loss) are required. b. Degenerate modes are not required.	a. Mode with low vibration (balanced mode) and large Q (low anchor loss). b. Degenerate modes are required.
2. Mass	Multiple masses are typically used for mode decoupling and creating balanced modes.	Axisymmetric geometry is typically used. Multiple masses can be used for balanced mode shapes and lower the anchor loss.
3. Spring design	a. Directional springs are used in decoupled gyros. b. Spring designs for drive and sense modes can be different. c. Springs with large deflection, small nonlinearity, and low temperature sensitivity are required. d. Coupling springs are used to separate parasitic modes from operating modes.	a. Spring shapes needs to be symmetric. b. Springs with large deflection amplitude may not be as important as in the RG. c. Coupling springs are equally important as in the RG.
4. Anchor design	Needs to be designed for low anchor loss and low temperature sensitivity.	a. Anchor positions need to be symmetric. b. Needs to be designed for low anchor loss and low temperature sensitivity.
5. Electrode design	Comb drive electrodes are typically used along driving axis, and parallel plate electrodes are typically used along sensing axis.	Parallel plate electrodes are used along both axes.
6. Basic control blocks	Main amplitude-control loop (E), quadrature-controlling loop (K), angular position controlling loop (θ).	Main amplitude-control loop (E), quadrature-controlling loop (Q).

CHAPTER 3.

DERIVATION OF PHYSICAL PARAMETERS OF 3-DIMENSIONAL WINEGLASS-MODE GYROSCOPE

In Chapter 2, we derived a general motional equation for a vibratory gyroscope. The physical parameters of a gyro include effective mass (M), angular gain (A_g), and centrifugal mass (α, β, μ). For a tuning fork gyroscope, it is straightforward to calculate these parameters, because there is a clear distinction between the spring and mass within the geometry and motional patterns (translation or torsion) are simple. In a continuous-shaped gyroscope, like the hemispherical resonator gyroscope (HRG), it is difficult to calculate these parameters, because the resonator shell serves as a mass and spring at the same time and the flexural motion is more complex than translational or torsional motions. Their physical parameters need to be solved numerically. In this chapter, the physical parameters of three-dimensional axisymmetric gyroscopes are derived in terms of their modal shape functions. The procedures for numerically calculating them using ANSYS will be discussed.

3.1. Lagrangian Motional Equation

The Lagrangian motional equation of a gyroscope is constructed using the generalized displacements of the two modes (q_i), kinetic energy T_E, potential energy V_E, damping energy D_E, and the externally applied force (F_i) as [96]:

$$\frac{d}{dt}\left(\frac{\partial(T_E - V_E)}{\partial \dot{q}_1}\right) - \frac{\partial(T_E - V_E)}{\partial q_1} + \frac{\partial D_E}{\partial q_1} = F_1 \quad \text{(Mode 1)} \qquad \text{(Equation 3.1)}$$

$$\frac{d}{dt}\left(\frac{\partial(T_E - V_E)}{\partial \dot{q}_2}\right) - \frac{\partial(T_E - V_E)}{\partial q_2} + \frac{\partial D_E}{\partial q_2} = F_2 \quad \text{(Mode 2)} \qquad \text{(Equation 3.2)}$$

3.1.1. Kinetic Energy (T_E)

For a continuous geometry, T_E is an integral of the kinetic energies of finite elements over the entire geometry, and it is given as:

$$T_E = \frac{1}{2}\int_V \rho \left|\overrightarrow{v(p)}\right|^2 dV \qquad \text{(Equation 3.3)}$$

In Equation 3.3, ρ denotes density, $\overrightarrow{v(p)}$ denotes the velocity vector of element p in the inertial coordinate system. We consider a gyro located on a rotating coordinate, located at a position vector of $\vec{r_a}$ from the origin (Figure 3.1). The coordinate rotates with an angular velocity vector $\vec{\Omega}$ and translates with a velocity vector $\vec{v_o}$. When a finite element p, located at $\vec{x_p}$ from the origin of the sensor coordinate, is translating with a displacement vector $\overrightarrow{u(p)}$, the velocity vector in the inertial coordinate $\vec{v}$ is expressed as [97]:

$$\vec{v} = \vec{v_o} + \overrightarrow{\dot{u}(p)} + \vec{\Omega} \times (\vec{r_a} + \vec{x_p} + \overrightarrow{u(p)}) \qquad \text{(Equation 3.4)}$$

In the Cartesian coordinate, $\vec{v_o}$ is expressed as (v_{xo}, v_{yo}, v_{zo}), $\overrightarrow{\dot{u}(p)}$ is expressed as ($\dot{u}_x$, $\dot{u}_y$, $\dot{u}_z$), $\vec{\Omega}$ is expressed as (Ω_x, Ω_y, Ω_z), $\vec{r_a}$ is expressed as (x_a, y_a, z_a), $\vec{x_p}$ is expressed as (x_p, y_p, z_p), and $\overrightarrow{u(p)}$ is expressed as (u_x, u_y, u_z). The $\vec{v}$ becomes:

$$\begin{bmatrix} v_x \\ v_y \\ v_z \end{bmatrix} = \begin{bmatrix} v_{xo} + \dot{u}_x + \Omega_y(z_a + z_p + u_z) - \Omega_z(y_a + y_p + u_y) \\ v_{yo} + \dot{u}_y - \Omega_x(z_a + z_p + u_z) + \Omega_z(x_a + x_p + u_x) \\ v_{zo} + \dot{u}_z + \Omega_x(y_a + y_p + u_y) - \Omega_y(x_a + x_p + u_x) \end{bmatrix} \qquad \text{(Equation 3.5)}$$

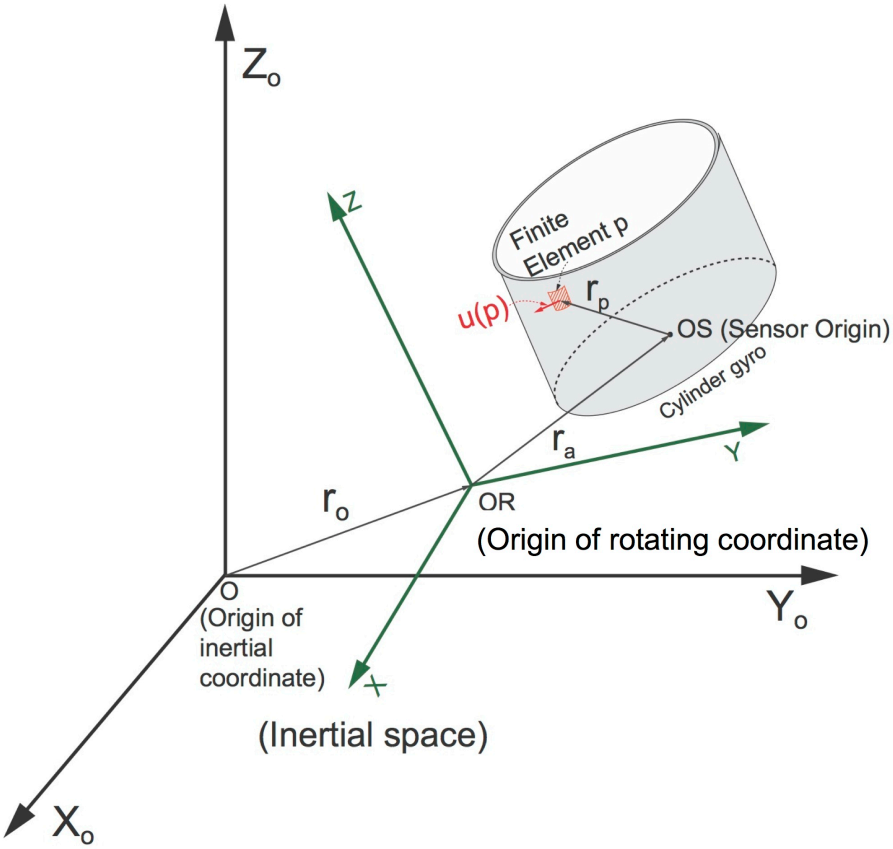

Figure 3.1. Finite element of a cylindrical gyro, located at $\overrightarrow{r_p}$ from sensor origin and has displacement vector $\overrightarrow{u(p)}$. The gyro is located at $\overrightarrow{r_a}$ from the origin of rotating coordinate, and rotating coordinate is located at $\overrightarrow{r_o}$ from the inertial coordinate origin.

The motion of the gyro can be expressed as a sum of two normal modes (Figure 3.2), so we can express motion of the finite element using the modal parameters. For an axisymmetric gyro, the two modes are flexural modes, also known as wineglass modes. The amplitudes of these modes are expressed in terms of modal coordinates (q_1, q_2). In the wineglass mode, the finite element at different location has different oscillation amplitudes, and it is most useful to define q_1 and q_2 as the maximum displacements from the two modes. The amplitudes at the rest of the locations are normalized with q_1 and q_2, and they are defined as shape functions [($\phi_{x1}, \phi_{y1}, \phi_{z1}$) for mode 1, and ($\phi_{x2}, \phi_{y2}, \phi_{z2}$) for mode 2]. The displacement of a finite element p for mode 1 and mode 2, ($u_{x1}(p)$, $u_{y1}(p)$, $u_{z1}(p)$) and ($u_{x2}(p)$, $u_{y2}(p)$, $u_{z2}(p)$), respectively, are expressed as:

$$\begin{bmatrix} u_{x1}(p) \\ u_{y1}(p) \\ u_{z1}(p) \end{bmatrix} = \begin{bmatrix} \phi_{x1}(p) \\ \phi_{y1}(p) \\ \phi_{z1}(p) \end{bmatrix} q_1 \qquad \text{(Mode 1)} \qquad \text{(Equation 3.6)}$$

$$\begin{bmatrix} u_{x2}(p) \\ u_{y2}(p) \\ u_{z2}(p) \end{bmatrix} = \begin{bmatrix} \phi_{x2}(p) \\ \phi_{y2}(p) \\ \phi_{z2}(p) \end{bmatrix} q_2 \qquad \text{(Mode 2)} \qquad \text{(Equation 3.7)}$$

The displacement vector $\overrightarrow{u(p)}$ is expressed as a superposition of displacements from the two modes.

$$\begin{bmatrix} u_x(p) \\ u_y(p) \\ u_z(p) \end{bmatrix} = \begin{bmatrix} \phi_{x1}(p) \\ \phi_{y1}(p) \\ \phi_{z1}(p) \end{bmatrix} q_1 + \begin{bmatrix} \phi_{x2}(p) \\ \phi_{y2}(p) \\ \phi_{z2}(p) \end{bmatrix} q_2 \qquad \text{(Equation 3.8)}$$

Equation 3.8 can be combined with Equation 3.5 to find the square of the velocity amplitude of the finite element p:

$$\begin{aligned} |v(p)|^2 &= v_x^2(p) + v_y^2(p) + v_z^2(p) \\ &= [v_{xo} + \dot{u}_x + \Omega_y(z_a + z_p + u_z) - \Omega_z(y_a + y_p + u_y)]^2 \\ &\quad + [v_{yo} + \dot{u}_y - \Omega_x(z_a + z_p + u_z) + \Omega_z(x_a + x_p + u_x)]^2 \\ &\quad + [v_{zo} + \dot{u}_z + \Omega_x(y_a + y_p + u_y) - \Omega_y(x_a + x_p + u_x)]^2 \end{aligned} \qquad \text{(Equation 3.9)}$$

,where

$$\begin{aligned} u_x(p) &= \phi_{x1}(p) q_1 + \phi_{x2}(p) q_2 \\ u_y(p) &= \phi_{y1}(p) q_1 + \phi_{y2}(p) q_2 \\ u_z(p) &= \phi_{z1}(p) q_1 + \phi_{z2}(p) q_2 \end{aligned}$$

The expanded form of the Equation 3.9 contains many terms, and it is not particularly physically meaningful. However, after we integrate $\left|\overrightarrow{v(p)}\right|^2$ over the entire geometry to calculate the $|v|^2$ (Equation 3.10), several terms will be canceled out, and the equations can become much simpler.

$$\left|\vec{v}\right|^2 = \int_V \left|\overrightarrow{v(p)}\right|^2 dV \qquad \text{(Equation 3.10)}$$

The expression for $|v|^2$ can be simplified first by canceling out the terms that do not contribute to the generation of inertial forces. These terms will become zero after differentiation during the derivation of the motional equations (Equations 3.1-3.2). The equations can be further simplified due to the symmetry in the modal shape and the orthogonality of the modes.

The displacement pattern of the wineglass mode is symmetric with respect to the axis of symmetry. The oscillation pattern along the azimuthal direction is expressed as sinusoidal wave function. From these characteristics, we can derive several mathematical expressions for the displacement of the finite elements. These expression become very useful in simplifying the $\left|\overrightarrow{v(p)}\right|^2$. Figure 3.2 shows a hemispherical resonator gyroscope (HRG) in the spherical coordinate. The HRG oscillates in the $n=2$ wineglass mode. The z-axis of the Cartesian coordinate is aligned to the symmetry axis of the gyro. The antinodes of this mode in the mode 1 are located at azimuthal positions (φ) of 0, $\pi/2$, π, and $3\pi/2$ radians. In the spherical coordinate, the radial (ΔU_1), tangential-to-azimuth (ΔV_1), and tangential-to-altitude (ΔW_1) displacements for the wineglass mode are sinusoidal functions of 2φ. The subscript 1 denotes that the displacement is from mode 1. The azimuthal position φ with the maximum $|\Delta U_1|$ always has the minimum $|\Delta V_1|$.

Therefore, $|\Delta U_1|$ and $|\Delta V_1|$ have a quadrature relationship. The phase of ΔW_1 matches the phase of ΔU_1 to conserve the overall volume. A general expression for the displacements ΔU_1, ΔV_1, and ΔW_1 of an element p in the spherical coordinate (r, φ, θ), oscillating in the nth-order wineglass mode, can be expressed as [98]:

$$\Delta U_1(r,\varphi,\theta) = f(r,\theta) q_1 \cos(n\varphi) \quad \text{(Equation 3.11)}$$

$$\Delta V_1(r,\varphi,\theta) = -g(r,\theta) q_1 \sin(n\varphi) \quad \text{(Equation 3.12)}$$

$$\Delta W_1(r,\varphi,\theta) = h(r,\theta) q_1 \cos(n\varphi) \quad \text{(Equation 3.13)}$$

In Equations 3.11-3.13, $f(r,\theta)$, $g(r,\theta)$, and $h(r,\theta)$ are shape functions in terms of radial and altitudinal coordinates. The mode has antinodes at φ of $i\pi/n$ (i: integer from 1 to $2n$) radians. The displacements of element p in mode 2 are:

$$\begin{aligned}\Delta U_2(r,\varphi,\theta) &= f(r,\theta) q_2 \cos\big(n(\varphi - \pi/2n)\big) \\ &= f(r,\theta) q_2 \sin\big(n\varphi\big)\end{aligned} \quad \text{(Equation 3.14)}$$

$$\begin{aligned}\Delta V_2(r,\varphi,\theta) &= -g(r,\theta) q_2 \sin\big(n(\varphi - \pi/2n)\big) \\ &= g(r,\theta) q_2 \cos\big(n\varphi\big)\end{aligned} \quad \text{(Equation 3.15)}$$

$$\begin{aligned}\Delta W_2(r,\varphi,\theta) &= h(r,\theta) q_2 \cos\big(n(\varphi - \pi/2n)\big) \\ &= h(r,\theta) q_2 \sin\big(n\varphi\big)\end{aligned} \quad \text{(Equation 3.16)}$$

The mode has antinodes at φ of $\pi(2i-1)/2n$ (i: integer from 1 to $2n$) radians. The displacements in the spherical coordinate are converted into the Cartesian coordinate as:

$$\Delta u_{xi}(r,\varphi,\theta) = \Delta U_i \cos\varphi \sin\theta - \Delta V_i \sin\varphi + \Delta W_i \cos\varphi \cos\theta \quad \text{(Equation 3.17)}$$

$$\Delta u_{yi}(r,\varphi,\theta) = \Delta U_i \sin\varphi \sin\theta + \Delta V_i \cos\varphi + \Delta W_i \sin\varphi \cos\theta \quad \text{(Equation 3.18)}$$

$$\Delta u_{zi}(r,\varphi,\theta) = \Delta U_i \cos\theta - \Delta W_i \sin\theta \quad \text{(Equation 3.19)}$$

The shape functions in the wineglass modes 1 and 2 are translated as:

$$\begin{aligned}\phi_{x1}(r,\varphi,z) &= f(r,\theta)\cos(\varphi)\cos(2\varphi)\sin\theta - g(r,\theta)\sin(\varphi)\sin(2\varphi)\\ &\quad +h(r,\theta)\cos(\varphi)\cos(2\varphi)\cos\theta\end{aligned} \qquad \text{(Equation 3.20)}$$

$$\begin{aligned}\phi_{y1}(r,\varphi,\theta) &= f(r,\theta)\sin(\varphi)\cos(2\varphi)\sin\theta + g(r,\theta)\cos(\varphi)\sin(2\varphi)\\ &\quad +h(r,\theta)\sin(\varphi)\cos(2\varphi)\cos\theta\end{aligned} \qquad \text{(Equation 3.21)}$$

$$\phi_{z1}(r,\varphi,\theta) = f(r,\theta)\cos(2\varphi)\cos\theta - h(r,\theta)\cos(2\varphi)\sin\theta \qquad \text{(Equation 3.22)}$$

$$\begin{aligned}\phi_{x2}(r,\varphi,z) &= f(r,\theta)\cos(\varphi)\sin(2\varphi)\sin\theta + g(r,\theta)\sin(\varphi)\cos(2\varphi)\\ &\quad +h(r,\theta)\cos(\varphi)\sin(2\varphi)\cos\theta\end{aligned} \qquad \text{(Equation 3.23)}$$

$$\begin{aligned}\phi_{y2}(r,\varphi,\theta) &= f(r,\theta)\sin(\varphi)\sin(2\varphi)\sin\theta - g(r,\theta)\cos(\varphi)\cos(2\varphi)\\ &\quad +h(r,\theta)\sin(\varphi)\sin(2\varphi)\cos\theta\end{aligned} \qquad \text{(Equation 3.24)}$$

$$\phi_{z2}(r,\varphi,\theta) = f(r,\theta)\sin(2\varphi)\cos\theta - h(r,\theta)\sin(2\varphi)\sin\theta \qquad \text{(Equation 3.25)}$$

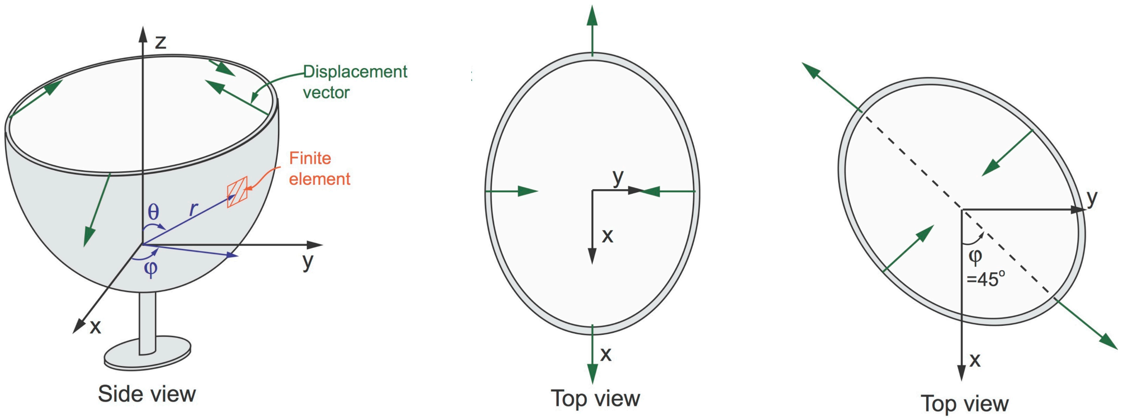

(a) Finite element of a hemispherical gyro in spherical coordinate (in orange)

(b) Oscillation pattern of the n=2 wineglass mode 1

(c) Oscillation pattern of the n=2 wineglass mode 2

Figure 3.2. Hemispherical resonator gyro (HRG) in n=2 the wineglass mode. A finite element p is located at location vector (r,φ,θ) in the spherical coordinate. The wineglass mode patterns are aligned at azimuthal positions (φ) of 0, π/2, π, and 3π/2 radians in mode 1 and π/4, 3π/4, 5π/4, and 7π/4 radians in mode 2.

Using Equations 3.20-3.25, the following four properties are found for the wineglass mode. The first property is that the sum of displacement for the overall geometry becomes zero. This property can be expressed using Equations 3.26-3.31.

- Property 3.1

$$\int_V \phi_{x1}(p)dV = 0 \qquad \text{(Equation 3.26)}$$

$$\int_V \phi_{x2}(p)dV = 0 \qquad \text{(Equation 3.27)}$$

$$\int_V \phi_{y1}(p)dV = 0 \qquad \text{(Equation 3.28)}$$

$$\int_V \phi_{y2}(p)dV = 0 \qquad \text{(Equation 3.29)}$$

$$\int_V \phi_{z1}(p)dV = 0 \qquad \text{(Equation 3.30)}$$

$$\int_V \phi_{z2}(p)dV = 0 \qquad \text{(Equation 3.31)}$$

Property 3.1 is expressed using general displacement parameters (u_{x1}, u_{y1}, u_{z1}, u_{x2}, u_{y2}, u_{z2}) as:

- Property 3.1-1.

$$\int_V u_{x1}(p)dV = 0 \qquad \text{(Equation 3.32)}$$

$$\int_V u_{x2}(p)dV = 0 \qquad \text{(Equation 3.33)}$$

$$\int_V u_{y1}(p)dV = 0 \qquad \text{(Equation 3.34)}$$

$$\int_V u_{y2}(p)dV = 0 \qquad \text{(Equation 3.35)}$$

$$\int_V u_{z1}(p)dV = 0 \qquad \text{(Equation 3.36)}$$

$$\int_V u_{z2}(p)dV = 0 \qquad \text{(Equation 3.37)}$$

The second property is that the integration of multiplication of the shape functions on the same axis in two wineglass modes becomes zero. This property can be expressed as:

- Property 3.2

$$\int_v [\phi_{x1}(p)\phi_{x2}(p)]dV = 0 \qquad \text{(Equation 3.38)}$$

$$\int_v [\phi_{y1}(p)\phi_{y2}(p)]dV = 0 \qquad \text{(Equation 3.39)}$$

$$\int_v [\phi_{z1}(p)\phi_{z2}(p)]dV = 0 \qquad \text{(Equation 3.40)}$$

The third property is that the integration of the sum of the cross products of the shape functions on x and y axes in the two wineglass modes becomes zero.

- Property 3.3

$$\int_v \left(\phi_{x1}(p)\phi_{y2}(p) + \phi_{x2}(p)\phi_{y1}(p)\right)dV = 0 \qquad \text{(Equation 3.41)}$$

The fourth property is that the integration of the product of the shape functions for two different axes in a single mode becomes zero.

- Property 3.4

$$\int_V \left[\phi_{x1}(p)\phi_{y1}(p)\right]dV = 0 \qquad \text{(Equation 3.42)}$$

$$\int_V \left[\phi_{x2}(p)\phi_{y2}(p)\right]dV = 0 \qquad \text{(Equation 3.43)}$$

$$\int_V \left[\phi_{x1}(p)\phi_{z1}(p)\right]dV = 0 \qquad \text{(Equation 3.44)}$$

$$\int_V \left[\phi_{x2}(p)\phi_{z2}(p)\right]dV = 0 \qquad \text{(Equation 3.45)}$$

$$\int_V \left[\phi_{y1}(p)\phi_{z1}(p)\right]dV = 0 \qquad \text{(Equation 3.46)}$$

$$\int_V \left[\phi_{y2}(p)\phi_{z2}(p)\right]dV = 0 \qquad \text{(Equation 3.47)}$$

Additionally, the fifth property of the mode is defined using the orthogonality principle of motion in the resonance mode. The orthogonality principle states that the product of the eigenvectors of finite elements in two different modes is integrated to become zero [96]. This property can be expressed as:

- Property 3.5

$$\int_V \left(\phi_{x1}(p)\phi_{x2}(p)+\phi_{y2}(p)\phi_{y2}(p)+\phi_{z2}(p)\phi_{z2}(p)\right)=0 \qquad \text{(Equation 3.48)}$$

The difference between Property 3.5 from Properties 3.1-3.4 is that is that Property 3.5 is valid regardless of the symmetry in the modal shapes, whereas Properties 3.1-3.4 are valid only if the mode shape is symmetric. Now, Equation 3.9 is simplified using the abovementioned properties. First, by canceling out the parameters that do not contribute to inertial force and by applying Property 3.1-1, $|v|^2$ can be simplified as:

$$\begin{aligned}
&|v|^2 \\
&= \int_V \left(\dot{u}_x^2+\dot{u}_y^2+\dot{u}_z^2\right)dV && \text{(Group 1)} \\
&\quad + \int_V (\Omega_x(-2\dot{u}_y u_z + 2u_y\dot{u}_z) + \Omega_y(2\dot{u}_x u_z - 2u_x\dot{u}_z) + \Omega_z(-2\dot{u}_x u_y + 2u_x\dot{u}_y))dV && \text{(Group 2)} \\
&\quad + \int_V (\Omega_x^2(u_y^2+u_z^2) + \Omega_y^2(u_x^2+u_z^2) + \Omega_z^2(u_x^2+u_y^2))dV && \text{(Group 3)} \\
&\quad + \int_V (-2\Omega_y\Omega_z u_y u_z - 2\Omega_x\Omega_z u_x u_z - 2\Omega_x\Omega_y u_x u_y)dV && \text{(Group 4)}
\end{aligned}$$

(Equation 3.49)

In Equation 3.49, Groups 1-4 in can be expressed in terms of modal parameters, and they will be further simplified using abovementioned properties.

- Group 1 (simplified using Property 3.5):

$$\int_V \left(\dot{u}_x^2+\dot{u}_y^2+\dot{u}_z^2\right)dV$$
$$=\int_V \left((\phi_{x1}^2+\phi_{y1}^2+\phi_{z1}^2)\dot{q}_1^2+(\phi_{x2}^2+\phi_{y2}^2+\phi_{z2}^2)\dot{q}_2^2+2(\phi_{x1}\phi_{x2}+\phi_{x1}\phi_{x2}+\phi_{x1}\phi_{x2})\dot{q}_1\dot{q}_2\right)dV$$
$$=\int_V \left((\phi_{x1}^2+\phi_{y1}^2+\phi_{z1}^2)\dot{q}_1^2+(\phi_{x2}^2+\phi_{y2}^2+\phi_{z2}^2)\dot{q}_{\mathbf{2}}^2\right)dV$$

(Equation 3.50)

- Group 2 (simplified using Property 3.4):

$$\int_V (\Omega_x(-2\dot{u}_y u_z+2u_y\dot{u}_z)+\Omega_y(2\dot{u}_x u_z-2u_x\dot{u}_z)+\Omega_z(-2\dot{u}_x u_y+2u_x\dot{u}_y))dV$$
$$=\int_V (-2\Omega_z(\phi_{x1}\phi_{y2}-\phi_{x2}\phi_{y1})\dot{q}_1 q_2+2\Omega_z(\phi_{x1}\phi_{y2}-\phi_{x2}\phi_{y1})q_1\dot{q}_2)dV$$

(Equation 3.51)

- Group 3 (simplified using Property 3.2):

$$\int_V [\Omega_x^2(u_y^2+u_z^2)+\Omega_y^2(u_x^2+u_z^2)+\Omega_z^2(u_x^2+u_y^2)]dV$$
$$\begin{aligned}
=\; & \int_V \Omega_x^2[(\phi_{y1}^2+\phi_{z1}^2)q_1^2+(\phi_{y2}^2+\phi_{z2}^2)q_2^2+2(\phi_{y1}\phi_{y2}+\phi_{z1}\phi_{z2})]dV \\
& +\int_V \Omega_y^2[(\phi_{x1}^2+\phi_{z1}^2)q_1^2+(\phi_{x2}^2+\phi_{z2}^2)q_2^2+2(\phi_{x1}\phi_{x2}+\phi_{z1}\phi_{z2})]dV \\
& +\int_V \Omega_z^2[(\phi_{x1}^2+\phi_{y1}^2)q_1^2+(\phi_{x2}^2+\phi_{y2}^2)q_2^2+2(\phi_{x1}\phi_{x2}+\phi_{y1}\phi_{y2})]dV \\
=\; & \int_V \Omega_x^2[(\phi_{y1}^2+\phi_{z1}^2)q_1^2+(\phi_{y2}^2+\phi_{z2}^2)q_2^2]dV \\
& +\int_V \Omega_y^2[(\phi_{x1}^2+\phi_{z1}^2)q_1^2+(\phi_{x2}^2+\phi_{z2}^2)q_2^2]dV \\
& +\int_V \Omega_z^2[(\phi_{x1}^2+\phi_{y1}^2)q_1^2+(\phi_{x2}^2+\phi_{y2}^2)q_2^2]dV
\end{aligned}$$

(Equation 3.52)

- Group 4 (simplified using Properties 3.3 and 3.4):

$$
\begin{aligned}
&\int_V (-2\Omega_y\Omega_z u_y u_z - 2\Omega_x\Omega_z u_x u_z - 2\Omega_x\Omega_y u_x u_y) dV \\
&= -\int_V 2\Omega_y\Omega_z[\phi_{y1}\phi_{z1}q_1^2 + (\phi_{y1}\phi_{z2} + \phi_{y2}\phi_{z1})q_1q_2 + \phi_{y2}\phi_{z2}q_2^2]dV \\
&\quad -\int_V 2\Omega_x\Omega_z[\phi_{x1}\phi_{z1}q_1^2 + (\phi_{x1}\phi_{z2} + \phi_{x2}\phi_{z1})q_1q_2 + \phi_{x2}\phi_{z2}q_2^2]dV \\
&\quad -\int_V 2\Omega_x\Omega_y[\phi_{x1}\phi_{y1}q_1^2 + (\phi_{x1}\phi_{y2} + \phi_{x2}\phi_{y1})q_1q_2 + \phi_{x2}\phi_{y2}q_2^2]dV \\
&= 0
\end{aligned}
\qquad \text{(Equation 3.53)}
$$

Combining Equations 3.50-3.53, the kinetic energy (T_E) is expressed as:

$$
\begin{aligned}
T_E &= \frac{1}{2}\rho|\vec{v}|^2 \\
&= \frac{1}{2}\rho\int_V \left[(\phi_{x1}^2 + \phi_{y1}^2 + \phi_{z1}^2)\dot{q}_1^2 + (\phi_{x2}^2 + \phi_{y2}^2 + \phi_{z2}^2)\dot{q}_2^2\right]dV \\
&+ \frac{1}{2}\rho\int_V \left[-2\Omega_z(\phi_{x1}\phi_{y2} - \phi_{x2}\phi_{y1})\dot{q}_1q_2 + 2\Omega_z(\phi_{x1}\phi_{y2} - \phi_{x2}\phi_{y1})q_1\dot{q}_2\right]dV \\
&+ \frac{1}{2}\rho\int_V \Omega_x^2\left[\left(\phi_{y1}^2 + \phi_{z1}^2\right)q_1^2 + \left(\phi_{y2}^2 + \phi_{z2}^2\right)q_2^2\right]dV \\
&+ \frac{1}{2}\rho\int_V \Omega_y^2\left[\left(\phi_{x1}^2 + \phi_{z1}^2\right)q_1^2 + \left(\phi_{x2}^2 + \phi_{z2}^2\right)q_2^2\right]dV \\
&+ \frac{1}{2}\rho\int_V \Omega_z^2\left[\left(\phi_{x1}^2 + \phi_{y1}^2\right)q_1^2 + \left(\phi_{x2}^2 + \phi_{y2}^2\right)q_2^2\right]dV
\end{aligned}
\qquad \text{(Equation 3.54)}
$$

These expressions will be used later in Section 3.4 in the derivation of Lagrangian motional equation.

3.1.2. Potential Energy (V_E)

Assuming that there is negligible nonlinear stiffness, potential energy (V_E) can be expressed using effective stiffnesses along the two axes (k_{11}, k_{22}) and cross-axial stiffness (k_{12} (=k_{21})) as:

$$
V_E = \frac{1}{2}(k_{11}q_1^2 + k_{22}q_2^2 + 2k_{12}q_1q_2) \qquad \text{(Equation 3.55)}
$$

In Chapter 2, we derived that the k_{11}, k_{22}, and k_{12} (=k_{21}) for a sensor axes, separated from the principal stiffness axes by θ_ω, are related to the principal stiffnesses k_1 and k_2, and θ_ω by:

$$\begin{bmatrix} k_{11} & k_{12} \\ k_{21} & k_{22} \end{bmatrix} = \begin{bmatrix} \cos^2\theta_\omega k_1 + \sin^2\theta_\omega k_2 & \cos\theta_\omega \sin\theta_\omega (k_1 - k_2) \\ \cos\theta_\omega \sin\theta_\omega (k_1 - k_2) & \sin^2\theta_\omega k_1 + \cos^2\theta_\omega k_2 \end{bmatrix} \qquad \text{(Equation 3.56)}$$

The principal stiffnesses (k_1, k_2) are contributed by mechanical and electrical stiffnesses. The mechanical stiffness of a complex 3D gyroscope is difficult to be found analytically, and we need to rely on the finite element method (FEM), where we can derive the stiffness from effective mass and a resonance frequency. An electrical spring constant is generated from nonlinear electrostatic force between parallel plates, and they are used to tune the resonance frequencies of a gyro. For parallel plate electrodes with area A, nominal gap g_{tuning}, polarization voltage V_p, and displacement u perpendicular to the plates, the amount of electrical energy (E_{energy}) stored across the plates is:

$$E_{electrical} = \frac{1}{2}\frac{\varepsilon A}{g_{tuning} - u}V_p^2 \qquad \text{(Equation 3.57)}$$

An electrical stiffness is found by differentiating the $E_{electrical}$ twice using u:

$$\begin{aligned} k_{electrical} &= -\frac{d^2 E_{Electrical}}{du^2} \\ &= -\frac{1}{4}\frac{\varepsilon A}{g_{tuning}^3}V_p^2 \end{aligned} \qquad \text{(Equation 3.58)}$$

The $k_{electrical}$ is always a negative value and lowers a resonance frequency. According to where a tuning electrode is placed, k_1 and k_2 can be selectively controlled.

3.1.3. Damping Energy (D_E)

The change in the damping energy (dD_E) is expressed using in-axis and off-axis damping constants ($c_{11}, c_{22}, c_{12}, c_{21}$), modal displacements ($q_1$, q_2), and modal velocities ($\dot{q}_1, \dot{q}_2$) as:

$$dD = c_{11}\dot{q}_1 dq_1 + c_{22}\dot{q}_2 dq_2 + c_{12}\dot{q}_2 dq_1 + c_{12}\dot{q}_1 dq_2 \qquad \text{(Equation 3.59)}$$

The effective damping constants in the sensor coordinate, separated from the principal damping axes by θ_τ, are:

$$\begin{bmatrix} c_{11} & c_{12} \\ c_{21} & c_{22} \end{bmatrix} = \begin{bmatrix} \cos^2\theta_\tau c_1 + \sin^2\theta_\tau c_2 & \cos\theta_\tau \sin\theta_\tau (c_1 - c_2) \\ \cos\theta_\tau \sin\theta_\tau (c_1 - c_2) & \sin^2\theta_\tau c_1 + \cos^2\theta_\tau c_2 \end{bmatrix} \qquad \text{(Equation 3.60)}$$

3.1.4. Derivation of Lagrangian Equation

The kinetic, potential, and damping energies (T_E, V_E, D_E) from Sections 3.1.1-3.1.3 are applied in Equations 3.1 and 3.2. First, inertia terms in the wineglass modes 1 and 2 are derived as:

$$\begin{aligned} \frac{d}{dt}\left(\frac{\partial T_E}{\partial \dot{q}_1}\right) = {} & \left[\int_V \rho\left(\phi_{x1}^2 + \phi_{y1}^2 + \phi_{z1}^2\right) dV\right]\ddot{q}_1 \\ & - \Omega_z \left[\int_V \rho\left(\phi_{x1}\phi_{y2} - \phi_{x2}\phi_{y1}\right) dV\right]\dot{q}_2 - \dot{\Omega}_z \left[\int_V \rho\left(\phi_{x1}\phi_{y2} - \phi_{x2}\phi_{y1}\right) dV\right] q_2 \end{aligned}$$

(Equation 3.61)

$$\begin{aligned} \frac{\partial T_E}{\partial q_1} = {} & \Omega_z \left[\int_V \rho\left(\phi_{x1}\phi_{y2} - \phi_{x2}\phi_{y1}\right) dV\right]\dot{q}_2 \\ & + \Omega_x^2 \left[\int_V \rho\left(\phi_{y1}^2 + \phi_{z1}^2\right) dV\right] q_1 + \Omega_y^2 \left[\int_V \rho\left(\phi_{x1}^2 + \phi_{z1}^2\right) dV\right] q_1 + \Omega_z^2 \left[\int_V \rho\left(\phi_{x1}^2 + \phi_{y1}^2\right) dV\right] q_1 \end{aligned}$$

(Equation 3.62)

$$\frac{d}{dt}\left(\frac{\partial T_E}{\partial \dot{q}_2}\right)=\left[\int_V \rho\left(\phi_{x2}^2+\phi_{y2}^2+\phi_{z2}^2\right)dV\right]\ddot{q}_2$$
$$+\Omega_z\left[\int_V \rho\left(\phi_{x1}\phi_{y2}-\phi_{x2}\phi_{y1}\right)dV\right]\dot{q}_1+\dot{\Omega}_z\left[\int_V \rho\left(\phi_{x1}\phi_{y2}-\phi_{x2}\phi_{y1}\right)dV\right]q_1$$

(Equation 3.63)

$$\frac{\partial T_E}{\partial q_2}=-\Omega_z\left[\int_V \rho\left(\phi_{x1}\phi_{y2}-\phi_{x2}\phi_{y1}\right)dV\right]\dot{q}_1$$
$$+\Omega_x^2\left[\int_V \rho\left(\phi_{y2}^2+\phi_{z2}^2\right)dV\right]q_2+\Omega_y^2\left[\int_V \rho\left(\phi_{x2}^2+\phi_{z2}^2\right)dV\right]q_2+\Omega_z^2\left[\int_V \rho\left(\phi_{x2}^2+\phi_{y2}^2\right)dV\right]q_2$$

(Equation 3.64)

Stiffness terms are calculated by differentiating the V_E using q_1 and q_2:

$$\frac{\partial V_E}{\partial q_1}=k_{11}q_1+k_{12}q_2$$ (Equation 3.65)

$$\frac{\partial V_E}{\partial q_2}=k_{22}q_2+k_{22}q_1$$ (Equations 3.66)

Damping terms are calculated by differentiating the D_E using $\dot{q}_1$ and $\dot{q}_2$:

$$\frac{\partial D_E}{\partial q_1}=c_{11}\dot{q}_1+c_{12}\dot{q}_2$$ (Equation 3.67)

$$\frac{\partial D_E}{\partial q_2}=c_{22}\dot{q}_2+c_{12}\dot{q}_1$$ (Equations 3.68)

Then the motional equation for the two wineglass modes is derived as:

$$\begin{bmatrix} M_1 & 0 \\ 0 & M_2 \end{bmatrix}\begin{bmatrix} \ddot{q}_1 \\ \ddot{q}_2 \end{bmatrix}+\begin{bmatrix} 0 & -2\gamma\Omega_z \\ 2\gamma\Omega_z & 0 \end{bmatrix}\begin{bmatrix} \dot{q}_1 \\ \dot{q}_2 \end{bmatrix}+\begin{bmatrix} c_{11} & c_{12} \\ c_{21} & c_{22} \end{bmatrix}\begin{bmatrix} \dot{q}_1 \\ \dot{q}_2 \end{bmatrix}$$
$$+\begin{bmatrix} k_{11} & k_{12} \\ k_{21} & k_{22} \end{bmatrix}\begin{bmatrix} q_1 \\ q_2 \end{bmatrix}+\begin{bmatrix} 0 & -\gamma\dot{\Omega}_z \\ \gamma\dot{\Omega}_z & 0 \end{bmatrix}\begin{bmatrix} q_1 \\ q_2 \end{bmatrix}$$
$$-\begin{bmatrix} \alpha_1\Omega_x^2+\beta_1\Omega_y^2+\mu_1\Omega_z^2 & 0 \\ 0 & \alpha_2\Omega_x^2+\beta_2\Omega_y^2+\mu_2\Omega_z^2 \end{bmatrix}\begin{bmatrix} q_1 \\ q_2 \end{bmatrix}=\begin{bmatrix} F_1 \\ F_2 \end{bmatrix}$$

(Equation 3.69)

Equations 3.70-3.78 show the relationship between the mode shape functions and the effective mass (*M*), Coriolis mass (γ), and centrifugal mass (α, β, μ) of a three-dimensional gyroscope, operating in the wineglass mode.

$$M_1 = \int_V \rho(\phi_{x1}^2 + \phi_{y1}^2 + \phi_{z1}^2)dV$$ (Effective mass for mode 1) (Equation 3.70)

$$M_2 = \int_V \rho(\phi_{x2}^2 + \phi_{y2}^2 + \phi_{z2}^2)dV$$ (Effective mass for mode 2) (Equation 3.71)

$$\gamma = \int_V \rho(\phi_{x1}\phi_{y2} - \phi_{x2}\phi_{y1})dV$$ (Coriolis mass) (Equation 3.72)

$$\alpha_1 = \int_V \rho(\phi_{y1}^2 + \phi_{z1}^2)dV$$ (X-axis centrifugal mass for mode 1) (Equation 3.73)

$$\alpha_2 = \int_V \rho(\phi_{y2}^2 + \phi_{z2}^2)dV$$ (X-axis centrifugal mass for mode 2) (Equation 3.74)

$$\beta_1 = \int_V \rho(\phi_{x1}^2 + \phi_{z1}^2)dV$$ (Y-axis centrifugal mass for mode 1) (Equation 3.75)

$$\beta_2 = \int_V \rho(\phi_{x2}^2 + \phi_{z2}^2)dV$$ (Y-axis centrifugal mass for mode 2) (Equation 3.76)

$$\mu_1 = \int_V \rho(\phi_{x1}^2 + \phi_{y1}^2)dV$$ (Z-axis centrifugal mass for mode 1) (Equation 3.77)

$$\mu_2 = \int_V \rho(\phi_{x2}^2 + \phi_{y2}^2)dV$$ (Z-axis centrifugal mass for mode 2) (Equation 3.78)

For an ideally symmetric gyroscope, effective mass and centrifugal mass for the two axes are the same. For *n*th order wineglass mode, the angular gain (A_g) is calculated using *M* and γ as:

$$A_g = \frac{\gamma}{nM}$$ (Equations 3.79)

Another property of a wineglass mode gyro is that the Coriolis mass for x- and y- axis rotation is zero from the symmetry in the modal shape (Property 3.4).

$$\int_v [\phi_{y1}(p)\phi_{z2}(p) - \phi_{y2}(p)\phi_{z1}(p)]dV = 0 \quad \text{(Coriolis mass for x-axis rotation)}$$

(Equation 3.80)

$$\int_v [\phi_{x1}(p)\phi_{z2}(p) - \phi_{x2}(p)\phi_{z1}(p)]dV = 0 \qquad \text{(Coriolis mass for y-axis rotation)}$$

(Equation 3.81)

This is because under a single wineglass mode, all the cross-axial products of the shape functions $\phi_{x1}\phi_{z2}$, $\phi_{x2}\phi_{z1}$, $\phi_{y1}\phi_{z2}$, $\phi_{y2}\phi_{z1}$ are sinusoidal functions of azimuthal angle (φ), which becomes zero when they are integrated over the perimeter (φ from 0 to 2π radians). Due to this property, a wineglass mode gyroscope operating in the wineglass modes of the same order can measure yaw rotation (direction parallel to the symmetry axis), but it cannot measure planar rotation. To create nonzero Coriolis mass for x- and y- axis rotation, the gyro has to be operated in two different wineglass modes (order number n_1 and n_2), where the two mode orders are different by 1 ($n_1 - n_2 = \pm 1$) [99]. The effectiveness of using the wineglass modes of two different orders depends on whether or not the two modes have a small enough frequency difference so that they can be electrically tuned and matched, which depends entirely on the shape of a gyro.

3.2. Numerical Calculation of Physical Parameters Using ANSYS

The physical parameters can be most easily calculated using ANSYS, because this program allows users to access displacement data of every element and perform arithmetic calculation using the data. The steps to calculate the device parameters are the following. First, the resonance frequencies are calculated from modal analysis. During this calculation, ANSYS can save the displacement amplitudes of the elements. Next, shape functions (ϕ_{x1}, ϕ_{y1}, ϕ_{z1}, ϕ_{x2}, ϕ_{y2}, ϕ_{z2}) are calculated from the displacement amplitudes along x, y, and z axes (u_x, u_y, u_z) by first evaluating the amplitude of the displacement vector of every element ($\sqrt{u_x^2+u_y^2+u_z^2}$) and then and normalizing u_x, u_y, and u_z using the maximum value of $\sqrt{u_x^2+u_y^2+u_z^2}$. Then, using the shape functions, the volume of elements (ΔV), and a density ρ, the physical parameters of each element ($M(p)$, $\gamma(p)$, $\alpha(p)$, $\beta(p)$, $\mu(p)$) are calculated. The parameters of elements are added over the entire geometry to find the M, γ, α, β, and μ. A batch code for calculating the M and γ of a Cylindrical Rate-Integrating Gyro (CING) is shown in Appendix B.

3.3. Summary

In this chapter, the physical parameters of an arbitrary 3-dimensional wineglass mode gyro are derived from its modal shape functions. The physical parameters include effective mass (M), angular gain (A_g), and centrifugal mass (α, β, μ). The steps for calculating these parameters using ANSYS are introduced. This method will be used to compare the physical parameters of several axisymmetric rate-integrating gyroscope (RIG) geometries in Chapter 5. We also find that due to symmetry in the modal shape, a gyro operating in the wineglass mode of the same order has zero Coriolis mass (γ) for measuring planar rotation. In order to measure planar rotation, a gyro has to be operated in the wineglass modes of two different orders that are different by 1.

CHAPTER 4.

PLANAR-RATE-SENSING QUAD-MASS BALANCED OSCILLATING GYROSCOPE (BOG)

In this chapter, the Balanced Oscillating Gyro (BOG) architecture, microfabrication technology, and the readout-and-control circuitry scheme are described. The aim of the BOG design is to use balanced modes for their vibration immunity and to use only a single anchor at the center of the device to reduce drift due to changes in thermoresidual stress. Reducing the number of anchors increases the difficulty of keeping parasitic resonance modes separated from the operational modes. FEM is used extensively to study the impact of design choices on the BOG parameters. The structure and placement of the coupling beams are studied in order to separate the parasitic modes from the operating modes.

The BOG is fabricated using the Si-on-glass (SOG) process with better etch quality due to improved etch-heat dissipation and without the footing problem. BOG prototypes are evaluated using analog interface circuitry.

4.1. Structure of the Balanced Oscillating Gyroscope (BOG)

The BOG is a planar rate-sensing gyroscope. The architecture of the BOG is shown in Figure 4.1. The device is symmetric across the y-axis and is constructed with masses, drive springs, drive-coupling springs, sense springs, sense-coupling springs, and semi-open frames.

The masses are connected to the semi-open frames via drive springs (folded beams), and the masses face each other across the y-axis via drive-coupling springs (folded beam). The semi-open frames are connected to the anchor via the sense springs and the sense-coupling springs. The anchor is located at the center of the device. The sense springs are torsion beams, connected at each end to the midpoint of one of the frames. The sense-coupling beam has two sections of perpendicular beams connected in the middle. The semi-open frame supports the masses, and it also serves as a coupling beam between the two pairs of masses. The location of the semi-open frame is highlighted on the top view picture in Figure 4.2. A lumped mass-spring representation of the BOG is shown in Figure 4.3. The spring constant along the x-axis is provided by the driving spring, drive-coupling spring, and the semi-open frame. The spring constant along the z-axis is provided by sense spring and sense-coupling spring.

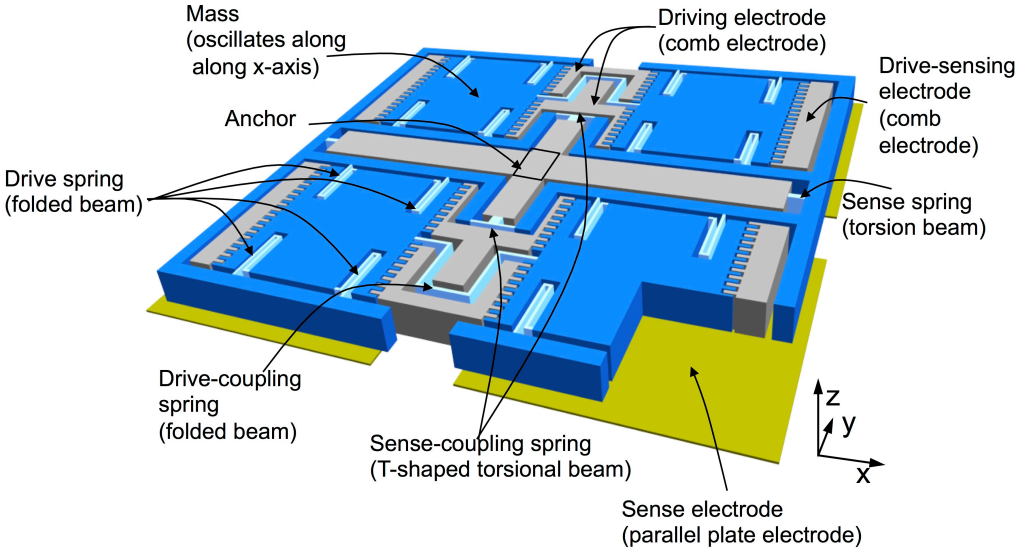

Figure 4.1. Architecture of the Balanced-Oscillating Gyroscope (BOG).

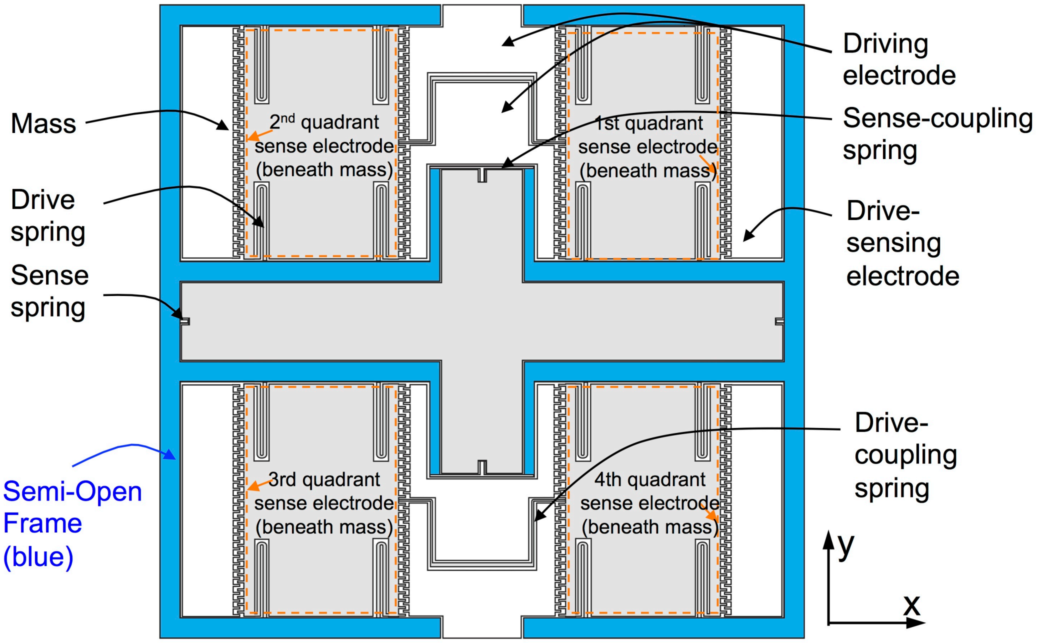

Figure 4.2. Top view of the BOG showing sensor components. Semi-open frame is highlighted in blue.

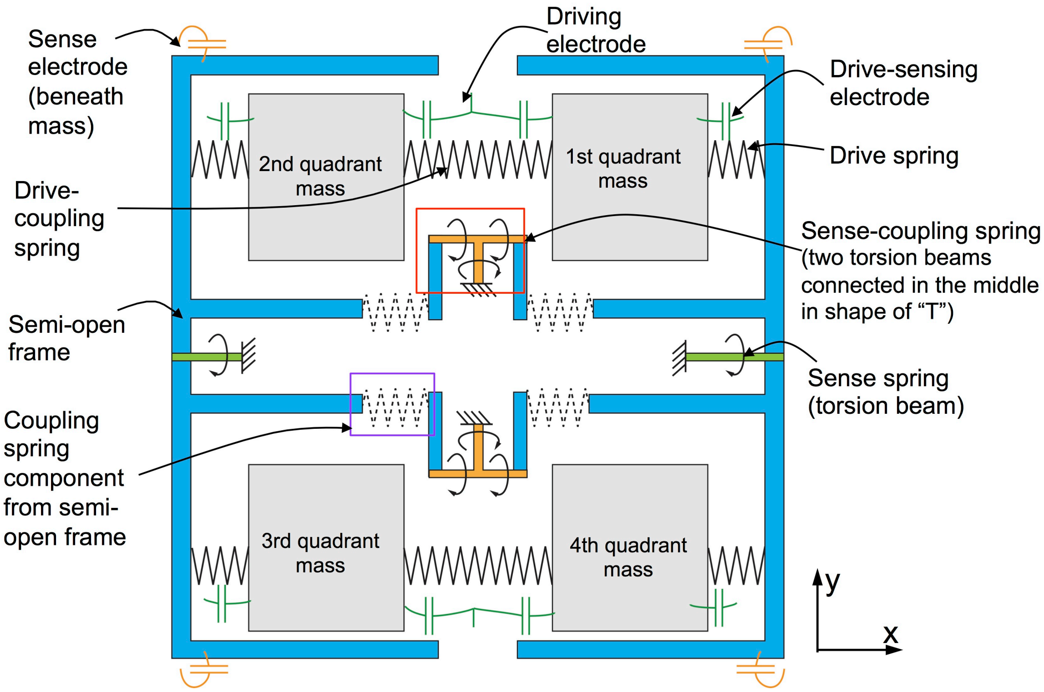

Figure 4.3. Lumped mass representation of the BOG along with driving, driving-sensing, and sense electrodes.

The BOG has three types of electrodes. The electrodes to actuate the masses along the x-axis are named the driving electrodes. The electrodes to measure the displacement of the masses along the x-axis are called the drive-sensing electrodes. Both the driving and drive-sensing electrodes are comb-drive electrodes. The bottom electrodes placed on the glass substrate are the rate-sensing electrodes. The current (prototype) version of BOG uses bias voltages on the sensing electrodes to electrically tune the resonance frequency along the sense axis.

4.2. Resonance Mode Shapes of the BOG

Figures 4.4 and 4.5 show the driving and the sensing mode shapes of the BOG simulated using ANSYS.

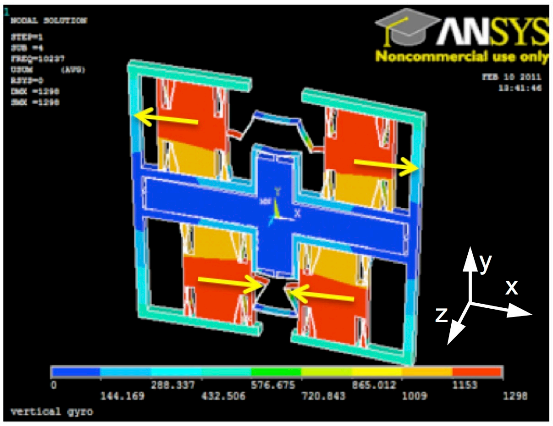

Figure 4.4. Displacement pattern in the driving mode

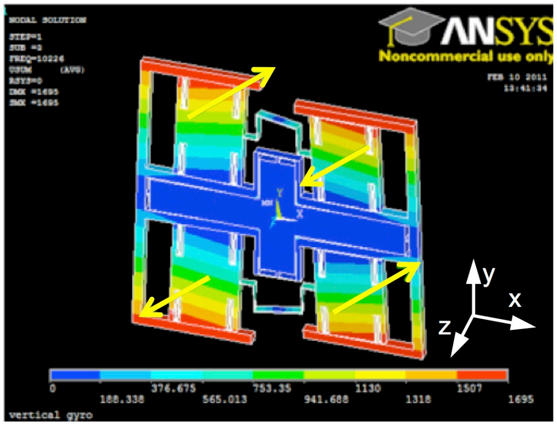

Figure 4.5. Displacement pattern in the sensing mode.

In the driving mode, the masses oscillate linearly along the x-axis. The masses linked with the drive-coupling springs oscillate in the opposite phase, and the two sets of masses along each side of the gyro oscillate in the opposite phase. Due to the direction of the mass's movement in the driving mode, the frames rotate around the z-axis in opposite directions. When the sensor experiences y-axis rotation with a rate $\overrightarrow{\Omega_y}$, the Coriolis force developed for each mass along the z-axis is:

$$\overrightarrow{F_{Coriolis}(z)} = 2kM\vec{v} \times \overrightarrow{\Omega_y}$$

[M_{drive}: effective mass along drive axis, $\vec{v}$: velocity vector, $\overrightarrow{\Omega_y}$: y-axis rotation rate vector, k: angular gain factor (1 for tuning-fork gyro)] (Equation 4.1)

The Coriolis force induces the sensing mode. In the sensing mode, the semi-open frames along with the masses oscillate torsionally along the sense springs in the opposite phase. Sensing mode signal is measured from the sum of capacitance change from first and third quadrants minus the sum of capacitance change from second and fourth quadrants (Equation 4.2). The four quadrants of the gyro are shown in Figure 4.2.

$$\Delta C_{sense} = \Delta C_{z1} - \Delta C_{z2} + \Delta C_{z3} - \Delta C_{z4} \qquad \text{(Equation 4.2)}$$

In Equation 4.2, ΔC_{zn} is the capacitance change measured from the bottom electrode in the *n*th quadrant. There are three parasitic modes along the driving axis and one parasitic mode along the sensing axis. In the first parasitic driving mode, the masses in the 1st and 2nd quadrants move in phase with each other and in opposite phase with the masses in the 3rd and 4th quadrants (Figure 4.6 (a)). In the second parasitic driving mode, the masses in all quadrants move in phase (Figure 4.6 (b)). In the third parasitic driving mode, the masses in the 1st and 2nd quadrants move in opposite phase and in phase with the masses in the 3rd and 4th quadrants (Figure 4.6 (c)). In the parasitic sensing mode, the two semi-open frames rotate in phase (Figure 4.6 (d)).

The frequencies of the driving and sensing modes and the four parasitic modes of the BOG are determined by the dimensions of all the springs as well as the dimensions of the semi-open frames. Due to the complexity of the sensor geometry, dimensions of each spring are designed using FEM. The sensor is designed to operate in the vicinity of

10kHz to optimize its scale factor and vibration insensitivity.

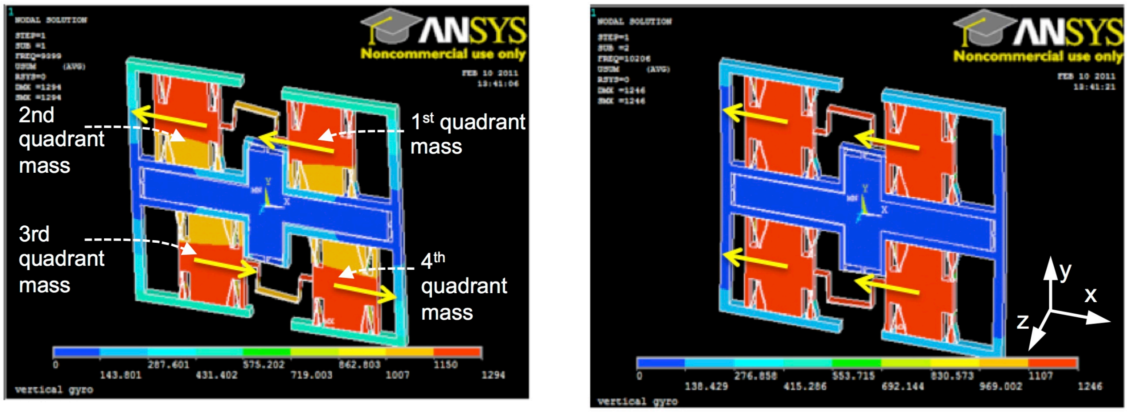

(a) Parasitic driving mode 1 (b) Parasitic driving mode 2

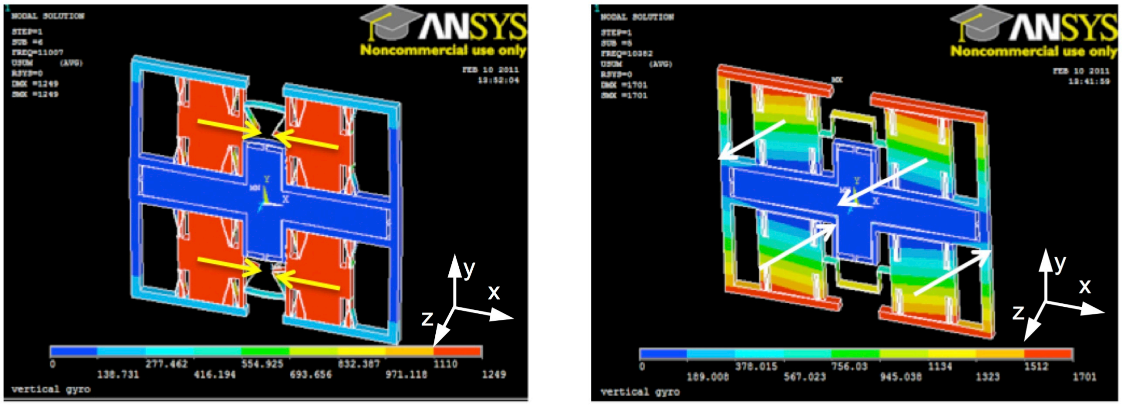

(c) Parasitic driving mode 3 (d) Parasitic sensing mode 1

Figure 4.6. Shapes of the three parasitic driving modes and one parasitic sensing mode.

4.3. Design of Driving and Sensing Coupling Springs

A vibratory gyro's sensitivity to shock or vibration reduces as the ratio between the parasitic frequency and the operating frequency increases. Vibration and shock cause the largest error in the sensor when they are along the direction of the Coriolis force. From this reason, the mode relationship between the parasitic sensing mode and the sensing mode is more important than the mode relationship between the parasitic driving modes and the driving mode.

The separation between parasitic modes and operational modes can be controlled with the combination of anchor placement and the design of the coupling springs. In the

BOG, it is challenging to have large mode separation because we try to achieve stable thermal characteristics by using only a single anchor, so we must rely only on the design of the coupling spring for mode separation. In this section, the design of the drive and sense-coupling spring is discussed.

4.3.1. Driving Coupling Spring

The driving coupling spring is a conventional folded spring, connecting the two masses in the middle. The length and the width of the spring is designed to separate the driving and the parasitic modes by approximately 10%.

4.3.2. Sensing Coupling Spring

The frequencies of the sensing and the parasitic sensing modes are affected by a number of parameters, including the length and the width of the semi-open frame and of the T-spring that connects the two semi-open frames in the middle of the sensor. The frequencies have a large sensitivity to the dimension and placement of the T-spring.

The geometry of the T-spring is shown in Figure 4.7. It consists of a beam that is parallel to the x-axis (Section A and C) and a beam that is parallel to the y-axis (Section B). The ends of Sections A, B, and C are connected. Throughout this discussion we will call the beam in the T-spring parallel to the x-axis as the lateral beam and the beam in the T-spring parallel to the y-axis as the vertical beam. The difference between the stiffness of the sensing and parasitic sensing modes is due to the torsional flexibility at the junction of the lateral and vertical beams. Because of the torsional flexibility at this joint, the spring stores different amounts of elastic energy in the sensing mode and in the parasitic sensing mode.

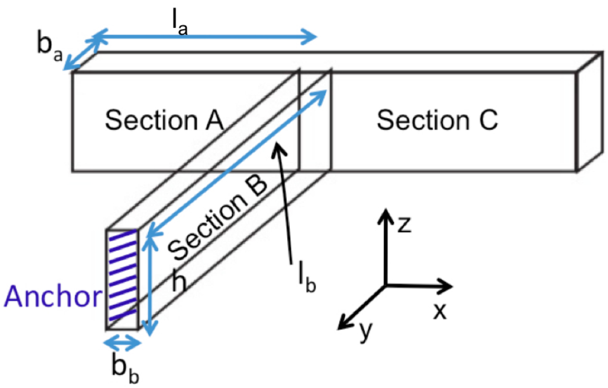

Figure 4.7. T-shaped sense coupling beam.

By calculating the difference in the stored elastic energy under a given displacement, the effective stiffness for each mode can be calculated as [100]:

$$k_z = \frac{2 \times Energy_{elastic}}{d_z^2} \qquad \text{(Equation 4.3)}$$

In both the sensing and parasitic sensing modes, the sense-coupling beam is affected by z-axis bending at the outer ends of Section A and Section C.

The elastic energy of the sense-coupling spring along z-axis bending can be calculated in the following way. In the sensing mode, the ends of the lateral beam are deflected along complementary z-directions. The deformation is made by first applying a positive force at the end of Section A to deflect the beam by d_z (Figure 4.8 (a)) and then applying a negative force at the end of Section C to deflect the right end of the lateral beam by $-d_z$ (Figure 4.8 (b)).

In Figure 4.8 (a), as the left end of the lateral beam is pushed upwards by d_z, if the torsional stiffness of the lateral beam is much larger than the torsional flexibility of the vertical beam, the vertical beam will tilt with respect to the y-axis. The lateral beam will stay almost flat, like a lever. Due to the lever action, the amount of strain energy stored in the T-spring by deflection $-d_z$ at the end of section C from the original position, in

Figure 4.8 (b), is much smaller than the amount of energy stored in the step performed in Figure 4.8 (a). This is because both the distance of deflection is smaller than the deflection distance in the previous step and the magnitude of the force in this step is smaller than the magnitude of the force needed at the previous step ($F_{z1} > F_{z2}$).

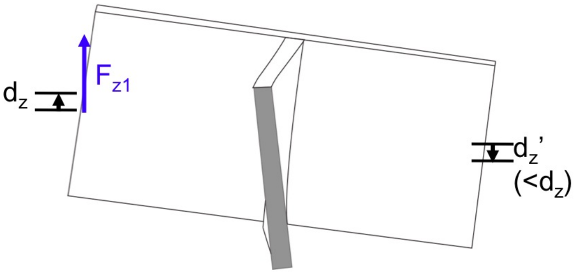

(a) Z-axis force (F_{z1}) applied from the left end of the lateral beam, causing z-axis deflection in the lateral beam (d_z at the left end and d_z' at the right end).

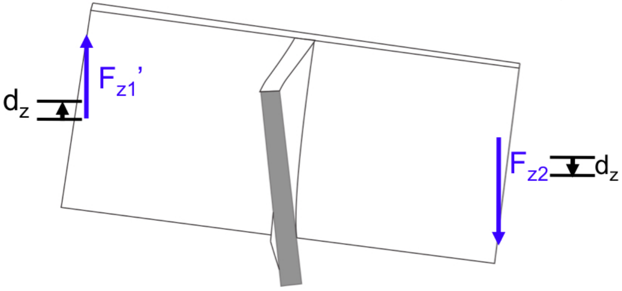

(b) Z-axis force F_{z2} is applied from the right end of the lateral beam and the left-end force is adjusted, causing z-axis deflection with the same amplitude (d_z) at both ends of the lateral beam.

Figure 4.8. Steps of deforming the sense-coupling spring to have the complementary deflection (d_z) at both ends of the lateral beam: In step (a), z-axis force (F_{z1}) is applied upward, causing deflection of d_z at the left end and d_z' ($<d_z$) at the right end. In step (b), another z-axis force (F_{z2}) is applied downward and the left-end force is adjusted (F_{z1}'), causing deflection of d_z at both ends. ($F_{z1}'=F_{z2}$).

A similar analysis can be made by deforming the T-spring to have the deflection at each end of the lateral beam in the same direction for the parasitic sense mode. The steps of deforming the spring are illustrated in Figure 4.9. First, a z-axis force is applied at the left end of the lateral beam which deflects the end of the beam by d_z. Due to the flexibility at the joint, the lateral beam will tilt like a lever, deflecting the beam by $-d_z'$ at the right end of the lateral beam (Figure 4.9 (a)). Then another force (F_{z2}') is applied from the right end of the lateral beam in the upward direction (Figure 4.9 (b)). At this time, the force at the left end is adjusted to (F_{z2}''). The energy needed at step (b) is larger than the energy used at step (a), because the amount of deflection is larger (d_z+d_z') and the force used in step (b) is stronger than the force used in step (a) because the moment caused by the two forces are in the opposite directions.

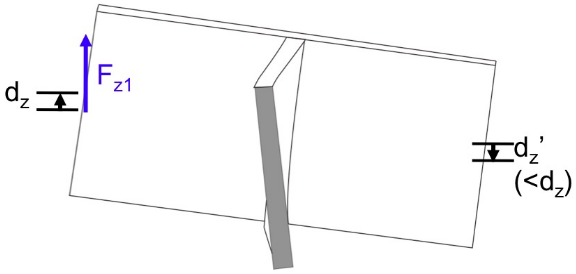

(a) Z-axis force (F_{z1}) is applied from the left end of the lateral beam, causing z-axis deflection in the lateral beam (d_z at the left end and d_z' at the right end).

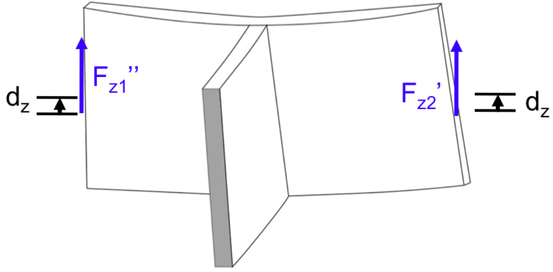

(b) Z-axis force is applied downward from the right end of the lateral beam, and the force applied at the left end of the beam is adjusted. The lateral beam of the spring is deflected by the same amount (d_z) at both ends (F_{z1}'' = F_{z2}').

Figure 4.9. Steps of deforming the lateral beam of the T-spring to have the same deflection in the same direction (d_z) at both ends. In step (a), z-axis force (F_{z1}) is applied upward, causing deflection d_z at the left end and d_z' (<d_z) at the right end. In step (b), another z-axis force (F_{z2}') is applied upward, overcoming the deflection made by the force applied at the left end of the beam. The force at the left end of the beam is adjusted (F_{z1}'') to have the same deflection (d_z) at both ends.

This analysis indicates that the amount of elastic energy stored in the coupling beam in complementary bending along the z-axis at the ends of the lateral beam is smaller than the energy stored from bending both ends of the beam in the same direction. This means that the stiffness of the coupling spring for the sensing mode is smaller than the stiffness for the parasitic sensing mode when we consider only the bending shapes along the z-axis.

Next, we consider the difference in the stored energy through torsion along the x-axis for the lateral beam. In the sensing mode, the outer ends of the lateral beam are rotated by x-axis moments in the opposite directions. In the parasitic sense mode, the outer ends of the lateral beam are rotated by x-axis moments in the same direction. Figure 4.10 shows the steps of the application of torques in order to have the deformation shape with complementary torsional angles at both ends of the lateral beam: first, a negative torque along x-axis ($-T_x$) is applied at the left end of the lateral beam (Figure 4.10 (a)). The torque rotates Section A by an angle $-\theta_x$, and due to the torsional flexibility at the junction of the lateral and vertical beams, the torque also rotates the end of Section C by angle $-\theta_x'$ ($\theta_x' < \theta_x$). Next, another x-axis torque T_{x2} is applied from the right end of the lateral beam in the opposite direction (Figure 4.10 (b)). The torque at the left end the lateral beam is adjusted to have rotation angle at Section A and Section C of $-\theta_x$ and θ_x, respectively. The amount of strain energy contained at step (b) is larger than the energy that is contained at step (a). This is because of the larger torsion angle ($\theta_x'+\theta_x$) and because the torque applied at step (b) (T_{x2}) is larger than the torque applied at step (a) (T_{x1}), as the torques are acting in the opposite directions.

Figure 4.11 shows the steps to apply torques to achieve an equal torsional angle from both sides of the lateral beam along the same direction. This is the case for the parasitic sensing mode. First, a negative x-axis torque ($-T_{x1}$) is applied at the left end of the lateral beam, and the beam is rotated by $-\theta_x$ at the left end and $-\theta_x'$ at the right end of the lateral beam (Figure 4.11 (a)) ($\theta_x > \theta_x'$). Next, another torque is applied at the right end of the lateral beam ($-T_{x2}'$), and the torque at the left end of the lateral beam is adjusted to a new value ($-T_{x1}''$) to have deflection angle of $-\theta_x$ at both ends of the lateral beam (Figure 4.11 (b)). The amount of elastic energy contained in step (b) is smaller than the elastic energy contained in step (a). This is because the angle of rotation is smaller (θ_x-θ_x') and because the amount of torque applied at step (b) ($-T_{x2}'$) is smaller than the torque applied at step (a), as the two torques applied at the sides of the lateral beam are acting in the same direction.

This analysis indicates that the torsion of the lateral beam of the sense-coupling spring in the opposite angle contains more energy than when the torsion is along the same

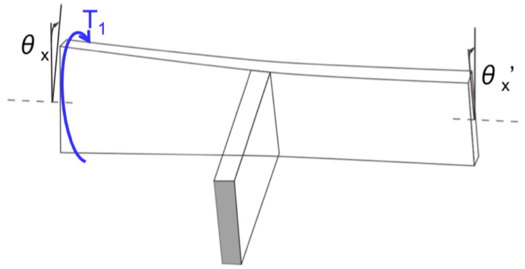

(a) X-axis torque T_{x1} is applied at the left end of the lateral beam, causing rotation angle of $-\theta_x$ at the left end and $-\theta_x'$ at the right end of the lateral beam ($\theta_x' < \theta_x$) due to torsional flexibility at the joint.

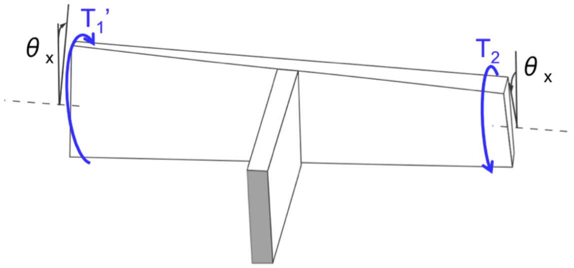

(b) X-axis torque along positive direction T_{x2} is applied at the right end of the lateral beam, and the torque at the left end of lateral beam is adjusted to T_{x1}' to cause complemenatry rotation angles at both ends of the beam ($-\theta_x$ at left end and θ_x at right end of the beam) ($T_{x1}' = T_{x2}$).

Figure 4.10. Steps of deforming the lateral beam of the T-spring to have same deflection in complementary rotation angle at both ends of the lateral beam of the T-spring ($-\theta_x$ at the left end and θ_x at the right end of the lateral beam). In step (a), a negative torque $-T_{x1}$ is applied at the left end of the lateral beam. In step (b), another torque (T_{x2}) is applied along the positive direction at the end of the right end of the lateral beam, while the amount of the torque is adjusted to T_{x1}'.

direction. Therefore, considering only the x-axis torsion, the stiffness of the coupling spring in the sensing mode is larger than the stiffness in the parasitic sensing mode.

The dimension of the sense-coupling spring also affects the amount of stiffness contributed by the semi-open frame. As the frame is made wider, its tensional and bending stiffness become smaller. As the T-spring's stiffness becomes comparable with the stiffness of the frame, the ratio between the amount of the elastic energy stored in the frame and the T-spring for a given displacement input increases. The effective stiffness of the BOG in the sense mode and the parasitic sense mode is the combination of the different stiffness provided from the T-coupling spring and the frame.

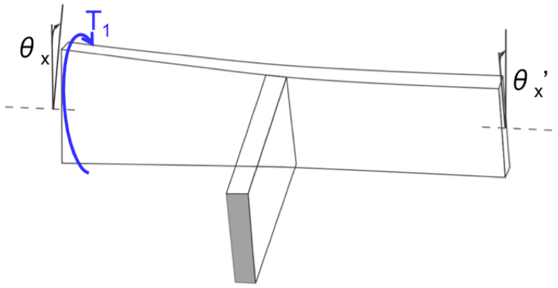

(a) X-axis torque -T_{x1} is applied at the left end of the lateral beam, causing a rotation angle of -θ_x at the left end and -θ_x' at the right end of the lateral beam ($\theta_x > \theta_x'$) due to torsional flexibility at the T joint.

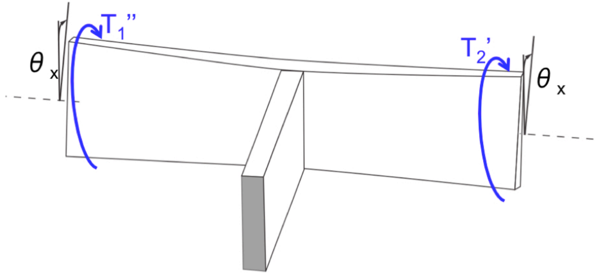

(b) Negative x-axis torque -T_{x2}' is applied at the right end of the lateral beam, and the torque at the left end of lateral beam is adjusted to T_{x1}'' to cause the same rotation angles of θ_x at both ends ($T_{x1}'' = T_{x2}'$).

Figure 4.11. Steps of deforming the lateral beam of the T-spring to have the same deflection angle θ_x at both ends of the lateral beam of the T-spring. In step (a), a negative torque -T_{x1} is applied at the left end of the lateral beam. In step (b), another x-axis torque -T_{x2}' is applied along the negative direction at the end of the right end of the lateral beam, while the torque at the left end is adjusted to T_{x1}''.

Due to the complexity of the gyro geometry, it is difficult to form accurate analytical equations to explain the relationship between the geometry of the T-spring and the resonance frequencies of the various modes. Thus, the relation is found using FEM analysis. The relations are found by changing each of the geometrical parameters, while keeping others constant. For the dimensions shown in Figure 4.7, the nominal dimensions are: b_a (width of the lateral beam) = 10µm, l_a (half of length of the lateral beam) = 100µm, l_b (length of the vertical beam) = 100µm, b_b (width of the vertical beam) = 10µm, and h (height) = 100µm. The rest of the geometry is shown later in Table 4.1.

Figures 4.12-4.15 show the relation between the lateral beam of the spring (l_a, b_a) and vertical beam (l_b, b_b) and the effect on the resonance frequencies. The graphs indicate that the geometry of the sense coupling springs changes not only the sense and parasitic sense mode but also driving and parasitic driving mode frequencies. However, the difference between the driving and the parasitic driving frequencies stays almost constant throughout the simulated range. The simulation results show that the separation between the sense and parasitic sense mode increases as the lengths of both of the vertical and horizontal beams (l_a and l_b) increase and as the widths of both of the horizontal and vertical beams (b_a and b_b) decrease.

4.4. Relationship between the Driving Mode Coupling, Linearity of the Driving Mode Motion, and the Position of the Sense-Coupling Beam

The motion of the two sets of driving masses are coupled by the deflection of semi-open frames. This deflection influences the operation of the BOG in several ways. First, when the amount of angular deflection increases, the orientation of the mass becomes increasingly nonparallel with respect to the comb-drive electrode. Due to the increased nonlinearity in the capacitive force, the driving range of the mass is decreased. In turn, the z-axis rotation on the masses affects the amount of coupling for the two sets of the drive masses. The minimum amount of mechanical coupling exists when there is no angular deflection of the frame. Without this coupling, the two sets of the masses can oscillate at two different frequencies. This frequency split creates challenges in control and reduces the scale factor. In addition, the position of the sense-coupling spring with respect to the frame affects the amount of angular deflection significantly, and as the deflection changes, the frequency difference between the driving and sensing modes and their respective parasitic modes changes.

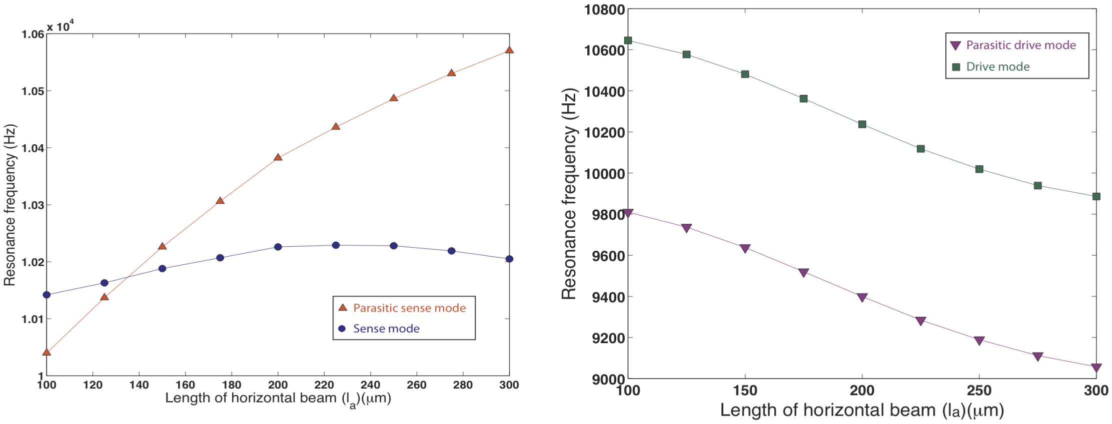

(a) Sensing mode and parasitic sensing mode

(b) Driving mode and parasitic driving mode

Figure 4.12. Relationship between the length of the lateral part of the sense coupling beam (l_a) and the sensing, parasitic sensing, driving, and parasitic driving mode frequencies. The rest of the geometry is set as l_b = 75μm, b_a = 10μm, b_b = 30μm, and h = 100μm.

The reaction diagram of the force and moment at the sense-coupling beam is shown in Figure 4.16. When the masses are driven with x-directional force $F_x(actuation)$, the T-spring provides an x-directional axial force $F_x(SC)$ and z-directional moment $M_z(SC)$ to the frame. The sense torsional beam provides z-axis moment $M_z(S)$. The forces and moments $F_x(SC)$, $M_z(SC)$, and $M_z(S)$ must sum such that the net forces and moments

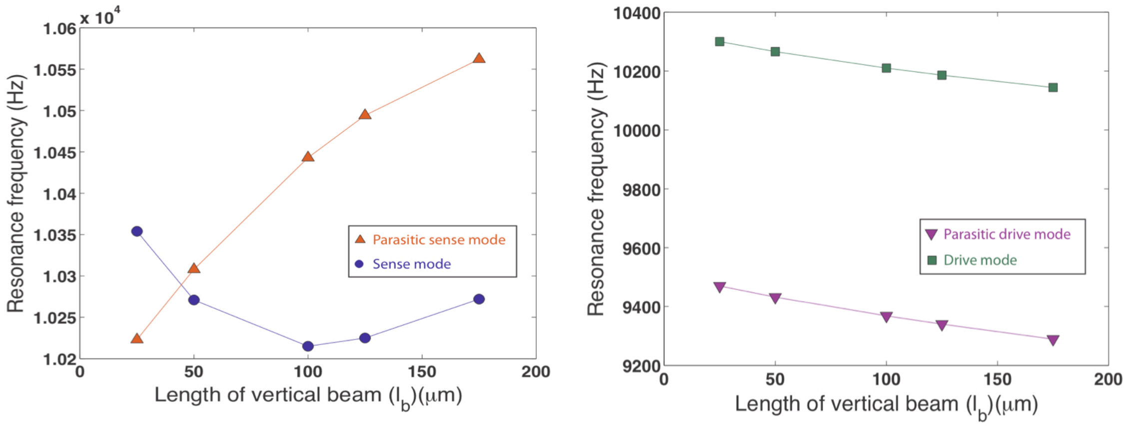

(a) Sensing and parasitic sensing mode (b) Driving and parasitic driving mode

Figure 4.13. Relation between the length of the vertical part of the sense coupling beam (l_b) and the sensing, parasitic sensing, driving, and parasitic driving mode frequencies. The rest of the geometry is set as l_a = 200μm, b_a = 10μm, b_b = 30μm, and h = 100μm.

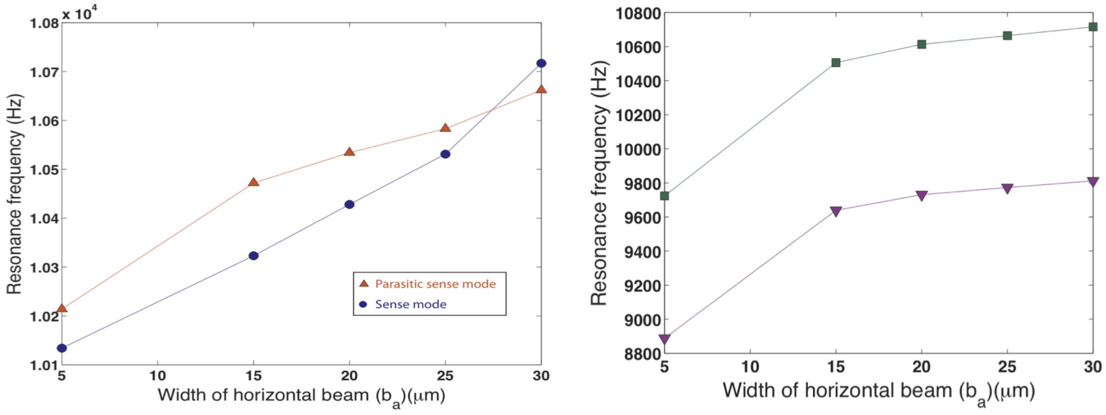

(a) Sensing and parasitic sensing mode (b) Driving and parasitic driving mode

Figure 4.14. Relationship between the width of the horizontal part of the sense-coupling beam (b_a) and the sensing, parasitic sensing, driving, and parasitic driving mode frequencies. The rest of the geometry is set as l_a = 200μm, l_b = 75μm, b_b = 30μm, and h = 100μm.

are zero. The reaction force and moment are also related by the deflection angle at the sense torsional beam and the deflection angle at the T-coupling spring.

The minimum angular deflection is achieved when the horizontal part of the sense-coupling spring is set parallel to the horizontal beam from the semi-open frame (y_d = 0). In this configuration, the reaction force from the electrostatic actuation is applied along mostly the axial direction of the lateral beam of the T-spring. Due to the large stiffness of the coupling spring along the axial direction, the sense coupling beam experiences negligible axial strain, and due to the angular relation between the deflection of the sense torsional beam and the sense coupling beam, the sense torsional beam also deforms by the minimal amount. When the lateral beam of the sense-coupling spring is placed at a higher position from the lateral beam of the semi-open frame along the y-axis ($y_d > 0$), the lateral beam experiences increasing z-axis moment. Since the coupling spring is made narrow and long to have good separation between the parasitic sense mode and the sense mode, the coupling spring is highly compliant to z-axis moment. As y_d increases, the amount of the moment at the end of the horizontal beam increases, increasing the T-spring deflection, resulting in larger angular deflection at the sense torsional beam.

Figure 4.17 shows the relationship between y_d and the ratio of vertical deflections found in the driving mass calculated with FEM simulation. The deflection ratio increases linearly with the increase in y_d.

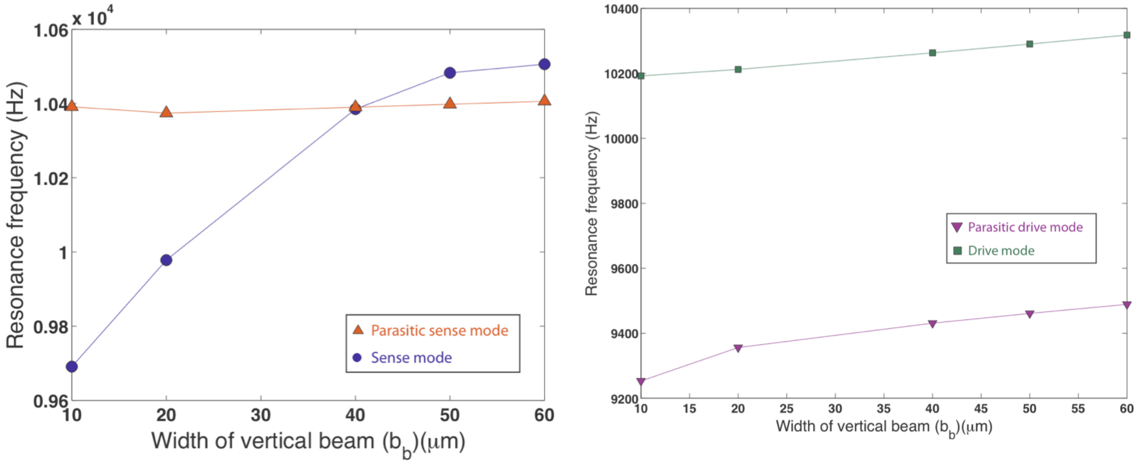

(a) Sensing and parasitic sensing mode (b) Driving and parasitic driving mode

Figure 4.15. Relation between the width of the horizontal part of the sense-coupling beam (b_b) and the sensing, parasitic sensing, driving, and parasitic driving mode frequencies. The rest of the geometry is set as $l_a = 200\mu m$, $l_b = 75\mu m$, $b_a = 10\mu m$, and $h = 100\mu m$.

Figures 4.18 and 4.19 show the relationship between y_d and the resonance frequencies of driving and parasitic driving modes and and sensing and parasitic sensing mode, respectively, again calculated using FEM simulation. The rest of the geometry parameters used in this simulation are found in Table 4.1. The figures indicate that the difference between the driving and the parasitic driving mode stay constant, whereas the difference between the parasitic sensing mode and the sensing mode increases with y_d.

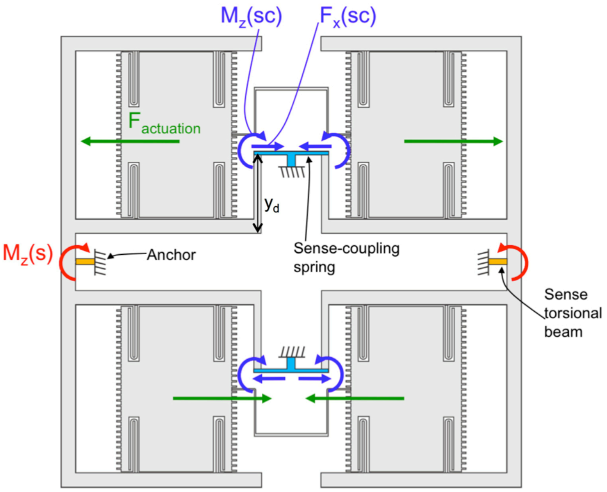

Figure 4.16. Reaction diagram of moment and forces in the driving mode.

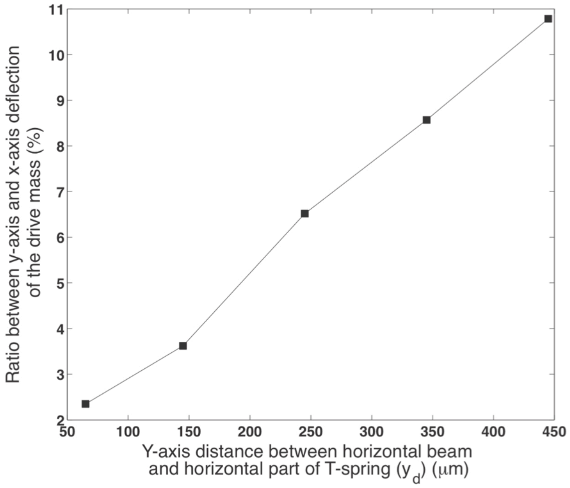

Figure 4.17. Relationship between the y-axis distance between the horizontal beam of the semi-open frame and the lateral beam of the T-spring and the ratio of the y-axis and x-axis deflections in the driving mode (y_d).

Based on the preceding analysis, the geometry of the BOG can be optimized using the FEM method to have a sufficient frequency difference between the sensing and parasitic sensing modes and also to have a small y-axis to x-axis deflection ratio for the driving mass in the driving mode.

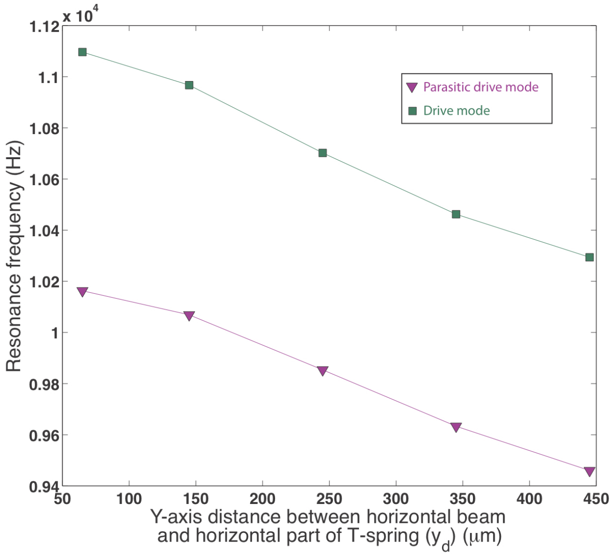

Figure 4.18. Driving and parasitic driving mode frequencies versus the y-axis distance between the horizontal beam of the semi-open frame and the lateral beam of the T-spring (y_d).

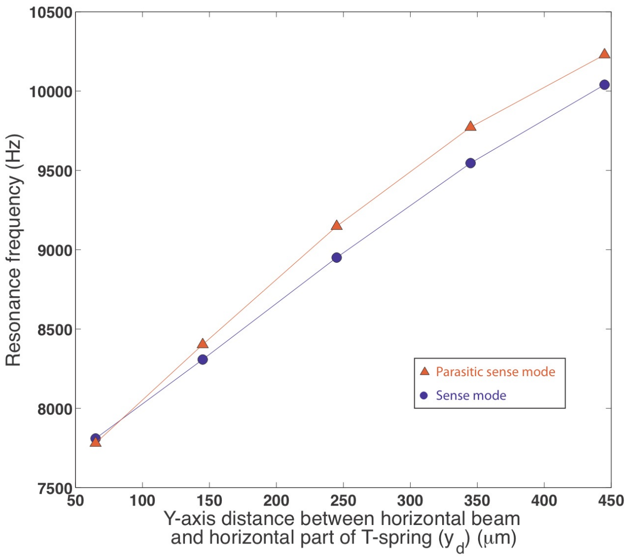

Figure 4.19. Sensing and parasitic sensing frequencies versus y-axis distance between the horizontal beam of the semi-open frame and the lateral beam of the T-spring (y_d).

4.5. Dimensions of the Fabricated BOG

The dimensions of the fabricated BOG (Figure 4.20) are summarized in Table 4.1. Table 4.2 summarizes mechanical and electrical design values of the BOG. The resonance frequency of a fabricated BOG is lower than the designed frequency due to lateral etching. The degree of change in the bending and torsional resonance frequencies due to a fixed amount of lateral etch depends on the original bending and torsional stiffnesses as well as the effective mass (*M*) and moment of inertia (*I*) of the geometry. The changes in the driving, parasitic driving, sensing, and parasitic sensing frequencies for the current geometry are found using FEM (Figure 4.21). The plot shows that the driving and parasitic driving frequency has higher sensitivity than the sense frequency. The larger sensitivity of driving mode to lateral etching is compensated by designing the driving mode frequency slightly higher than the sensing mode frequency.

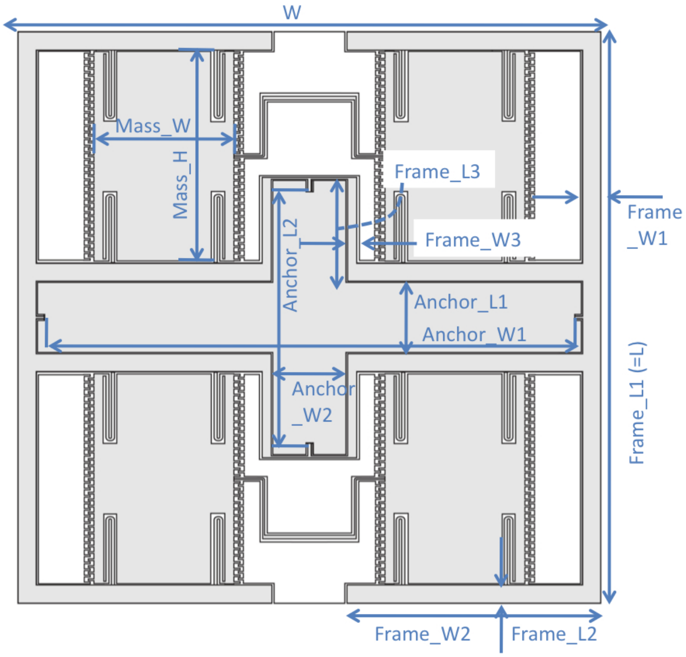

(a) Overall view

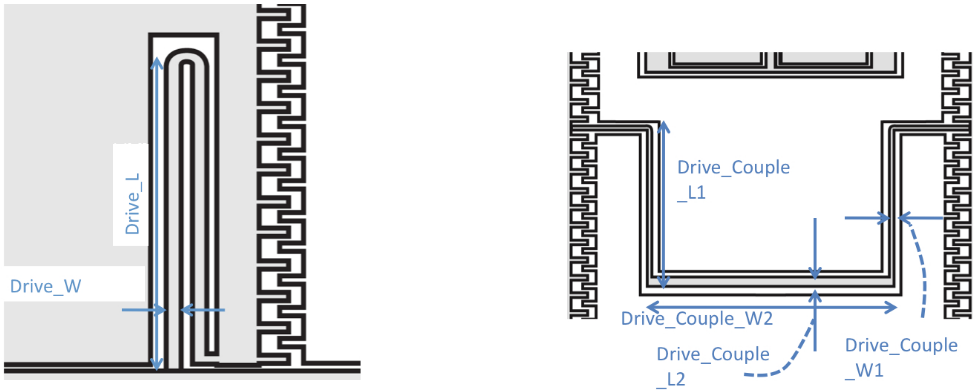

(b) Drive spring (c) Drive coupling spring

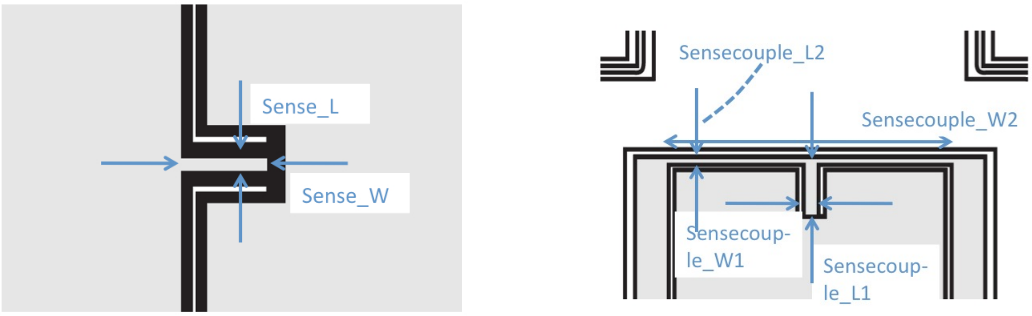

(d) Sense spring (e) Sense coupling spring

Figure 4.20. Dimensions of the first-generation Balanced Oscillating Gyroscope (BOG).

Table 4.1. Dimension of first-generation BOG

H (height)	100µm	Drivecouple_L1	316.5µm
W (width (x))	3052µm	Drivecouple_W1	7.5µm
L (length (y))	3000µm	Drivecouple_L1	317µm
Mass_W (drive mass width)	735µm	Drivecouple_W2	482µm
Mass_L (drive mass length)	1100µm	Drivecouple_L2	15µm
Frame_L1	1100µm	Sense_L (sense spring length)	18~20µm
Frame_W1	100µm	Sense_W (sense spring width)	40µm
Frame_L2	100µm	Sensecouple_L1	75µm
Frame_W2	1330µm	Sensecouple_W1	20µm
Frame_L3	546µm	Sensecouple_L2	10µm
Frame_W3	50µm	Sensecouple_W2	400µm
Anchor_L1	370µm	Nominal comb drive gap	2µm
Anchor_W1	2772µm	Sense electrode gap	2~3µm
Anchor_L2	1322µm	Electrode area (each quadrant)	116E4µm^2
Anchor_W2	390µm	Sense electrode gap	2~3µm
Drive_L	337µm		
Drive_W	12.5µm		

Table 4.2. Mechanical and electrical design values of the BOG, neglecting lateral etching from DRIE

Drive mass (each)	170µg	Parasitic drive mode 2 frequency	11841Hz
Sense moment of inertia with respect to the sense spring (x-axis)	2.2094E5 (µg•µm)	Parasitic drive mode 3 frequency	12404Hz
Drive mode frequency	10683Hz	Parasitic sense mode frequency	10737Hz
Sense mode frequency	10411Hz	Nominal driving capacitance (quadrant)	0.5pF
Parasitic drive mode 1 frequency	10085Hz	Nominal sense capacitance (quadrant)	3.4~5.4pF

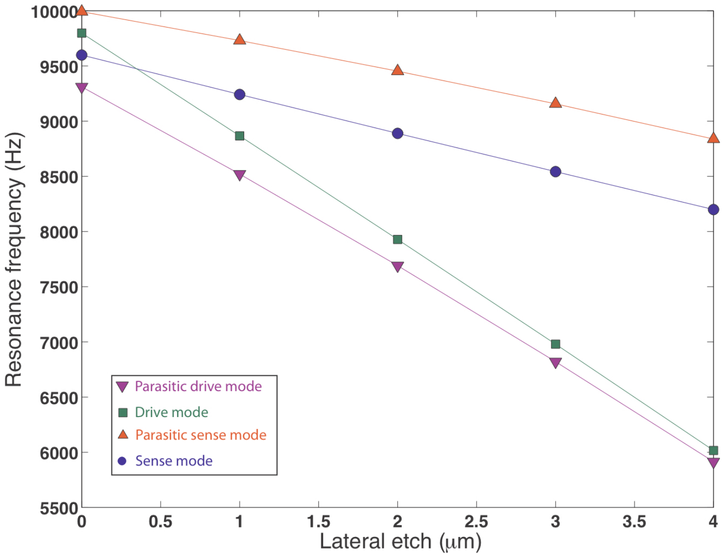

Figure 4.21. Change of the BOG's drive and sense mode frequencies increase in lateral etching.

4.6. Si-on-Glass (SOG) Process for the BOG

The Si-on-Glass (SOG) process is used to fabricate the BOG. The advantages of the SOG process over thin-film based processes are that it provides higher-*Q* materials, it can create large sensor masses, and it produces structures with lower residual stress. The advantages of the SOG process over the silicon-on-insulator (SOI) process are larger sensing area capacitance using the bottom electrodes, ability to control the gap between the mass and the bottom electrode, and lower parasitic capacitance due to glass substrate. The problems with a typical SOG process are footing and poor thermal-dissipation during the DRIE step needed to release the MEMS structures. The footing problem occurs when the bottom of through-etched silicon structures are attacked by SF_6 plasma molecules that are deflected by electric field developed by the trapped charges on the glass surface. One can avoid this problem by placing a conductive layer underneath every etching region. In the latest DRIE technology, the footing problem is avoided by releasing the charges by using low-frequency-modulated SF_6 plasma. Improving thermal dissipation is more challenging.

4.6.1. Si-on-Glass (SOG) Process Using Glass Thermal Dissipation Bumps

The thermal dissipation problem causes a drastic increase in the lateral etch rate during DRIE when the Si structures are close to being released. Early in the etch, the structures are connected at the bottom with the Si layer which keeps the etched areas below the temperature where the sidewall-protecting polymer starts to weaken. When the devices are nearly released, the heat conduction is poor, and the polymer is weakened. Because of this, Si structures are attacked by SF_6 plasma in the lateral directions. Due to glass's low thermal conductivity (1.1W/mK as opposed to 149W/mK for Si), it also contributes to the thermal dissipation problem. This problem occurs most significantly near springs or comb drives with a large length-to-width (L/W) ratio.

The process development discussed here is done with a STS DRIE machine at the Lurie Nanofabrication Facility (LNF). This machine clamps the process wafer using a mechanical clamp, and this machine provides only a high-frequency bias during the etching process. Although newer generation DRIE machines reduced the footing and heat conduction issues, it is believed that the process presented here is still useful, because it is more compatible with general DRIE machines. The SEM pictures of comb-drive electrodes suffering from thermal-dissipation problem are shown in Figure 4.22.

Other investigators have tried to overcome this problem by: 1) partially etching the front side of the Si wafer before bonding to glass, and etching or polishing the rest of the Si from the opposite side [19], or 2) recessing the glass wafer only after the DRIE step when the glass is etched for a long time to release the MEMS structure [56]. However,

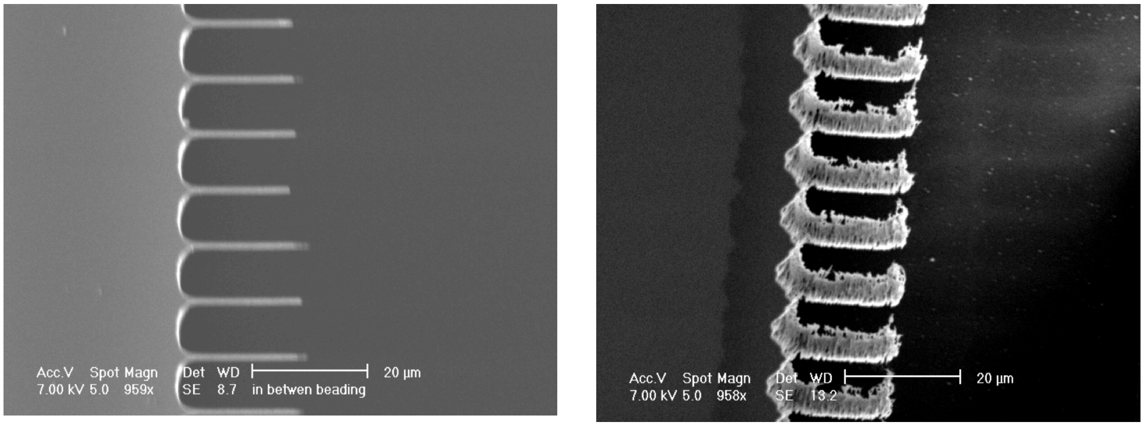

(a) Thinned down comb drive electrode (b) Curled comb drive electrodes

Figure 4.22. SEM photographs of comb drive electrodes damaged from over-heating during the typical SOG process.

the first method requires grinding and polishing step, which tends to increases cost and non-uniformity, and the second method is still prone to footing problems.

Two different methods are tried to reduce the thermal dissipation problem. In the first method, glass heat-dissipation bumps are patterned underneath the gyro mass. The Si mass and the glass substrate are bonded at these bumps, so etch heat is more easily dissipated through the bumps. The bumps are small enough to be etched using HF after the DRIE process. In the second method, Al heat dissipation layers are patterned underneath all etch regions. These Al dissipation layers are thick enough to physically contact the etched structures to the glass recess and can be easily removed by wet etching after the DRIE process.

Figure 4.23 shows the process steps of a SOG process which uses glass bumps as heat sinks. The process begins by defining 4µm-deep recessed areas on a borosilicate glass (Borofloat33) wafer from PlanOptik. The non-recessed areas form the glass bumps and the contact area for the vertical electrodes. A masking layer consisting of evaporated Cr with a thickness of 1000Å and AZ9260 with a thickness of 14µm is used to define the recessed areas. The glass substrate is etched in non-diluted HF (49%) to avoid variation in the etch-rate from the diluting step and to avoid the solution becoming saturated while processing multiple glass layers. After patterning the glass, a 1000Å-thick Al layer is patterned with the Cr-AZ9260 layer as a liftoff mask. After stripping the wet-etch mask, the glass substrate is blank etched in a BHF solution for 10 seconds to strip the Cr residue remaining on the surface of the glass. This stripping step is crucial for good quality anodic bonding.

Next, a 100μm-thick, double-side-polished, P-type (<0.005 ohm-cm), (100) Si wafer is cleaned using a Karl Suss CL200 megasonic wafer cleaner. The Si and the glass wafers are anodically bonded at 300°C with a bonding voltage of -500V for center-pin bonding and -1300V for full wafer bonding using a Karl Suss SB6E bonder. The

(a) A recess with a depth of 4μm defines the glass bumps and the contact area for the vertical comb electrodes. An Al layer with the thickness of 1000Å is deposited and patterned to form the shield layer

(b) A 100μm-thick Si wafer is anodically bonded to the glass wafer

(c) Si wafer is etched using DRIE

(d) DRIE etch mask and metal shield layer are removed

(e) Vertical comb (VC) electrodes are formed with local anodic bonding

(f) Movable structures are released from the bumps

Figure 4.23. SOG process using glass bumps and metal shields on the glass substrate.

bonding temperature is a critical process parameter, which affects the amount of curvature of the wafer. The coefficient of thermal expansion (CTE) of the glass for our process stays almost constant over the process temperature at 3.25ppm/°C [101]. On the other hand, the CTE of Si changes significantly with temperature [102] (Figure 4.24). Figure 4.25 shows the calculated normalized difference between Si and Borofloat33 wafers, accounting for the variation of CTE over a temperature range of 0 to 500°C. According to this analysis, a bonding temperature of 300°C will cause nearly zero overall deflection.

After bonding, the Si wafer is through-etched using DRIE with a mask of 4µm-thick SPR220-3.0. The patterns on the photoresist are exposed using I-beam lithography (λ: 365nm, beam power: 1000W) with a GCA AS200 Autostep. After the DRIE, the photoresist mask is dissolved in PRS2000, the Teflon residue on the sidewall of the patterned Si structures is removed using a Piranha (H_2SO_4:H_2O_2 = 1:1) solution, and the Al shield layer is completely removed using an Transene Type A etchant. Then, the wafer is rinsed in DI water for more than 10 minutes to rinse away the Al etchant. Without drying, the wafer is dipped in isopropyl alcohol (IPA) for more than 4 hours, and then the wafer is dried on a hot plate at 115°C.

Next, the wafer is flipped onto a clean dummy Si wafer, and is brought into the SB6E bonder where local anodic bonding is performed to form the vertical-comb (VC) electrodes. A more detailed discussion of the VC electrodes is provided in Appendix C. An anodic bonding voltage of -600V is used with a full electrical contact to the wafer surface. In this bonding step, suspended VC electrodes are pulled down on the glass substrate and form strong anodic bonds. Then, the glass bumps are etched away with non-diluted HF to release the structures. Note that the glass bumps have enough area to provide good thermal contact, but at the same time, individual bumps are small enough to be etched away in a relatively short time, limiting any damage to the anchors. The maximum size of the bumps used in this process is 30µm.

This fabrication method reduces the heating problem compared to the conventional SOG process. However, one of the issues found here is that the bottom surfaces of the Si

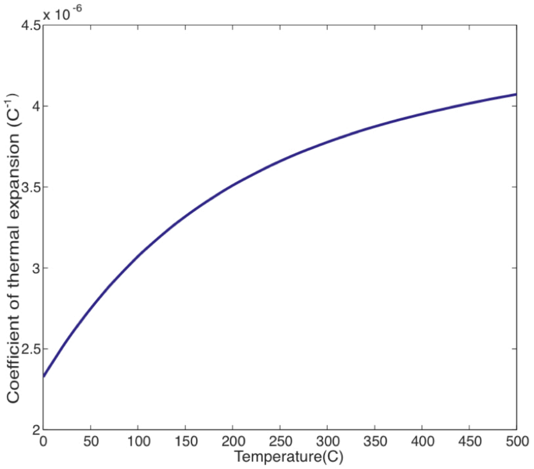

Figure 4.24. CTE of Si over a temperature of 0°C ~500°C [102].

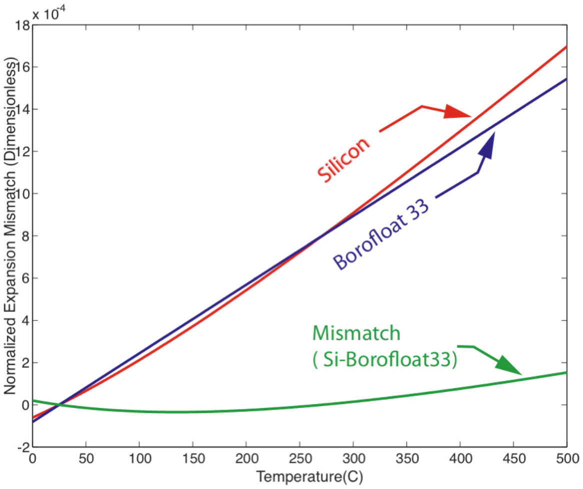

Figure 4.25. Normalized expansion mismatch between Si and Borofloat 33 with respect to bonding temperature (CTE of Borofloat33 and Si are found from [101] and [102], respectively).

structures are roughen by scattered SF_6 plasma, resulting in weak anodic bonds between the VC electrodes and the glass surface. Because of this, the VC electrodes cannot withstand the final HF etching step. Figure 4.26 is a backside photograph of the bonding plate of the VC electrodes after the bumps are etched, indicating significant undercut due to bonding plate with roughened bottom surface.

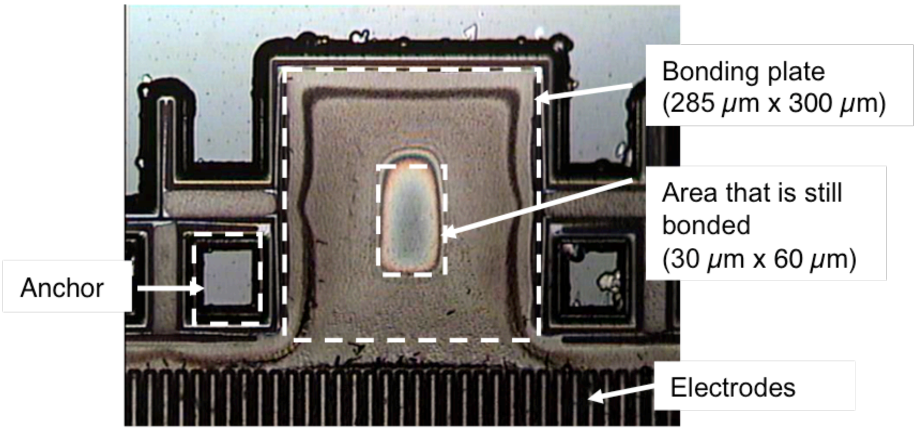

Figure 4.26. Bottom side photograph of vertical comb drive (VC) electrodes showing excessive amount of lateral etch due to rough bottom surface of Si substrate.

A modified process is introduced to solve the issue of the rough bottom surface. In the modified process, a metal shield layer is patterned on the bottom surface of the Si wafer instead of on the glass substrate, similar to the method that is demonstrated by Alper et al. [103] so that the shield layer can protect the bottom surface of the silicon during DRIE. The metal layer serves also as a thermal dissipation layer. The improved process flow is shown in Figure 4.27.

Using this method we are able to address the problems of footing and rough bottom surface, and we are able to solve the thermal gradient problem for most structures. This process, however, still cannot provide optimal heat dissipation at critical etch spots such as thin comb drives or springs, because of the footing problem. Figure 4.28 shows SEM photographs of the bottom sides of comb-drive electrodes which still suffered a considerable amount of lateral etching. This issue could be improved by using a several-microns-thick metal layer. Other issues of the process include excessive device area, primarily due to the VC electrodes, and the VC electrodes are significantly less sensitive than parallel-plate sensing. Therefore, it is desirable to develop a process that can prevent footing, provide better protection from overheating, and have parallel plate electrodes in the vertical direction. To accommodate these needs, the glass thermal dissipation bumps are replaced with a thick aluminum shield layer that can dissipate heat by contacting both the Si and the glass substrates.

(a) An Al layer with a thickness of 1000 Å is evaporated on top of a 100µm-thick Si substrate

(b) Recess with a depth of 4µm defines the glass bumps and the contact area for the vertical comb electrodes, and the glass substrate is anodically bonded to the silicon substrate

(c) Si substrate is through-etched using DRIE. The bottom surface is protected by the Al layer

(d) DRIE etch mask and metal shield layer are removed

(e) Vertical comb electrodes are formed with local anodic bonding

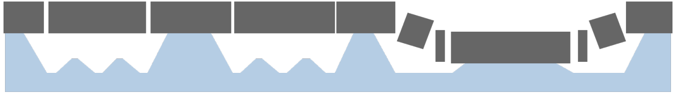

(f) Bumps are etched to release the moving structures

Figure 4.27. SOG process with glass bumps and metal protection layer on the bottom surface of Si wafer.

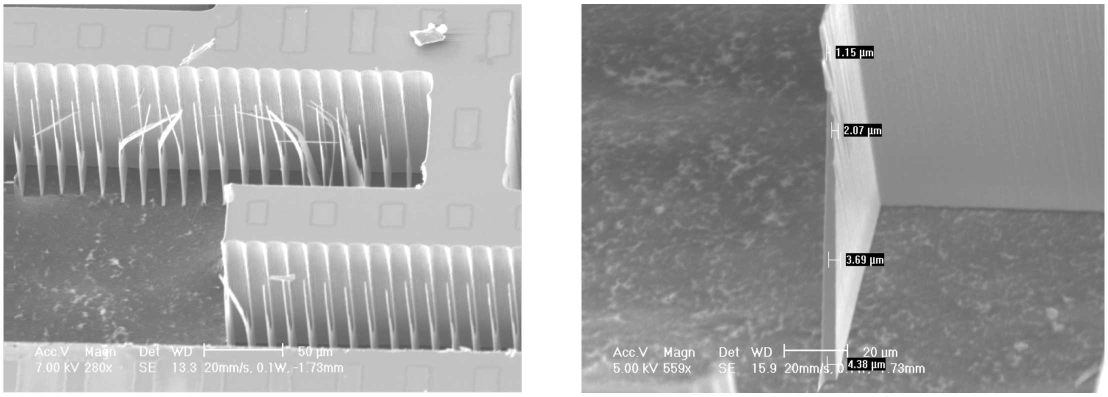

(a) Near the lateral comb drives (drawn width: 3µm)

(b) Near the lateral comb drives (drawn width: 6µm)

Figure 4.28. SEM photographs taken from the bottom of test device fabricated using the improved SOG process using glass bumps and metal protection layer on the bottom surface of Si wafer.

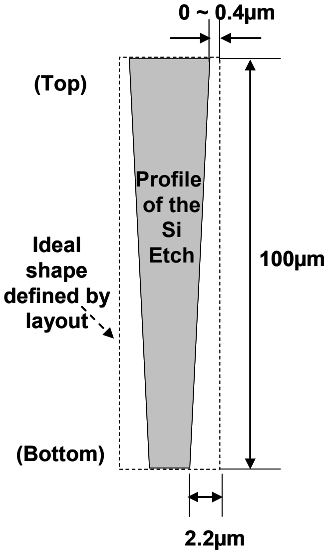

Figure 4.29. Etch profile of the improved SOG process using the glass bumps.

4.6.2. Si-on-Glass (SOG) Process Using Thick Aluminum Heat Sinks

Figure 4.30 shows the process steps of the SOG process with thick Al heat sinks. The process begins by recessing the glass substrate by 1-3µm using non-diluted HF. Then, a stack of Cr/Pt/Au with thicknesses of 50/250/250Å is patterned to form the bottom electrodes and the signal lines. On the top of a separate 100µm-thick Si wafer, Al is deposited to be slightly thicker (500~1500Å) than the recess and patterned to fit in the recesses on the glass wafer and form the shield layer and the heat sink. The Al layer is thin enough for the wafers to form good anodic bonds and also thick enough to have firm contact with the Si wafer. The Si wafer is then anodically bonded to the prepared glass substrate and etched using DRIE. The shield metal is wet etched to release the structures.

In this process, the heat sink can be placed directly below the spots where the Si is etched to achieve best thermal dissipation. In addition, this process can create parallel plate electrodes in the vertical direction to achieve better sensitivity and allow the resonance frequency to be tuned more easily. Figure 4.31 shows SEM photographs taken from the bottom and the side of a fabricated test device using the developed process, which demonstrate a good aspect ratio. Figure 4.32 shows the DRIE etching profile from this process, having a lateral etch of 0.9~1.4µm at the bottom of the 100µm-thick Si

(a) Recesses with a depth of 1-3µm are defined using wet etching

(b) Cr/Pt/Au: 50/250/250Å is evaporated and patterned to form the bottom electrodes and underlining signal lines

(c) On the 100µm-thick Si wafer, Al is deposited to be slightly thicker, by 500~1500Å, than the recess depth, and it is patterned to form the shield layer as well as heat sink

(d) Si and glass wafers are anodically bonded

(e) Si wafer is etched using DRIE

(f) Al layer is wet etched, and movable structures are released

Figure 4.30. SOG process using thick Al heat sink.

structure.

A comparison between SOG processes with glass-bumps and thick Al heat sinks is made in Table 4.3. Future work includes further improvement of the SOG process by fine-tuning the DRIE recipe to achieve an even better aspect ratio and a smaller feature size (<2µm) in order to reduce cross-axial stiffness. An SEM picture of the fabricated BOG with the direct heat-dissipation process is shown in Figure 4.33. The device has a size of 3mm (lateral) × 3mm (vertical) × 100µm (thickness), with a total mass of approximately 750µg.

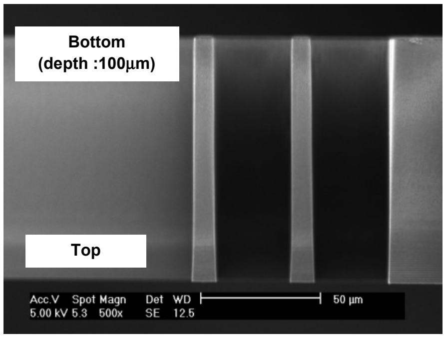

(a) Cross section of the parallel plate electrodes (drawn width: 9.5µm)

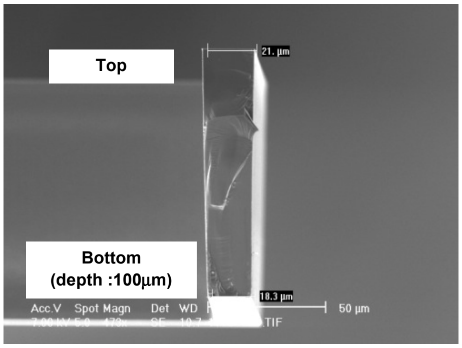

(b) Cross section of a spring (drawn width: 21µm)

Figure 4.31. Cross-sectional SEM photograph of fabricated samples made using SOG process with thick Al heat sink.

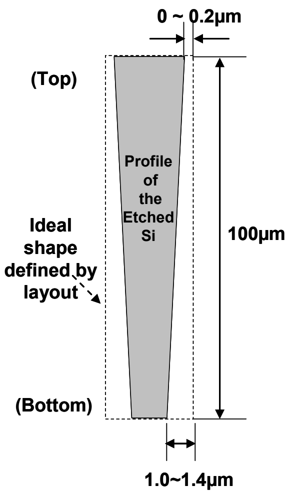

Figure 4.32. Etch profile of the SOG process using Al heat sink.

Table 4.3. Comparison of the etch profiles of developed SOG processes (based on 100µm-thick Si wafer; same DRIE etch recipe is used)

Process Flow	Figure 4.29	Figure 4.32
Material for the heat sink	Glass bumps	Al shield layer
Avg. lateral etch length: vertical etch depth	1:45	1: 87
Minimum feature size* (drawn)	5.5µm	3.5µm
Minimum gap size** (drawn)	<2µm	<2µm
Vertical Electrodes	VC electrodes	Parallel plate electrodes
* Minimal feature size is defined as the width of a layout that will have the width of 1µm at the bottom of the Si substrate, so that the structure can possess enough strength ** Minimum drawn gap size is limited by lithography		

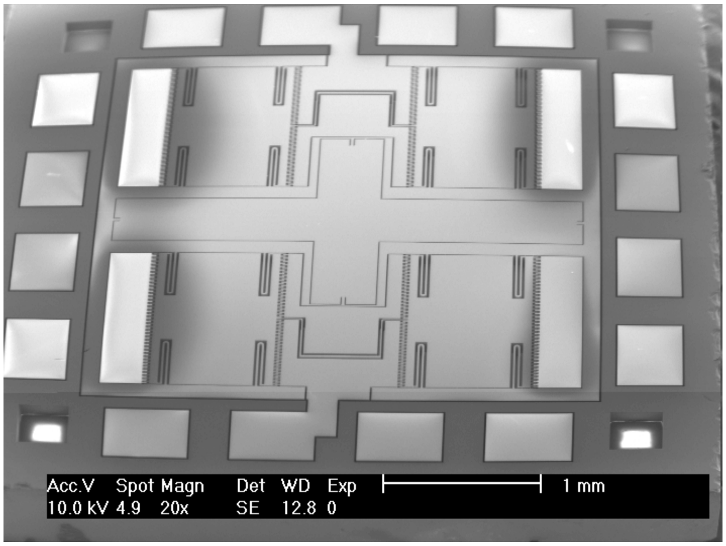

Figure 4.33. SEM picture of Balanced Oscillating Gyroscope (BOG) made with SOG process using Al heat sink.

4.7. Resonance Characteristics of the Balanced Oscillating Gyroscope (BOG)

The resonance characteristics of the Balanced Oscillating Gyroscope (BOG) with Al heat sink are tested in a Lakeshore FWP-6 vacuum probe station at a pressure of <5mTorr. The temperature is left uncontrolled (~300K). A transimpedance amplifier with JFET OPAMP (MC33184) with a feedback resistance of 10MΩ is used. The gain-phase measurement is done using an HP4194A.

The gyro is actuated using one of the comb electrodes at the outer boundary of one of the driving masses. By actuating from this electrode, all four modes along the planar direction can occur due to strong mechanical coupling. Due to cross-axis stiffness, both modes along the z-axes can also occur. Figure 4.34 shows the measured resonance peaks. The mode located at the lowest frequency is the in-phase parasitic driving mode. In this mode, two pairs of masses connected by the drive coupling springs move in the opposite directions. Very little elastic energy is stored in either the drive-coupling springs or the semi-open frames. The next mode is the driving mode, where the masses connected with the drive coupling beams are oscillating out-of-phase. In this mode, elastic energy is stored in the drive coupling spring, but little energy is stored in the semi-open frame. The third mode is the sense mode. In this mode, the sense torsional beam and the sense-coupling beam are primarily responsible for the overall stiffness. The drive-coupling spring provides minor contribution to the overall stiffness of the structure in this mode. The fourth mode is the in-phase parasitic driving mode, where the two pairs of connected masses move in the same phase. The fifth mode is the second out-of-phase parasitic driving mode. In this mode, the masses that are connected with the drive-coupling beams move with the same phase, so the lateral stiffness of the semi-open frame contributes to the overall stiffness. Although this is a balanced mode with a large *Q* (>50,000), we cannot use this mode in practice, because no Coriolis force can be developed under y-axis rotation. The sixth mode is the parasitic sensing mode, where two frames tilt in the same phase along the sense torsion beam.

From the tested device, the driving mode is found at ~8500Hz and the sensing mode is found at ~8700Hz. The driving mode is separated from the nearest spurious mode by about 300Hz. The sensing mode is separated from the nearest spurious mode by about 200Hz. The *Q* of the driving and sensing modes are measured to be about 50,000 and 20,000, respectively.

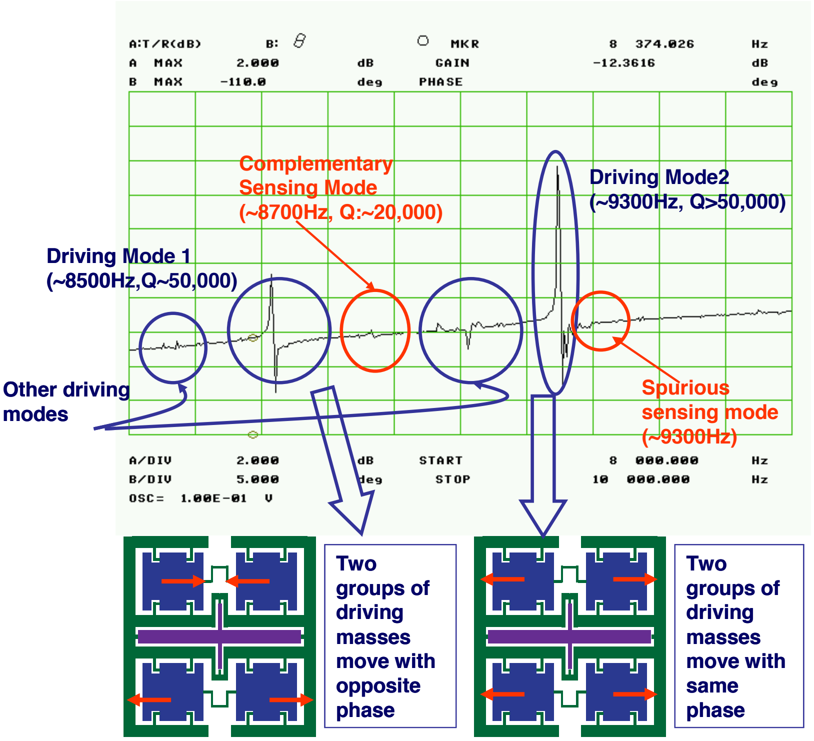

Figure 4.34. Gain plot of the BOG measured from 8,000Hz to 10,000Hz at room temperature (300K) and pressure under 5mTorr.

The driving and the sensing mode frequencies can be brought close to each other using the electronic tuning method down to below their 3dB bandwidths (Figure 4.35) by applying a DC offset to the non-inverting input port of the transimpedance amplifier connected to the bottom electrode. The *Q* of the sense mode is found to decrease to 7,422 due to cross-axial coupling. The minimum frequency difference between the driving and sensing modes of the current gyro is limited by cross-axial stiffness, and it is necessary to include bottom electrodes dedicated for balancing cross-axial stiffness in the next generation gyro.

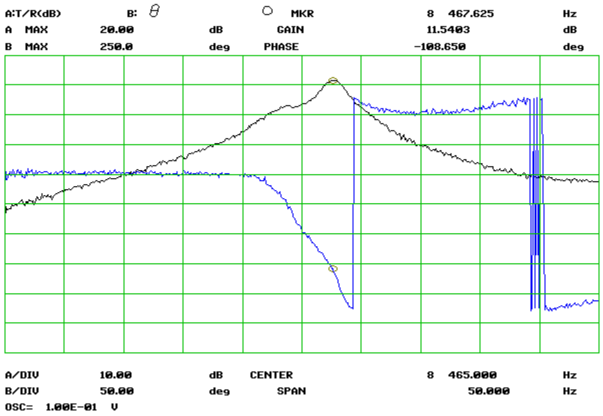

(a) Frequency separation of ~5Hz between driving and sensing modes (nearly matched), body bias: 7.46V, bottom electrode voltage: 0V

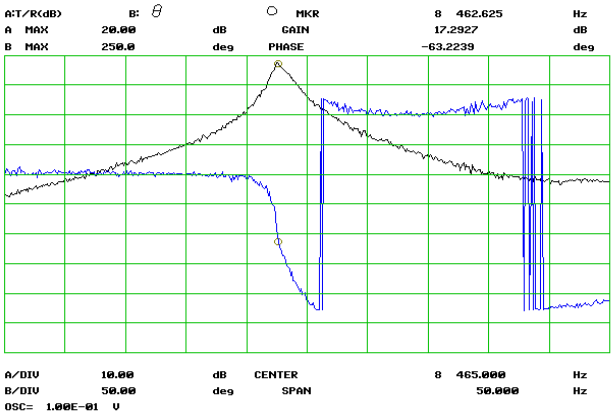

(b) Frequency separation below the 3dB bandwidth (very closely matched), body bias: 7.56V, bottom electrode voltage: 0V

Figure 4.35. (a) Slightly mismatched matched (~5Hz difference) and (b) closely matched (within 3dB) resonance frequencies of the BOG.

4.8. Temperature Dependency of Mode Frequency and *Q*

The frequencies and the *Q* of the driving and sensing mode frequencies are measured over a temperature from -50 to 75°C, under a pressure of <1mTorr (Figure 4.36). Both the driving and sensing mode frequencies drop as the temperature increases with thermal coefficients of frequency (TC_F) of -14.6ppm/K and -9.1ppm/K, respectively.

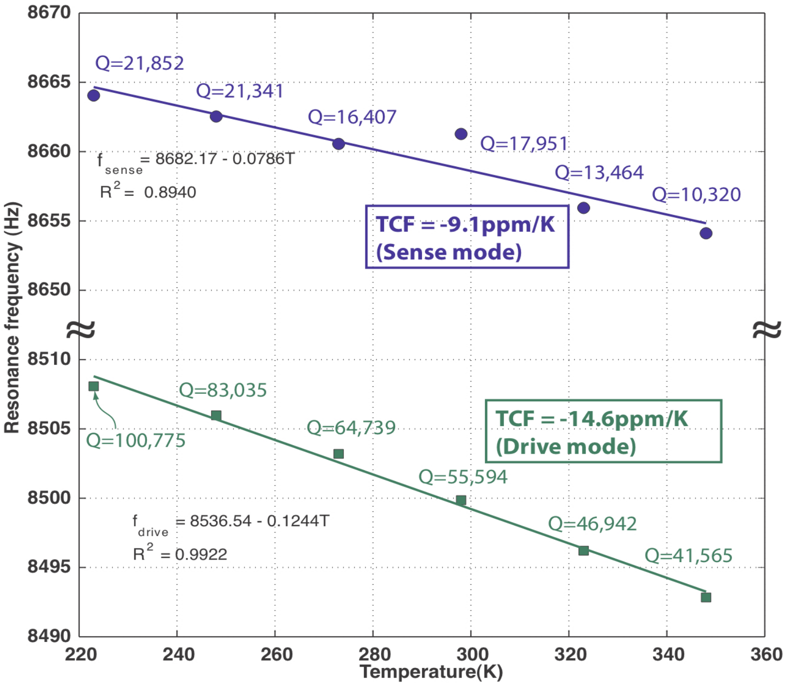

Figure 4.36. Change of the BOG's resonance frequency and the *Q* over the temperature range of 233K to 348K, measured at <1mTorr range.

The temperature sensitivity of the BOG is approximately a half of the TC_F values reported for Si micro-resonators on a SOI substrate [104, 105]. It is believed that the smaller TC_F is contributed by thermoresidual stress from the mismatch between expansion coefficients of Si and glass. The *Q* for the driving and sensing modes decreases with an average rate of -6000ppm/K and -5000ppm/K. The negative slope of *Q* with temperature indicates thermoelastic damping (TED) is one of the dominant mechanism of the BOG. In the TED mechanism, the amount of the temperature gradient generated in an oscillating beam from adiabatic expansion and compression is proportional to the ambient temperature, resulting in the increase in damping force with increase in ambient temperature [106].

4.9. Pressure Dependency of Mode Frequency and *Q*

The *Q* of the driving and the sensing modes of the BOG are characterized from a pressure of 0.5 to 100mTorr at 293K (Figure 4.37).

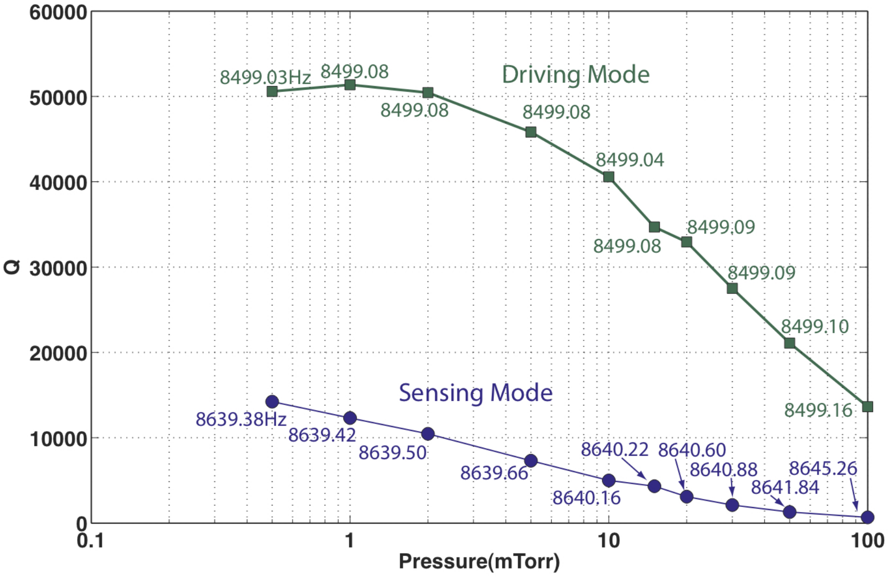

Figure 4.37. Change of quality factor (*Q*) of the BOG from pressure of 0.5mTorr to 100mTorr.

The *Q* of the sensor has a maximum value of 50,000 at <2mTorr, which is highly likely limited by TED. Above that pressure, the driving *Q* is increasingly affected by air damping. On the other hand, the sensing *Q* did not show any peak, which indicates that the influence of air damping is more significant. The difference in the pressure sensitivity of the *Q* is believed to be from the difference in the electrode configuration. In a comb-drive electrode, there is shorter path for air molecules to squeeze out than the parallel electrode during actuation.

4.10. First-generation Readout-and-Control Circuitry

The 1^{st}-generation interface circuitry consists of an analog self-oscillation block, gain control block, instrument amplifier block, and demodulation block. The architecture of the circuit is shown in Figure 4.38. Note that this version of circuitry is built to mainly confirm the functionality of the prototype BOG. In the future, the system will be improved with a better configuration for the amplitude controller block and will include a quadrature cancellation block. This version of the BOG sensor does not have balancing electrodes to compensate for cross-axial stiffness difference, nor does it have force-rebalancing electrodes for quadrature error and closed-loop rate operation.

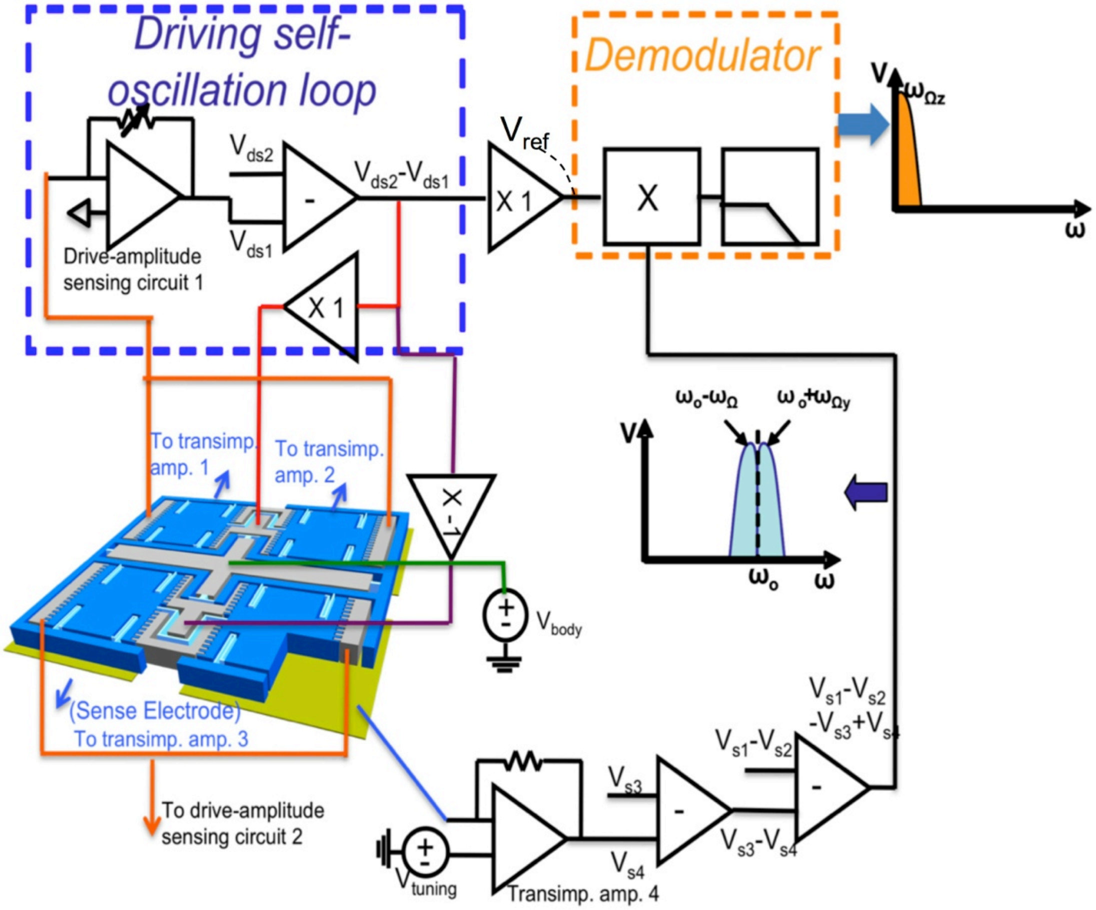

Figure 4.38. Architecture of the first-generation circuitry.

4.10.1. Self-Oscillation Block

The self-oscillation block consists of a transimpedance amplifier (TIA) and a buffer. The circuitry uses a principle that at the resonance frequency, the phase of displacement lags the phase of the actuation force by 90°. If the rest of the circuitry makes the overall loop phase of 360° and provides a loop gain of larger than 1, the amplitude of the vibration starts building up. The amplitude is regulated with an automatic gain controller (AGC) block at certain amplitude range (typically several microns for tuning-fork gyros) to avoid large nonlinearity. When a TIA is used, the output of the signal has the same phase as the velocity of oscillation. In the resonance mode, the actuation signal has the same phase as the velocity. Therefore, in resonance, the driving signal and the output signal from TIA have the same phase.

4.10.2. Automatic-Gain Controller (AGC) Block

The automatic gain controller (AGC) consists of a half-wave rectifier, a comparator, and a low-pass filter [107]. This block rectifies the measured displacement signal and averages it to calculate a near-DC signal that is proportional to the vibration amplitude. The amplitude signal is then compared with a DC set point. The output from the comparator is low-pass filtered. The output of the low-pass filter is connected to the gate of a N-type MOSFET (NXP BSS83), which is connected in series with 10kΩ linearization resistor. The MOSFET and resistor are connected in parallel with the 10MΩ feedback resistor at the frontend TIA for the driving-amplitude-sensing electrode. The gain of the TIA is controlled by changing the gate bias of a discrete NMOS chip, operating in the linear region. The threshold voltage of this NMOS chip is controlled with the substrate bias.

In this version of circuitry, the output signal from the TIA connected to the driving sensing electrode is currently used as the reference signal for the demodulation block. The reference signal contains low-frequency noise, which is generated from rectification and low-pass filter in the AGC, and the noise limits the accuracy of the sensor. This problem can be solved by separating the reference-signal generator from the self-oscillation block.

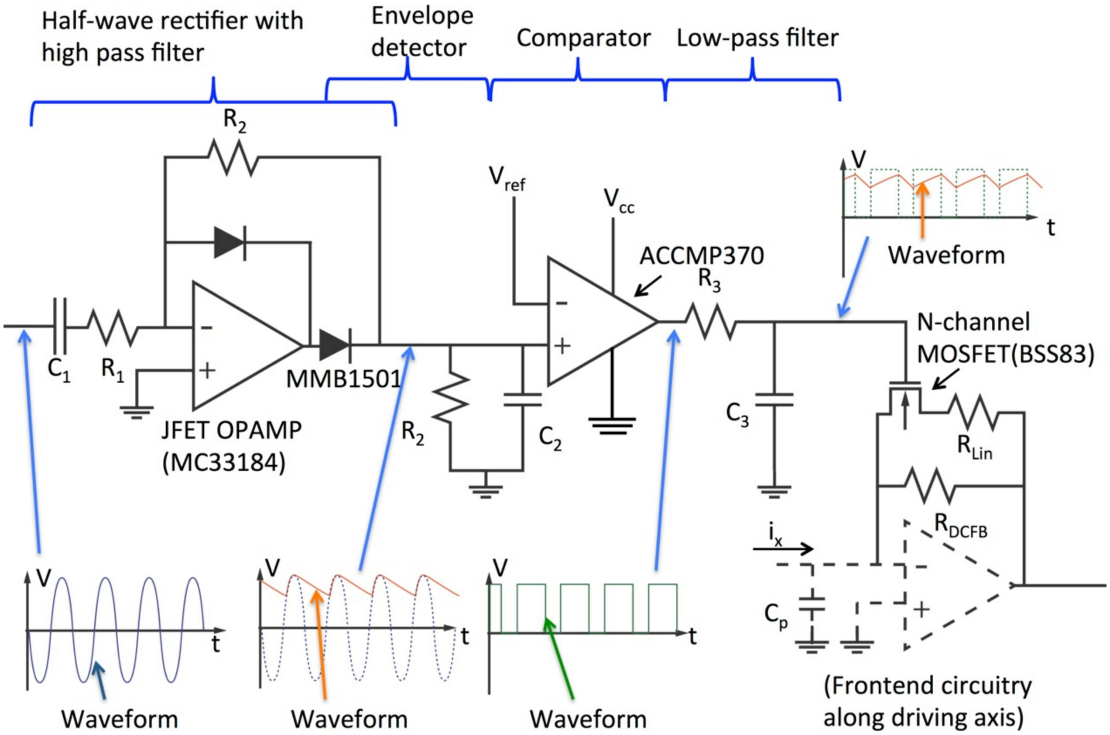

Figure 4.39. Automatic gain controller (AGC) circuitry. The circuit consists of half-wave detector, comparator, and low-pass filter.

4.10.3. Instrumentation Amplifier Block

The instrumentation amplifier block combines the signal outputs of the TIA connected to each quadrant of the sensor to provide differential cancellation of signals due to capacitive feedthroughs and in-phase oscillation.

4.10.4. Demodulation Block

The demodulation block consists of a manual phase-shifter and a 2nd-order Butterworth filter. The manual phase shifter block can adjust the reference voltage by 0° or 90°, depending on the frequency separation between the driving and sensing modes. When the driving and sensing modes are matched, the phase relationship between the reference voltage and the TIA connected to the sense electrode is 0°. This is because the reference signal is in phase with the velocity of driving motion, the Coriolis force is in phase with the driving velocity, and the output signal from the TIA connected to the sense electrode is in phase with the Coriolis force, because the sensing mode is occurred. When unmatched, the output from the TIA to the bottom electrode has 90° separation from the Coriolis force, because the sensing mode is not occurred. It is difficult to achieve exact phase using manual phase shifter, so this unit will be changed in the future. The parameters of circuit blocks in the first-generation circuitry are provided in Table 4.4.

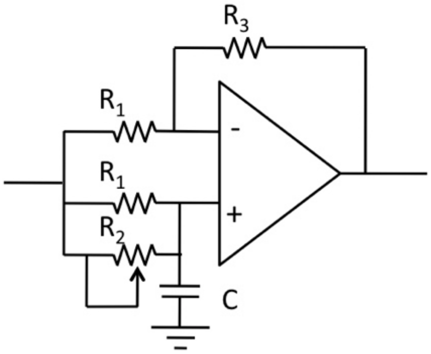

Figure 4.40. Manual phase shifter.

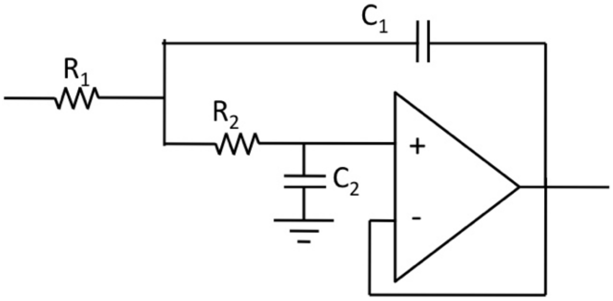

Figure 4.41. Second-order Butterworth low-pass filter.

4.11. Testing Setup

For testing, the BOG and front-end interface circuitry are mounted on an Ideal

Aerospace® 500 rotation table. The BOG chip is wire-bonded to a ceramic DIP package, and the package is mounted vertically to align the rate table with the measuring axis of the BOG. The package is connected to TIA built on a protoboard. A metal bell jar is set on the top of the rotation stage to allow testing the device under vacuum. The signal lines are fed out through slip rings. The control circuitry is located on a separate protoboard outside the rotation table. The system is pumped down to a high vacuum level of <5mTorr, read by a commercial Pirani gauge. The temperature of the sensor is kept uncontrolled.

Table 4.4. Parameters of readout-and-control circuitry

Circuitry Block	Property
Frontend	R_{dcfb}: 10MΩ, R_{lin}: 10kΩ
Auto-gain Controller (AGC)	Half-wave detector: - High-pass 3dB frequency: 700Hz - Low pass filter's 3dB frequency1: 1000Hz. - Gain: -10 Low-Pass filter 3dB frequency: <10
Variable phase shifter	Phase shift: >90°
Sensing demodulator	Butterworth filter 3dB frequency: <50Hz

4.12. Scale Factor Measurement

Due to cross axis stiffness, the minimum mode separation of the sensor is about 4Hz. The sensor is kept at a pressure below 5mTorr, and the scale factor of this gyro under DC rotation is tested from a rate of -100 to 100°/sec (Figure 4.42). The measured scale factor was 5.65mV/°/sec with a linearity (R^2) of 0.999. The scale factor of the current device is limited by quadrature error, which saturates the output of the TIA. The quadrature error can be reduced by aligning the stiffness axis electronically if alignment electrodes are added to the design. The methods for reducing the quadrature error will be discussed later.

4.13. Noise Equivalent Rotation Rate

The power spectrum of the BOG with a resonance frequency gap of 5Hz between the driving and the sensing modes is measured with the rotation table rotating sinusoidally with an amplitude of 10°/s and a frequency of 5Hz. Figure 4.43 shows the power spectrum plot of the output signal of the gyro, when it is tested under 5Hz and 10°/s peak-to-peak rotational signal. The low pass filter is set to be about 20Hz.

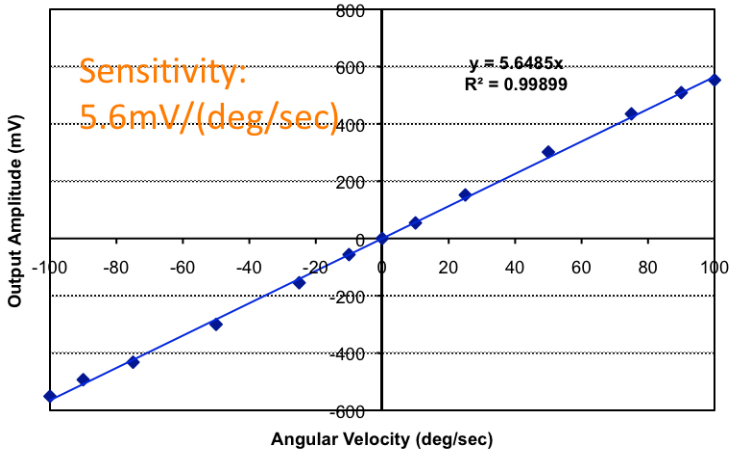

Figure 4.42. Voltage output of the BOG over -100°/s to 100°/s at pressure below 5mTorr.

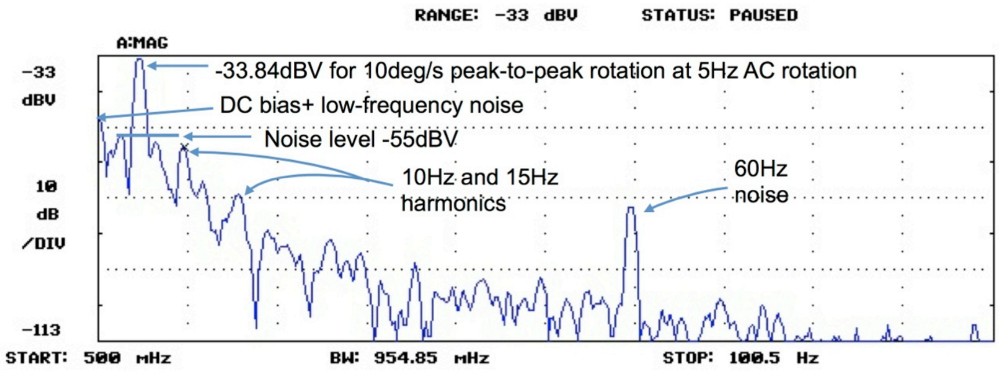

Figure 4.43. Power spectrum density of the BOG measured using first-generation interface circuitry. The device is tested under a rotation rate of 10°/s peak-to-peak at 5Hz. Under 10°/s peak-to-peak AC rotation at 5Hz, the signal output is -33.84dBV. The base noise level is -55dBV at 3Hz. The noise equivalent rotational rate (ARW) is calculated as 0.44°/sec/√Hz.

The output signal of this gyro has peak amplitude of -33.84dBV, and the noise level is at -55dBV. Harmonics of input rotation frequencies are found at 10Hz and 15Hz. These harmonics are caused from nonlinearity in capacitance measurement from parallel-plate electrodes and low-frequency noise in the reference signal. Based on the signal to noise ratio from this plot, the angle random walk (ARW) of this gyro is calculated as 0.44°/sec/√Hz.

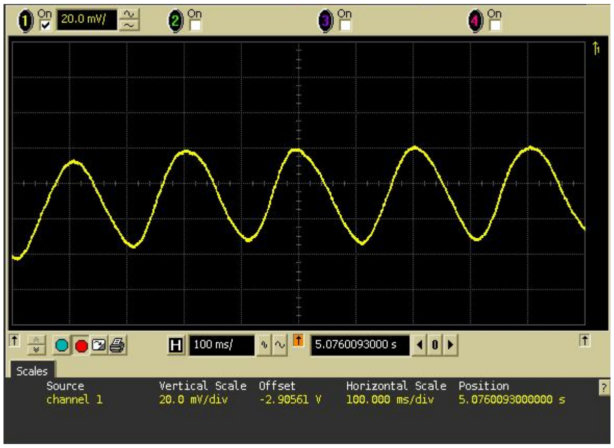

```
Source       Vertical Scale  Offset       Horizontal Scale  Position
channel 1    20.0 mV/div     -2.90561 V   100.000 ms/div    5.0760093000000 s
```

Figure 4.44. Output signal under a sinusoidal rotation of 10°/s at 5Hz.

4.14. Future Development

4.14.1. Cancellation of Quadrature Error

One of the performance limiting factors of the current gyroscope is quadrature error. The quadrature error is created from non-zero cross-axial stiffness. The cross-axial stiffness of the gyro is generated from mismatch between the principal stiffness axes and the sensor axes. The sources of mismatch in the axes include asymmetric DRIE profile, device bowing, and levitation force in the comb-drive electrode [108].

In the Si-on-glass (SOG) process, device is bowed due to mismatch in the TCE of Si and glass. Figures 4.45 (a) and (b) show the SEM picture of the BOG and the vertical profile of the BOG, measured using a Zygo Newview5000 optical interferometer, respectively.

The SEM picture shows the locations of driving mass, driving electrode, driving sensing electrode, driving spring, and anchor. The optical profile indicates that the gyro is bent upward by 0.4μm at the top edge of the device. The electrode is anchored on the glass substrate, so it is not bent upward in the same way as the suspended gyro mass. The principal stiffness axes are located in parallel to the mass. Due to the bowing, the principal stiffness axes are misaligned from the sensor axes (Figure 4.46).

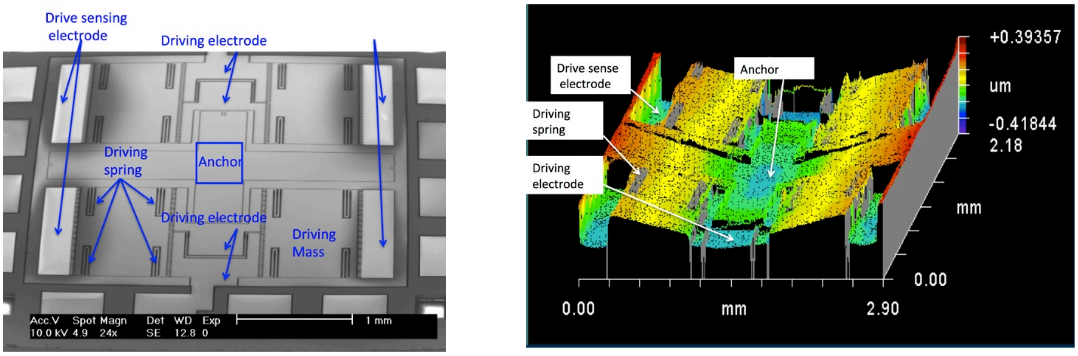

(a) SEM picture (b) Vertical profile

Figure 4.45. SEM picture and vertical profile of BOG measured using Zygo. The Zygo plot indicates that the edge of the BOG is bent up by 0.4μm due to mismatch in thermal coefficient of expansion (TCE) of Si and glass.

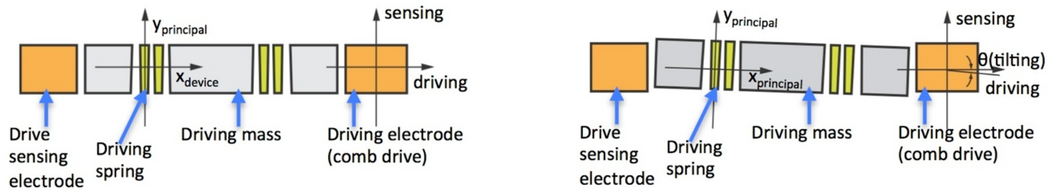

(a) When gyro spring and electrodes are aligned

(b) When gyro spring and electrodes are mismatched by θ

Figure 4.46. Relationship between sensor axes and principal stiffness axes: (a) spring and electrodes are aligned, and sensor and stiffness axes are aligned and (b) spring and electrodes are separated by angle θ.

The cross-axial stiffness along the sensor axis also prevents mode matching. When the damping of the system is small ($Q > 10{,}000$), the motion equation of a simple gyro model, having effective mass M along driving and sense axes and effective stiffnesses k_{11}, k_{22}, k_{12}, and k_{21} along the driving, sensing, and cross-axial directions, respectively, become:

$$\begin{bmatrix} M & 0 \\ 0 & M \end{bmatrix}\begin{bmatrix} \ddot{x} \\ \ddot{y} \end{bmatrix}+\begin{bmatrix} k_{11} & k_{12} \\ k_{21} & k_{22} \end{bmatrix}=\begin{bmatrix} 0 \\ 0 \end{bmatrix} \qquad \text{(Equation 4.4)}$$

The resonance frequencies can be found by inserting Equations 4.5 and 4.6 into Equation 4.4.

$$x = X\exp(j\omega t) \qquad \text{(Equation 4.5)}$$

$$y = Y\exp(j\omega t) \qquad \text{(Equation 4.6)}$$

The driving and sensing mode frequencies ω_1 and ω_2 are calculated as:

$$\omega_1 = \sqrt{\frac{M_1k_{22} + M_2k_{11} - \sqrt{\left(M_1k_{22} - M_2k_{11}\right)^2 + 4M_1M_2k_{12}^2}}{2M_1M_2}} \qquad \text{(Equation 4.7)}$$

$$\omega_2 = \sqrt{\frac{M_1k_{22} + M_2k_{11} + \sqrt{\left(M_1k_{22} - M_2k_{11}\right)^2 + 4M_1M_2k_{12}^2}}{2M_1M_2}} \qquad \text{(Equation 4.8)}$$

The square-root radicands of ω_1 and ω_2 are different by:

$$\frac{\sqrt{\left(M_1k_{22} - M_2k_{11}\right)^2 + 4M_1M_2k_{12}^2}}{M_1M_2} \qquad \text{(Equation 4.9)}$$

The necessary conditions to match the ω_1 and ω_2 are:

$$M_1k_{22} - M_2k_{11} = 0 \qquad \text{(Equation 4.10)}$$

$$k_{12} = 0 \qquad \text{(Equation 4.11)}$$

This relationship shows that k_{12} (=k_{21}) has to be reduced to zero in order to match the frequencies of the two modes. In order to cancel the cross-axial stiffness, it is necessary to include an electrode that can provide a force along the sensing axis that is proportional to the displacement along the driving axis. This can be done using bottom electrodes that partially overlap the drive mass, as shown in Figure 4.48.

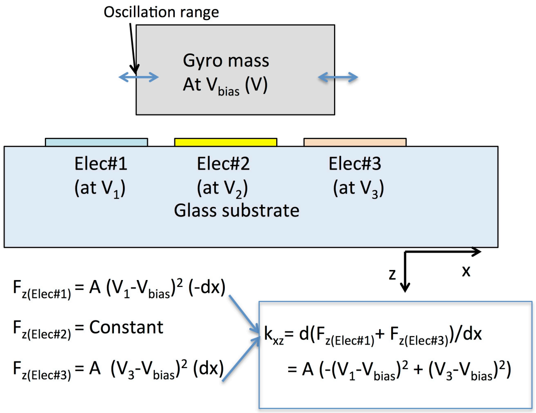

Figure 4.47. Structure of partially overlapping electrodes. The vertical force depends linearly on x-axis displacement, so the cross-axis stiffness of both polarities can be adjusted using V_1 and V_3.

4.14.2. Improvement of Interface Circuitry

In the current interface circuitry, the reference signal contains low-frequency noise that is created from the automatic gain controller (AGC) (Figure 4.39). The behavior of the current circuitry is simulated using Simulink. Figure 4.49 shows a Simulink model that describes the dynamics of a gyro and the architecture of the current interface circuitry. The displacement along the x- and y- axes are written as x and y, respectively. The effective masses along the two axes are set to be the same. The dynamics along the two axes are described using resonance frequencies (ω_{11}, ω_{22}), damping time constants (τ_{11}, τ_{22}), cross-axial frequency (ω_{12}, ω_{21}), and the Coriolis force ($2\Omega\dot{x}$, $2\Omega\dot{y}$). The motion along the driving and sensing axes are coupled by the Coriolis force and force from cross-axial stiffness. The cross-axial stiffness introduces quadrature error, which has 90° separation from displacement from the Coriolis force. The purpose of this simulation is to demonstrate the instability in bias from the fluctuation in the reference signal. In the simulation, driving and sense frequencies are set to 10,000Hz and 10,010Hz, and the cross-coupling stiffness is set to be the 0.1% of the in-axial stiffness. The Q of both modes are set to 1,000 to reduce the time for reaching to a steady state. The nominal Q value is found to introduce negligible difference in the amount of the amplitude fluctuation in the reference signal v_{ref}.

Figure 4.49 shows the normalized waveforms of $\dot{x}$ (from TIA along driving axis), $\dot{y}$ (from TIA along sense axis), reference voltage (v_{ref}), $\dot{y} \times v_{ref}$, and the output from 2nd-order Butterworth filter (v_{out}) with a cutoff frequency of 50Hz. From these signals, we find that $\dot{x}$ (normalized) and $\dot{y}$ (normalized) have much more stable amplitude than the v_{ref}. This is due to the small bandwidth of the driving resonance mode. The amplitude fluctuation in v_{ref} introduces error in $\dot{y} \times v_{ref}$ and v_{out}. Improved accuracy can be achieved by using $\dot{x}$ as the reference signal.

The current circuitry also has a challenge in the creation of accurate phase of the reference voltage. More accurate in-phase and quadrature signals can be generated, for example, by using digital phase-lock loop (PLL) and digital frequency divider [7]. In addition, the parasitic capacitance at the non-inverting node of the frontend TIA can be reduced by mounting the gyro chip and by reducing the distance of the electrical line between the amplifier and the gyro chip.

4.14.3. Geometry Optimization for Mode Separation and Controllability

The sensor design can be further optimized to have wider separation between the sensing mode and the parasitic sensing mode. The structure and location of the sense-coupling spring is closely related to the amount of angular deflection in the driving mode.

Devices with different coupling spring designs will be compared for their vibration sensitivity.

4.15. Summary

This chapter described the design and fabrication of the Balanced Oscillating Gyroscope (BOG). The relationship between the geometry of the gyro and the frequency separation between operational and parasitic modes is studied. The first-generation BOG is built using high-aspect-ratio, high-accuracy Si-on-Glass (SOG) process with a device thickness of 100µm. The BOG with a minimum mode separation of 5Hz is evaluated in the open-loop mode using analog interface circuitry. The gyro has a sensitivity of 5.6mV/°/s and an angle random walk (ARW) of 0.44°/sec/√Hz. An addition of balancing electrodes and quadrature feedback electrodes will improve the performance of the device.

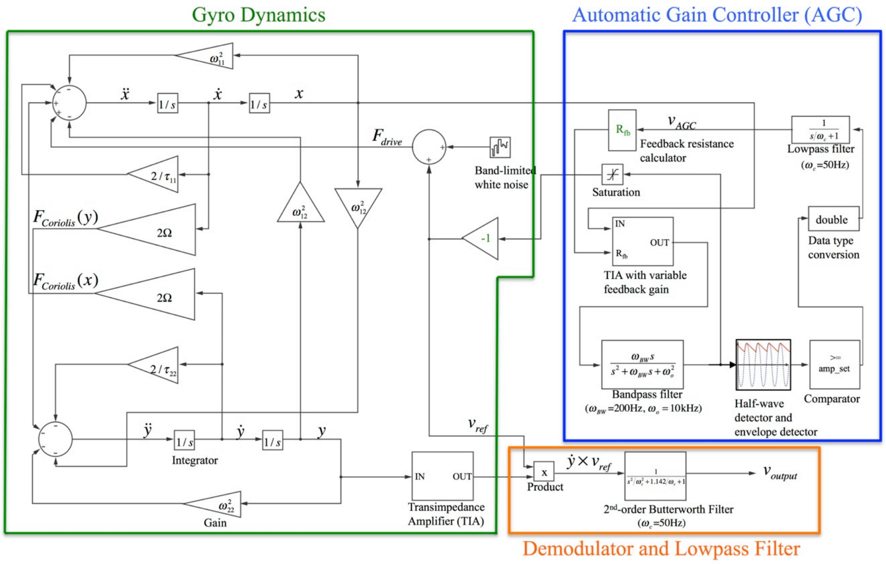

Figure 4.48. Simulink model of the gyro and first-generation circuitry. This model is used to simulate bias instability due to fluctuation in reference signal. The gyro model includes cross-coupling stiffness. Cross-coupling damping is omitted for simplicity. The output voltage (v_{output}) is proportional to the quadrature error signal.

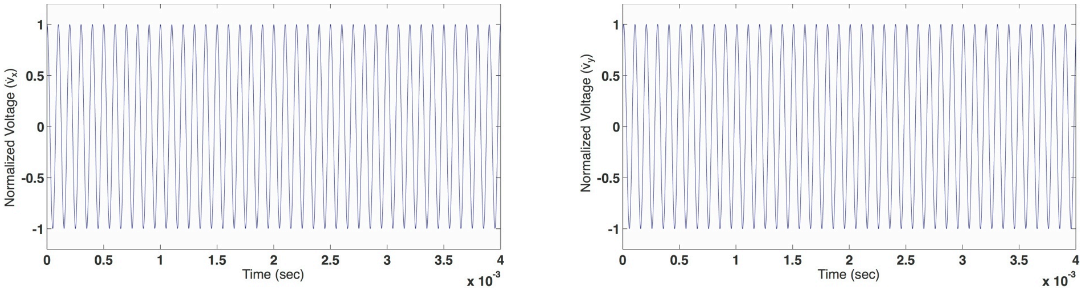

(a) Normalized velocity along driving axis [$\dot{x}$ (normalized)]

(b) Normalized velocity along sense axis [$\dot{y}$ (normalized)]

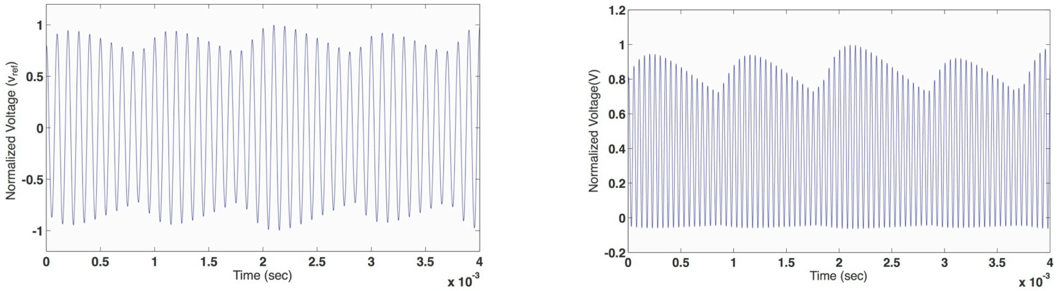

(c) Normalized reference voltage [v_{ref} (normalized)]

(d) Normalized modulated voltage [$v_{ref} \times \dot{y}$ (normalized)]

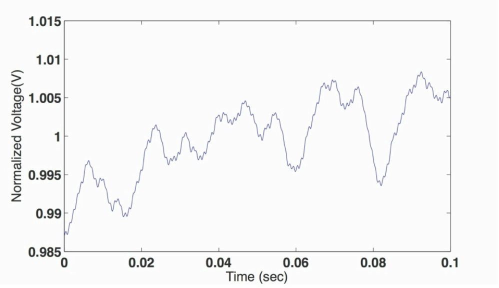

(e) Output voltage of the demodulation block after the low pass filter (cutoff frequency: 50Hz)

Figure 4.49. Simulated waveforms of normalized velocity along driving and sense axes ($\dot{x}$ (normalized), $\dot{y}$ (normalized)), reference voltage (v_{ref} (normalized)), modulated voltage ($v_{ref} \times \dot{y}$ (normalized)), and output voltage (v_{out}).

CHAPTER 5.

HIGH-FREQUENCY SINGLE-CRYSTAL-SILICON CYLINDRICAL RATE-INTEGRATING GYROSCOPE (CING)

This chapter describes the design, fabrication, and evaluation a Single-Crystal-Si Cylindrical Rate-Integrating Gyroscope (CING). The advantages of the CING are complete axisymmetry, easy frequency controllability, and larger ratio between parasitic frequencies and the wineglass frequency ($f_{parasitic}/f_{wineglass}$), which affects the response of the sensor under vibration and shock. To improve the fabrication of CING, the Si-on-glass (SOG) process is calibrated for creating 3D structures like the CING. The gyro is tested in the rate- and rate-integrating modes using digital circuitry, developed within our group [129].

5.1. Geometries for the MEMS Rate-Integration Gyroscope (RIG)

The vibratory rate-integrating gyroscope (RIG) serves either as a rate (RG) or a rate-integrating gyro (RIG). To have small drift, the vibratory RIG needs to have identical resonance frequencies and *Q*. Many RG's, like the BOG, are designed with non-degenerated modes with innate mechanical anisotropy, so that they may be more accurate in the rate-sensing mode. The drift rate due to anisotropic damping is inversely related to the damping time difference ($\Delta 1/\tau$) of the gyro. Due to the inverse proportional relationship between the damping time (τ_o) and the operating frequency (f_o), lower-frequency gyro are expected to achieve a lower drift due to anisotropic damping.

There has been only a single practical RIG so far [45]. The device in [45] is the quad-mass tuning-fork gyroscope. The device is weakly decoupled with respect to the x- and y- axes. The device operates at 2kHz with a Q of more than 1 million. The attractiveness of the non-axisymmetric gyro is the compatibility with conventional planar microfabrication processes. The challenges of 2D low-frequency gyros include complicated structures and the existence of parasitic modes below the resonance mode, which increases sensitivity to environmental vibration and shock. On the other hand, axisymmetric gyro designs like CING have advantages of simpler design, complete axisymmetry, and fewer parasitic modes. The gyro has a single anchor at the center of the design, minimizing the effect of thermoresidual stress under temperature variation. However, the drawback of the CING is the lower angular gain (A_g), in the range of 0.07 for 2500μm radius and 300μm tall device.

Figure 5.1 shows a few axisymmetric resonator geometries considered in the presented study: hemisphere, half-toroid, ring, disk, simple cylinder, and multi-ring cylinder. These geometries have either already been realized or are currently being attempted as vibratory gyroscopes. The geometries are compared for simplicity of microfabrication and mode characteristics.

The hemispherical resonator geometry is used in the Hemispherical Resonator Gyroscope (HRG), and the HRG serves as the state-of-art vibratory gyroscope [109]. Due to the curvature of the sidewall, the placement of electrodes, and the vertical level of the edge of the shell and the anchor, it is difficult to micro-machine this geometry.

In the half-toroid shell geometry, the anchor is located at the same level as the top edge of the shell [110]. This is expected to simplify fabrication of this geometry compared to the hemispherical geometry. The primary challenges in the fabrication of the half-toroid are isotropy and control of sidewall curvature.

The ring geometry has been previously adopted to make vibratory rate gyroscopes [7]. Advantages of the ring geometry include simplicity of the microfabrication and controllability of the resonance frequency. The main challenge in this geometry is achieving mechanical anisotropy because of the supporting springs.

The disk geometry is used in the Si bulk-acoustic wave (BAW) gyroscope [26]. The advantages of the disk geometry include simplicity in fabrication and complete axisymmetry. The challenge of the disk geometry is the difficulty of designing the geometry to operate at <10kHz with a small footprint, for use as a rate-integrating gyro.

The cylinder geometry is used in [111]. This geometry provides complete symmetry, and the resonance frequency can be easily controlled by changing the wall thickness. However, it is challenging to define such a geometry using a single masking step.

The multi-ring-cylinder geometry (named the CING geometry) has a number of rings that fill the space between the innermost wall and the outermost wall of the cylinder [112]. This geometry is completely axisymmetric and a single-crystal-Si multi-ring gyro can be microfabricated relatively simply using the DRIE lag effect, with a single masking step.

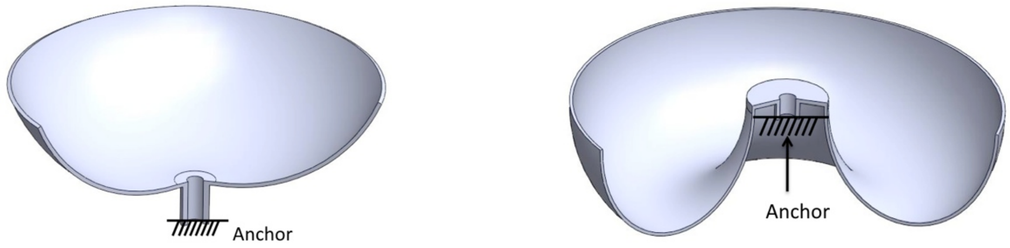

(a) Hemisphere (b) Half-toroid (birdbath)

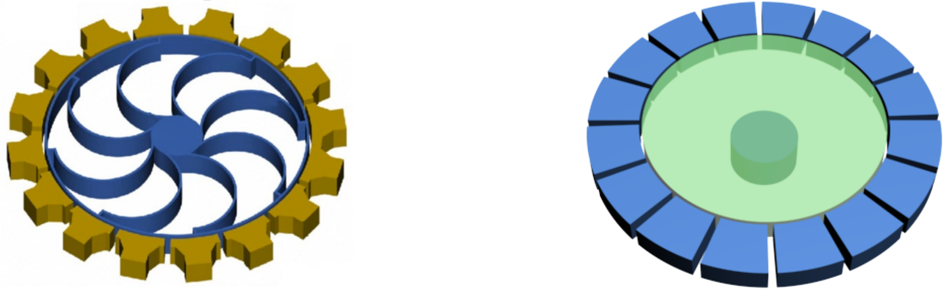

(c) Ring (d) Disk

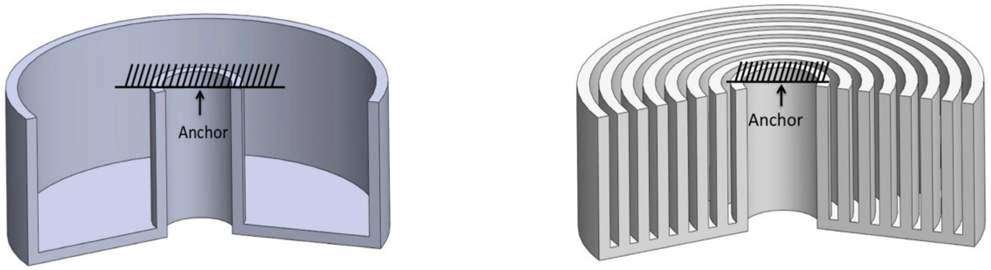

(e) Simple cylinder (folded) (f) Multi-ring cylinder (folded) (CING)

Figure 5.1. Axisymmetric resonator shapes for the MEMS rate-integrating gyroscope (RIG).

The relative frequencies of a gyro's resonance modes are critical to its ability to reject environmental vibrations. The types of resonance modes found near the n=2 wineglass mode, include the tilting and vertical deflection mode. In the tilting mode, the mass is rotated with respect to the planar (x-y) axes. Due to the symmetry of these structures, two tilting modes with identical frequencies are found. In the vertical mode, the mass of the gyro is deflected in the vertical direction. The shapes of the wineglass mode, tilting mode, and vertical mode for the CING are illustrated in Figure 5.2. Table 5.1 compares fabrication simplicity, axisymmetry, wineglass mode frequency (f_{WG}), ratios of tilting and vertical mode frequencies to the wineglass mode frequency ($f_{tilting}/f_{WG}$,

$f_{vertical}/f_{WG}$), effective mass (M), and angular gain (A_g) of range of device sizes for each geometry. The range of the outer radius (R), anchor radius (AR), and height (H) are the same for all geometries. The aspect ratio (H/R) of the considered geometries is set to be less than 0.2. The thicknesses of the geometries are set to be in the range that can be created using conventional micromachining processes. The n=3 wineglass mode also exists near the n=2 wineglass mode, but due to the balanced characteristics of the mode, it will not be excited by environmental vibration and so it is not considered in this comparison. It should be noted that in the ring geometry, due to the flexibility of the support spring, lateral and rotational modes exist below the wineglass mode. Among the considered geometries, the multi-ring geometry offers the greatest separation between parasitic and wineglass modes indicated by having the largest $f_{parasitic}/f_{WG}$.

Large effective mass (M) and angular gain (A_g) are important for having a larger Coriolis mass (γ), which leads to a larger scale factor in both rate-sensing and rate-integration modes. Among the considered geometries, the disk and multi-ring geometries have the largest M. The ring geometry has the largest A_g (0.4), which is 5 to 20 times larger than the A_g of the other geometries. The shell, disk, and multi-ring geometries have small A_g because of large out-of-plane displacement in the wineglass mode. In chapter 3, A_g is defined as:

$$A_g = \frac{\gamma}{nM} \text{ (for } n\text{th wineglass mode)} \qquad \text{(Equation 5.1)}$$

The M and γ are expressed using the shape functions of finite elements in the Cartesian coordinate for the two wineglass modes (ϕ_{x1}, ϕ_{y1}, ϕ_{z1}, ϕ_{x2}, ϕ_{y2}, ϕ_{z2}) as:

$$M_1 = \int_V \rho(\phi_{x1}^2 + \phi_{y1}^2 + \phi_{z1}^2)dV \qquad \text{(Effective mass for mode 1)} \qquad \text{(Equation 5.2)}$$

$$M_2 = \int_V \rho(\phi_{x2}^2 + \phi_{y2}^2 + \phi_{z2}^2)dV \qquad \text{(Effective mass for mode 2)} \qquad \text{(Equation 5.3)}$$

$$\gamma = \int_V \rho(\phi_{x1}\phi_{y2} - \phi_{x2}\phi_{y1})dV \qquad \text{(Coriolis mass)} \qquad \text{(Equation 5.4)}$$

The difference between γ and M is that γ is not contributed by motion along the z-axis, whereas M increases with ϕ_{z1} and ϕ_{z2}. This is because the out-of-plane (z-axis) motion does not contribute to create the Coriolis force.

The A_g of a wineglass mode gyro increases as the aspect ratio of the gyro increases. Figures 5.3 (a) and (b) compare the flexural mode patterns of cylinder gyros with two different aspect ratios. In the lower aspect-ratio gyro (Figure 5.3 (a)), the bottom plate has larger flexibility than the vertical sidewall (along the z-axis), so large displacement occurs from the bottom plate. The direction of the displacement is along the z-axis. In the higher aspect-ratio gyro (Figure 5.3 (b)), the vertical sidewall has larger flexibility than the bottom plate, so large lateral motion occurs from the vertical sidewall. The lateral motion contributes to the creation of the Coriolis force, so the higher aspect-ratio gyro has a larger A_g.

Table 5.2 compares the mechanical characteristics of the gyros as their aspect ratios become 1. In this aspect ratio, the A_g of all the geometries become 0.3~0.4, but it is very difficult to fabricate these geometries using the conventional micromachining process.

In this research, we develop the multi-ring cylinder gyro (CING) with a radius of 2.5mm and height of 300µm, resulting in an aspect ratio of 0.12. Although the CING geometry that we investigate has a small A_g, the complete axisymmetry and stable modal charactersitics makes it a useful rate-integrating gyroscope (RIG).

(a) Wineglass mode (b) Tilting mode

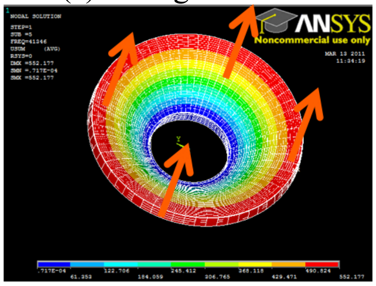

(c) Vertical mode

Figure 5.2. Displacement pattern of wineglass mode, tilting mode, and vertical mode of the CING.

Table 5.1. Comparison of fabrication simplicity, axisymmetry, mode characteristics (f_{WG}, $f_{tilting}/f_{WG}$, $f_{vertical}/f_{WG}$), effective mass (M), and angular gain (A_g) of the RIG shapes with aspect ratio (height/radius) less than 0.2

Gyro shape	Hemisphere [109] *	Half-toroid (birdbath) * [110]	Ring [7]	Disk [26]	Simple cylinder [111]	Multi-ring cylinder (CING) [112]
Fabrication simplicity	Very difficult	Very difficult	Easy	Easy	Difficult	Easy
Axisymmetry	Yes	Yes	Not completely	Yes	Yes	Yes
Wineglass mode frequency (f_{WG})	2.5~5.1 kHz	5.4~15 kHz	8.6~24.5 kHz	40.5~134 kHz	13~46 kHz	14~38 kHz
$f_{tilting}/f_{WG}$	0.8~3.1	1.1~1.7	0.4~0.9**	0.8~0.9	0.4~0.9	0.8~1.8
$f_{vertical}/f_{WG}$	2.4~4.0	2.0~3.2	0.4~1	~0.9	0.5~1.1	1.7~2.8
Effective mass (M)	< 80μg	< 80μg	< 800μg	< 5mg	< 300μg	< 1mg
Angular gain (A_g)	~0.03	~0.05	~0.4	~0.02	~0.06	~0.08

- Condition: material: Si, radius: 2~2.5mm, anchor radius: 500~1000μm, height: <500μm. The thickness of the shell for hemisphere and birdbath gyro is 5~10μm. The thickness of ring, cylinder wall, and multi-ring cylinder is 20~40μm.

*: The ratios between tilting and vertical modes and wineglass mode ($f_{tilting}/f_{WG}$, $f_{vertical}/f_{WG}$) depend strongly on the curvature of gyro.

**: In ring gyro, translational mode and rotational mode exist below the wineglass mode.

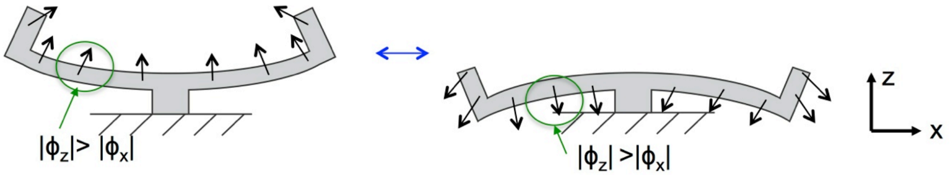

(a) Small aspect ratio (height/radius)

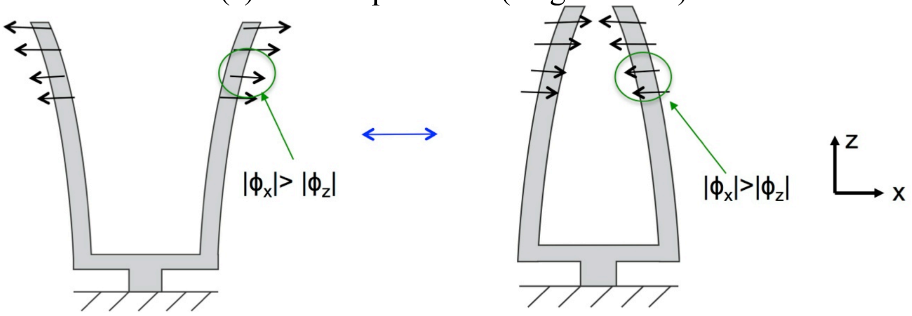

(b) Large aspect ratio (height/radius)

Figure 5.3. Comparison of wineglass-mode displacement patterns of cylinder resonators with different aspect ratios (height/radius).

Table 5.2. Comparison of fabrication simplicity, axisymmetry, mode characteristics (f_{WG}, $f_{tilting}/f_{WG}$, $f_{vertical}/f_{WG}$), effective mass (M), and angular gain (A_g) of the RIG shapes with aspect ratio (height/radius) of 1

Gyro shape	Hemisphere * [109]	Half-toroid (birdbath) * [110]	Ring** [7]	Disk*** [26]	Simple cylinder **** [111]	Multi-ring cylinder**** (CING) [112]
Fabrication simplicity	Very difficult	Very difficult	Very difficult	Very difficult	Very difficult	Very difficult
Axisymmetry	Yes	Yes	Not completely	Yes	Yes	Yes
Wineglass mode frequency (f_{WG})	15.3kHz	11.2kHz	10.6kHz	88.9kHz	6.3kHz	6.2kHz
$f_{tilting}/f_{WG}$	4.2	4	> 4	1.5	1.2	1.3
$f_{vertical}/f_{WG}$	> 6	> 6	> 4	4	1.5	2.5
Effective mass (M)	160µg	180µg	3.2mg	46mg	460µg	2mg
Angular gain (A_g)	0.3	0.3	0.4	0.43	0.34	0.35

*: Radius: 2.5mm, anchor radius: 1mm, height: 2500µm, thickness: 10µm
**: Radius: 2.5mm, anchor radius: 1mm, height: 2500µm, ring thickness 40µm. Translational and rotational modes exist below the wineglass mode
***: Radius: 2.5mm, anchor radius: 1mm, height: 2500µm. Rotational mode exists below the wineglass mode
****: Radius: 2.5mm, anchor radius: 1mm, height: 2500µm, thickness: 20µm

5.2. Cylindrical Rate-Integrating Gyro (CING)

5.2.1. Overall Description

The architecture of the CING is illustrated in Figure 5.4. It consists of 1) a multi-ring cylinder resonator; 2) side electrodes, surrounding the outer perimeter of the resonator; 3) a ring electrode, surrounding the inner perimeter of the resonator; and 4) bottom electrodes, located underneath the resonator. The CING is fabricated from a (111) single-crystal Si wafer using the Si-on-glass (SOG) process.

The multi-ring resonator faces downwards and bonds to the bottom substrate (glass) at its innermost ring. The resonator faces 16 discrete side electrodes and bottom electrodes, each spanning almost 22.5°. The ring electrode is surrounded by the innermost ring of the gyro. Using the nonlinearity of the capacitive force, the ring electrode can actuate the resonator in the wineglass mode.

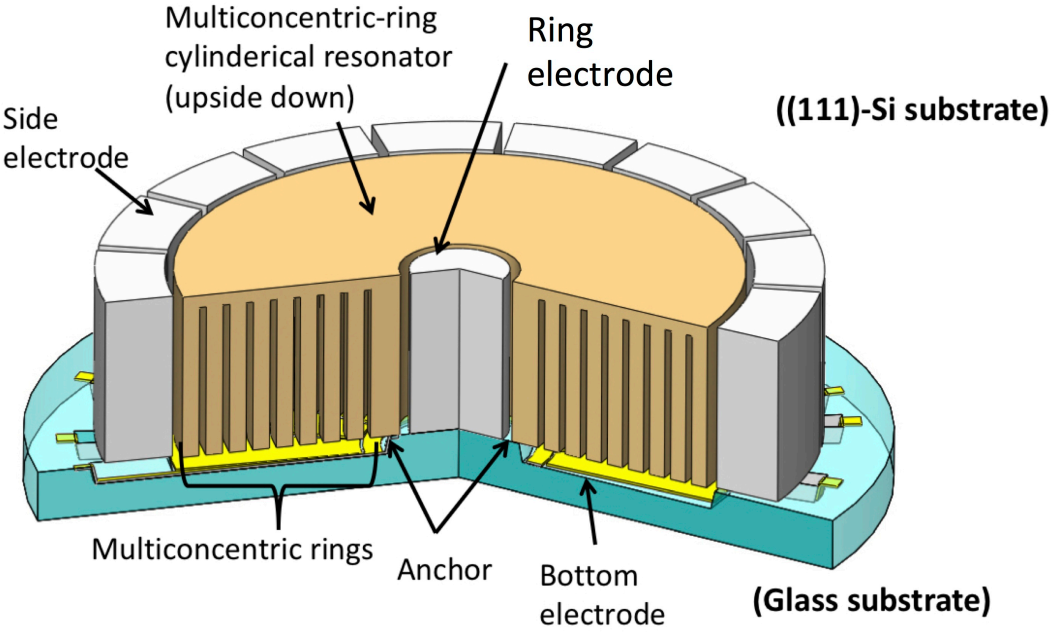

Figure 5.4. Single-Crystal-Si Cylindrical Rate-Integrating Gyroscope (CING).

5.2.2. Dependency of Resonance Frequencies on Geometry

The design parameters for the multi-ring cylinder include the radius (*R*), anchor radius (*AR*), height (*H*), ring thickness (*T*), bottom plate thickness (*BT*), anchor thickness (*AT*), and the number of rings (*N*) (Figure 5.5). The relationships between the geometry parameters and the change in the wineglass frequency (f_{WG}) and the parasitic frequencies ($f_{vertical}$, f_{tilting}) are found using FEM analysis.

5.2.2.1. Outer Radius (*R*)

The dependency of the wineglass mode frequency (f_{WG}), tilting mode frequency ($f_{tilting}$), and vertical mode frequency ($f_{vertical}$), and *n*=3 wineglass mode ($f_{n=3}$) on the outer radius (*R*) is shown in Figure 5.6. The relationship is studied with an *R* of 2mm to 4mm, while keeping the rest of the dimensions constant (*AR*: 1 mm, *H*: 300µm, *T*: 30µm, *AT*: 100µm, *BT*: 30µm). In this study, we used approximate geometries that have fewer numbers of rings (*N*) so that ANSYS can successfully mesh and simulate the structure. The simulation results show that the as *R* increases, all of the frequencies drop, but f_{WG} and $f_{n=3}$ decrease slower than the parasitic modes.

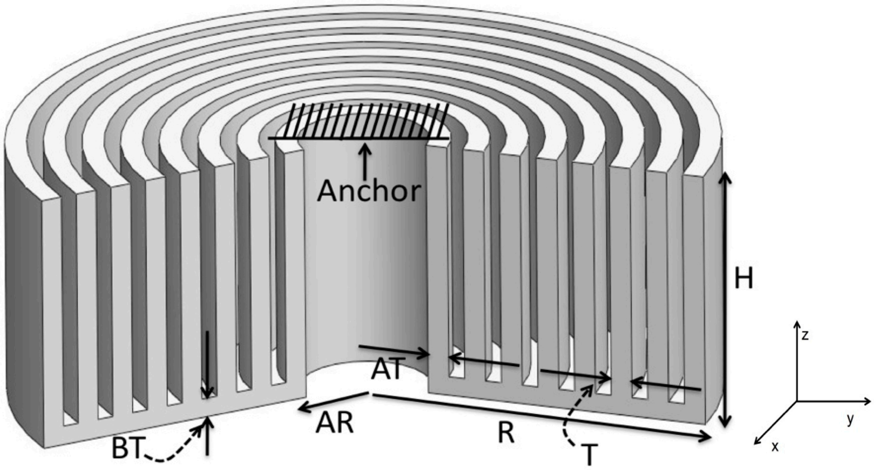

Figure 5.5. Geometrical parameters of the CING.

5.2.2.2. Inner Radius (*AR*)

Figure 5.7 shows the simulated relationship between the mode frequencies and the anchor radius (*AR*), while other parameters are kept constant (*R*: 2.5mm, *H*: 300µm, *T*: 30µm, *AT*: 100µm, *BT*: 30µm). The f_{WG}, $f_{vertical}$, and $f_{tilting}$ increase with *AR*, but the parasitic modes are affected more than f_{WG} and $f_{n=3}$. The $f_{n=3}$ has smallest dependency on the change in *AR*. As *AR* increases above ~1700µm, $f_{n=3}$ is at a lower frequency than f_{WG}.

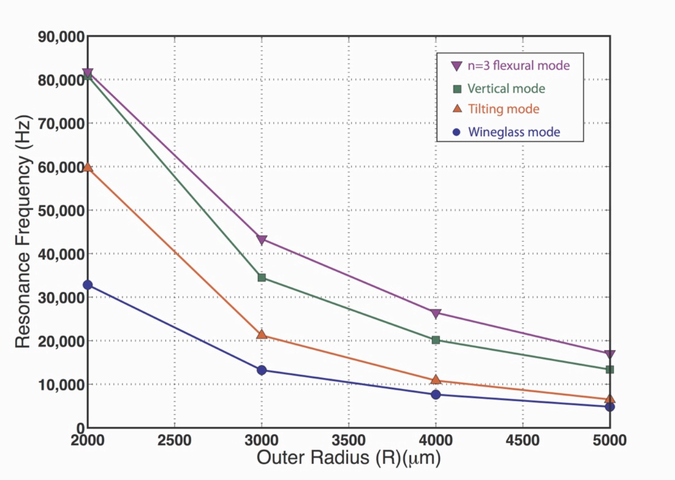

Figure 5.6. Relationship between the outer radius (*R*) and the frequencies of wineglass mode (f_{WG}), vertical mode ($f_{vertical}$), tilting mode (f_{WG}), and *n*=3 flexural mode ($f_{n=3}$) (*AR*: 1mm, *H*: 300µm, *T*: 30µm, *AT*: 100µm, *BT*: 30µm).

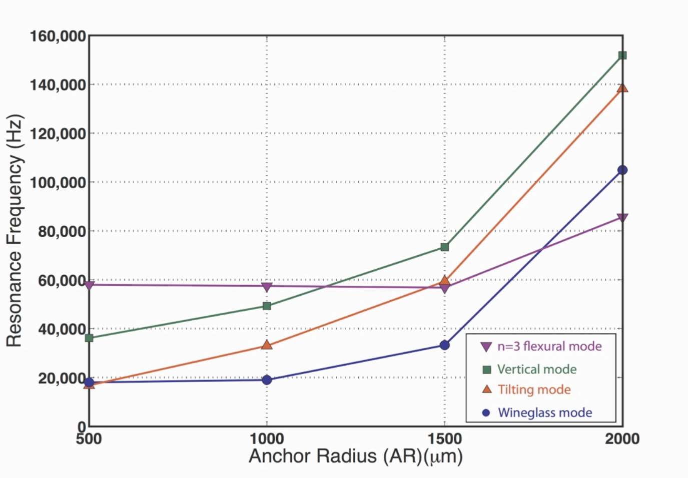

Figure 5.7. Relationship between the anchor radius (*AR*) and the frequencies of wineglass mode (f_{WG}), vertical mode ($f_{vertical}$), tilting mode (f_{WG}), and *n*=3 flexural mode ($f_{n=3}$) (*R*: 2.5mm, *T*: 30µm, *H*: 300µm, *AT*: 100µm, *BT*: 30µm).

5.2.2.3. Ring Thickness (*T*)

Figure 5.8 shows the simulated relationship between the mode frequencies and the ring thickness (*T*), while other parameters are kept constant (*R*: 2.5mm, *AR*: 1mm, *H*: 300µm, *AT*: 100µm, *BT*: 30µm). The rings add stiffness to the bending stiffness of the bottom plate, so as *T* increases, all of the mode frequencies increase. The increase in *T* also adds mass to the system. The largest slopes in the frequencies versus *T* are found for smaller *T*. As *T* increases, the $f_{tilting}$ and $f_{vertical}$ start to saturate, due to the saturation in the bending stiffness of the bottom plate and increase in the mass. The f_{WG} and $f_{n=3}$ increase at nearly constant slopes, indicating that the effective mass for the wineglass modes increases more slowly than the $f_{tilting}$ and $f_{vertical}$. This simulation result indicates that relatively low f_{WG} (<20kHz) and large gap between f_{tilting} and f_{WG} (>5kHz) can be achieved when *T* is smaller than 30µm. A challenge in the reduction of *T* comes from lithography process. Later in this chapter, we discuss the process conditions with AZ9260 photoresist that we developed for achieving such a high aspect ratio.

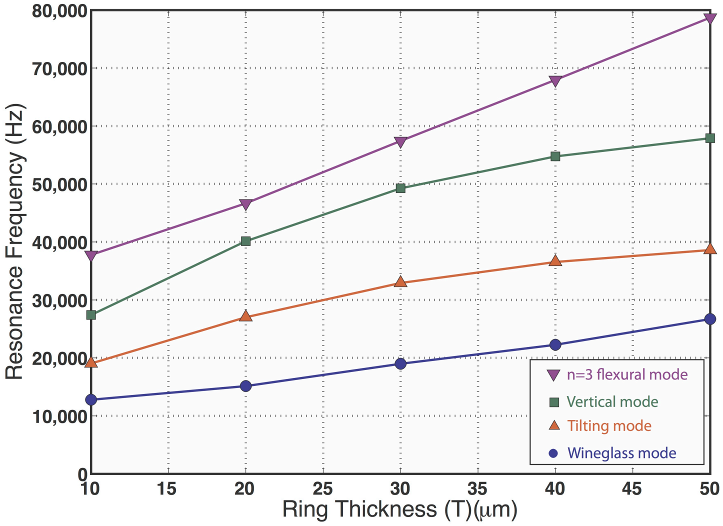

Figure 5.8. Relationship between the ring thickness (*T*) and the frequencies of wineglass mode (f_{WG}), vertical mode ($f_{vertical}$), tilting mode (f_{WG}), and *n*=3 flexural mode ($f_{n=3}$) (*R*: 2.5mm, *AR*: 1 mm, *H*: 300µm, *AT*: 100µm, *BT*: 30µm).

5.2.2.4. Height (*H*)

Figure 5.9 shows the simulated relationship between the mode frequencies and device height (*H*), while other parameters are kept constant (*R*: 2.5mm, *AR*: 1 mm, *T*: 30µm, *AT*: 100µm, *BT*: 30µm). The resonance frequency of the gyro increases with the increase in *H* for 100µm to 300µm. As *H* increases above 300µm, the frequencies start to drop. This tendency can be understood as when *H* is low, the stiffness of the vertical walls is considerably higher than the stiffness of the bottom plate, so that as *H* increases, it adds stiffness to the bottom plate and increases the resonance frequency. However, as *H* goes above 300µm, the flexibility of the vertical walls starts to influence the overall flexibility of the device.

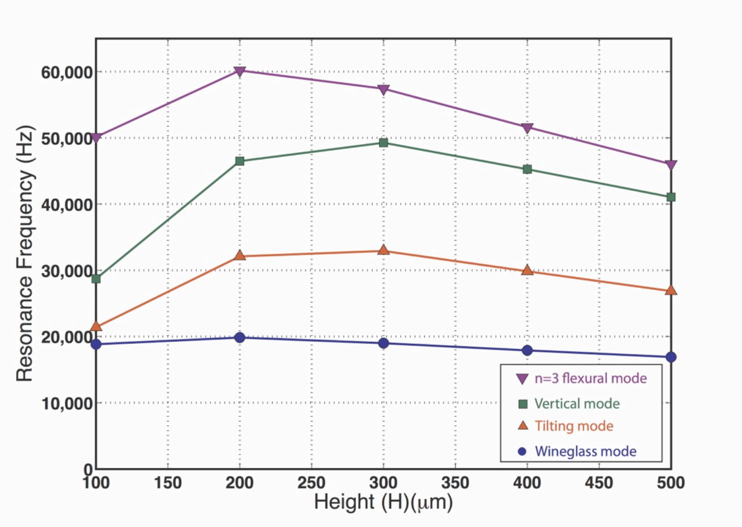

Figure 5.9. Relationship between the height (*H*) and the frequencies of wineglass mode (f_{WG}), vertical mode ($f_{vertical}$), tilting mode (f_{WG}), and n=3 flexural mode ($f_{n=3}$) (*R*: 2.5mm, *AR*: 1 mm, *AT*: 100µm, *BT*: 30µm).

5.2.2.5. Bottom Thickness (*BT*)

Figure 5.10 shows the simulated relation between the mode frequencies and the anchor radius (*BT*), while other parameters are kept constant (*R*: 2.5mm, *AR*: 1mm, *H*: 300µm, *T*: 30µm, *AT*: 100µm). The slope for the change of the flexural mode frequency is found to be larger than for the parasitic frequencies. A good mode separation is achieved with a *BT* of 20~30µm.

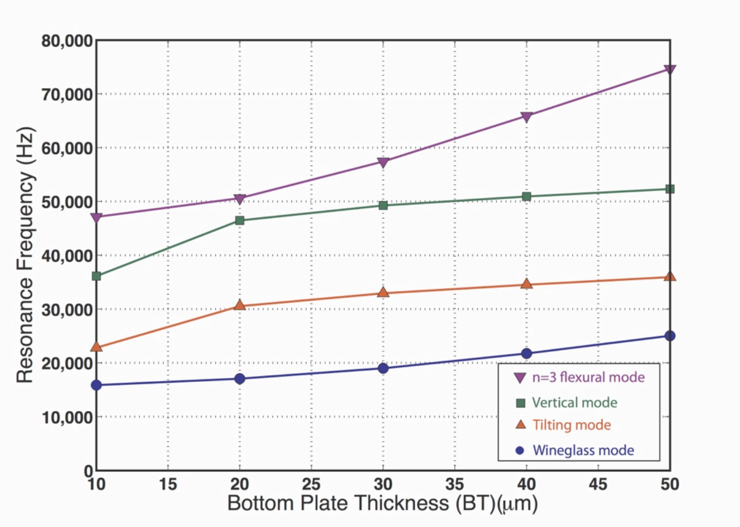

Figure 5.10. Relationship between the bottom plate thickness (*BT*) and the frequencies of wineglass mode (f_{WG}), vertical mode ($f_{vertical}$), tilting mode (f_{WG}), and n=3 flexural mode ($f_{n=3}$) (*R*: 2.5mm, *AR*: 1mm, *H*: 300µm, *AT*: 100µm).

5.2.3. Dimension of the 1st Generation CING

The first-generation CING is designed to operate at 17~23kHz, with a frequency separation between the wineglass mode to the parasitic modes of more than 800Hz. The height of the CING is 300~350µm. The geometry, electrical properties, and calculated physical properties of the first-generation CING are included in Table 5.3.

5.3. Energy Loss Mechanism of the CING

The major energy loss mechanisms for low-frequency, single-crystal-Si resonators in vacuum are thermoelastic damping (TED), anchor loss, and surface loss. Thermoelastic damping (TED) is an energy loss mechanism occurring from strain changes following the temperature profile inside a vibrating structure. The temperature profile is determined by the interaction of: 1) thermal gradient generation through adiabatic extension and compression and 2) thermal diffusion, following the generated temperature gradient